MEMS Varifocal Mirror for High-Power Laser Focusing

by

André Augusto Geraldes

Submitted to the Department of Computer Science
in partial fulfillment of the requirements for the degree of

Doctor of Philosophy in Computer Science
S.S.D. ING-INF05
Cycle XXXI/2015

at the

Università degli Studi di Verona

May 2019

© Università degli Studi di Verona 2019. All rights reserved.

Author . . . . . .
Department of Computer Science
May. 13, 2019

Certified by . . . . . .
Prof. Paolo Fiorini
Full Professor
Thesis Tutor

Certified by . . . . . .
Leonardo De Mattos
PhD
Thesis Tutor

Accepted by . . . . . .
Prof. Massimo Merro
Chairman of the PhD School Council

This work is licensed under a Creative Commons Attribution-NonCommercial-NoDerivs 4.0 Unported License, Italy. To read a copy of the licence, visit the web page:
`https://creativecommons.org/licenses/by-nc-nd/4.0/`

Attribution – You must give appropriate credit, provide a link to the license, and indicate if changes were made. You may do so in any reasonable manner, but not in any way that suggests the licensor endorses you or your use. **NonCommercial –** You may not use the material for commercial purposes.
NoDerivatives – If you remix, transform, or build upon the material, you may not distribute the modified material.

MEMS Varifocal Mirror for High-Power Laser Focusing – André Augusto Geraldes
PhD Thesis, Verona, May. 13, 2019.
ISBN: XXXXXXXXXXXXX

©All rights reserved. This copy of the thesis has been supplied to ensure timely dissemination of scholarly and technical work on condition that anyone who consults it is understood to recognize that its copyright rests with its author and that no quotation from the thesis and no information derived from it may be published without the author's prior consent.

MEMS Varifocal Mirror for High-Power Laser Focusing

by
André Augusto Geraldes

Submitted to the Department of Computer Science
on May. 13, 2019, in partial fulfillment of the
requirements for the degree of
Doctor of Philosophy in Computer Science
S.S.D. ING-INF05
Cycle XXXI/2015

Abstract

Today, lasers are used in many surgical procedures due to their ability of performing precise incisions, and ablations. With the development of fiber-coupled lasers, even minimally invasive procedures started making use of laser tools. However, existing fiber tools do not provide the same performance as traditional laser systems, often causing significantly more tissue carbonization. This can be attributed to the lack of optics in fiber tools, which requires the tip of the fiber to be placed in direct contact with the tissue, increasing the collateral damage of the laser. To avoid this issue, a compact focusing system should be integrated in the fiber tool. However, traditional optical systems based on moving lenses are too large and bulky for that. To solve this problem, this thesis proposes a focusing system based on MEMS deformable mirrors. Using microfabrication methods, we develop a novel MEMS varifocal mirror, designed for focusing high-power laser in a fiber laser system. The design of this mirror is based on state-of-the-art MEMS deformable mirrors, which have been proposed for microscopy applications, with significant adaptations for high-power lasers, including different actuation mechanisms and control strategies. We explore the use of hydraulic actuation to achieve large focal length range, while providing compatibility with high-power laser. The deflection of the mirror is controlled using a feed-forward model, in which parameters are obtained through characterization of the fabrication process. This allows controlling the mirror without a beam splitter or external sensors, which contributes to the miniaturization of the focusing system.

Thesis Advisor: Prof. Paolo Fiorini
Title: Full Professor

Thesis Advisor: Leonardo De Mattos
Title: PhD

Acknowledgments

Finishing a PhD is a very rewarding experience. However this accomplishment would not have been possible without the support of so many friends who have helped me throughout these years of doctoral studies. It is my great pleasure now to thank them for their invaluable contribution.

First, I would like to thank my advisor, Dr. Leonardo De Mattos, for guiding my work, always pointing me in the right direction. More importantly, thank you for being so dedicated and committed to the laboratory and for inspiring me to do the same. Thank you also for encouraging me to seek collaborations outside our department, which allowed me to acquire important skills for my career, and for never second-guessing me, even when results took long to arrive. Your trust in me was a great source of motivation.

I am equally grateful to my other advisor, Prof. Paolo Fiorini, for his advices in all stages of my PhD. Thanks for making me see beyond my research project, teaching me also to consider the implications of my work on other projects. Thanks for sharing your wisdom with me.

Furthermore, I am thankful to the members of my thesis committee, Prof. Riccardo Muradore and Prof. Tiziano Villa, for their valuable feedback at the end of each year of my PhD. Thank you also for our collaboration project on formal verification of medical systems. In this regard, I must also thank Prof. Luca Geretti, for the paper we wrote together. This experience was the best writing class I had during the PhD.

I am also in debt with the reviewers of my thesis, Prof. Arianna Menciassi and Dr. Marti Duocastella, for accepting this task and for putting so much effort in improving my work. Your insightful comments were essential to conclude this doctoral thesis. I also thank Marti for being my reference in the field of optics and for being always open to answer my questions.

I would like to thank Dr. Francesco De Angelis for giving me the opportunity to work in IIT's clean room, even though I did not have prior experience in the field. And most importantly, thanks to Dr. Andrea Jacassi who taught me everything I know about microfabrication. His patience and interest were fundamental to introduce me to this field of work and to allow me to succeed on it. I could not have done it without him.

It is also a pleasure to thank my dear colleagues at IIT: Alperen Acemoglu, Zhuoqi Cheng, Veronica Penza, Lucia Schiatti, Jesus Ortiz, Olmo Alonso Moreno Franco, Nabeel Kamal, Nikhil Deshpande, Giacinto Barresi, Brendan Michael Emery and Yonas Teodros Tefera. Thank you for the countless suggestions about my work and thank you also for the daily company and for all the coffees, aperitivos and dinners we shared.

I am grateful to all the technicians and secretaries of IIT, for the amazing support they provided me. I feel lucky to be able to count with the support of so many

competent people. I am also grateful to Laura Marcazzan for the countless times she helped me dealing with bureaucratic issues of the University of Verona. If it were not for her kindness and patience, I do not think I would have been able to fulfill all the requirements for obtaining the PhD.

Thanks to my family for always supporting my life choices, giving me the courage to pursue an academic career. And special thanks to my mother, Rosangela, for teaching me to chase my dreams and to never give up.

Finally, I am extremely grateful to my beloved wife Ana, who has been my greatest partner over the last five years. Thank you for all your kindness and love. You are my balance and my peace.

Contents

1 Introduction **13**
1.1 Technical and Scientific Challenges 14
1.2 Contributions of the Thesis 15
1.3 Outline of the Thesis 16

2 Laser Surgery Fundamentals **18**
2.1 Laser Fundamentals 18
2.2 Laser Beam Optics 21
2.2.1 Laser Beam Propagation 22
2.2.2 Optical Aberrations 23
2.2.3 Quantifying Optical Aberrations 25
2.3 Laser-Matter Interaction 26
2.3.1 Interaction with Biological Tissue 27
2.3.2 Thermal Interactions 27
2.4 Clinical Applications 29
2.4.1 Laser Delivery Systems 30
2.4.2 Open Challenges with fiber laser tools 31
2.5 Conclusion 33

3 Review of MEMS Varifocal Mirrors **34**
3.1 Fundamentals of Varifocal Mirrors 34
3.2 Membrane Mirrors 35
3.2.1 Electrostatic Mirrors 36
3.2.2 Pneumatic and Hydraulic Mirrors 38
3.3 Bimorph Mirrors 41
3.3.1 Electrothermal Mirrors 41
3.3.2 Piezoelectric Mirrors 43
3.4 Comparison between Varifocal Mirrors 44

4 Modeling and Simulation **46**
4.1 Membrane Deflection Model 46
4.1.1 Deflection Model for Circular Membranes 47
4.1.2 Deflection Model for Elliptical Membranes 50

4.1.3 Thermal Deflection Model 51
4.1.4 Membrane Heating under Laser Irradiation 52
4.1.5 Explicit Model for the Membrane Central Deflection 54
4.2 Laser Focusing with a Varifocal Mirror 55
4.2.1 On-Axis Telescopic System 55
4.2.2 Off-Axis Parabolic Mirrors 56
4.2.3 Validity of the Approximation of the Off-Axis Paraboloid as an Elliptical Paraboloid 60
4.3 Laser Focusing as a Control Problem 60
4.3.1 Problem Formulation 60
4.3.2 Simplified Solution 63
4.3.3 General Solution 64
4.3.4 Errors due to the Far-field Approximations 66
4.4 Varifocal Mirror Design and Control 67
4.4.1 Feed-Forward Controller for the Varifocal Mirror 67
4.4.2 Varifocal Mirror Design Considerations 68
4.5 Conclusions 69

5 Mirror Fabrication 70
5.1 Overview of the Fabrication Process 70
5.2 Membrane Deposition 71
5.3 Patterning of the Silicon Bulk 72
5.4 Membrane Release 73
5.4.1 Membrane Release using DRIE and Wet Etching 74
5.4.2 Membrane Release using DRIE with an Etch-Stop Layer . . 78
5.4.3 Alternative Membrane Release Methods 79
5.5 Coating Deposition 79
5.5.1 Metallic and Dielectric Coatings 79
5.5.2 Deposition Methods for Metallic Coating 81
5.6 Complete Fabrication Process 81
5.6.1 Obtained Results 83
5.7 Improved Fabrication Process 83
5.8 Conclusion 85

6 Experimental Characterization 86
6.1 Hydraulic Actuation System 86
6.2 Methods for Measuring Mirror Deflection 88
6.2.1 Parametric Fitting Method 89
6.2.2 Far-Field Approximation Method 92
6.2.3 Fourier Method 92
6.3 Static Characterization 94
6.3.1 Experimental Setup 94

6.3.2 Experimental Procedure 94
6.3.3 Obtained Results 96
6.3.4 Corresponding Focal Length Range 103
6.3.5 Optical Quality 105
6.4 Focusing Demo in Fluorescent Medium 107
6.5 Thermal Characterization 110
6.5.1 Experimental Setup 111
6.5.2 Experimental Procedure 113
6.5.3 Obtained Results 114
6.6 Step Response 116
6.6.1 Experimental Procedure 117
6.6.2 Obtained Results 117
6.7 Integration with Fiber Laser Tools 118
6.8 Conclusion 120

7 Conclusions and Future Works 122
7.1 Concluding Remarks 122
7.2 Future Work 123
7.2.1 Improvements to the MEMS Varifocal Mirror 123
7.2.2 Design of a Compact Focusing System 124

A Mathematical Derivations 126
A.1 Solution to the Equation 4.36 126
A.2 Taylor Series Expansion of the Function 4.43a 128
A.3 Conversion of the Measured Focal Length in the Fluorescent Medium 129

List of Figures

2-1 Stimulated emission of radiation effect 19
2-2 Schematic diagram of a laser device 20
2-3 Transverse modes of a laser beam 20
2-4 Propagation of a focused Gaussian beam in free space 21
2-5 Common optical aberrations in focusing systems 24
2-6 Zernike polynomials on the unit circle up to the fourth order 26
2-7 Basic interactions between laser light and matter 26
2-8 Laser-tissue interaction types 28
2-9 Thermal effects that occur in biological tissue during thermal ablation 29
2-10 Laser phonomicrosurgery for vocal cord tumor resection 30
2-11 Laser delivery systems 31
2-12 Comparison of ablated tissue in contact (a) and focused (b) modes . 32
2-13 Proposed focusing system with variable focal length, based on a varifocal mirror 32

3-1 Operating principle of varifocal mirrors with electrostatic actuation . 36
3-2 Examples of varifocal mirrors with electrostatic actuation 37
3-3 Examples of varifocal mirrors with pneumatic actuation 40
3-4 Examples of varifocal mirrors with hydraulic actuation 40
3-5 Operating principle of varifocal mirrors with electrothermal actuation 42
3-6 Examples of varifocal mirrors with piezoelectric actuation 43

4-1 Deflection of a thin circular membrane under uniform pressure difference 47
4-2 Arc length of the parabola 49
4-3 Deflection of a circular membrane under compressive residual stress 52
4-4 Steady state solution of the FEM thermal simulation of the membrane under irradiation of a 3W continuous wave laser beam 53
4-5 Telescopic focusing system with two mirrors 56
4-6 Paraboloid with incident collimated beam parallel to its axis 57
4-7 Tangential cross section of the paraboloid centered at the transposed coordinate system 59
4-8 Diagram of focusing system in a fiber tool using a varifocal mirror . 60

4-9 Numerical solution to the required defocusing as a function of the distance to the tissue . . . 65
4-10 Laser focusing with the beam waist placed inside (a) or before (b) the tissue . . . 66
4-11 Error in the calculated value of z_t due to the far-field approximation 67

5-1 Cross-sectional diagram of a membrane mirror with elliptical boundary . . . 71
5-2 Main phases of the fabrication process of the membrane mirror . . . 71
5-3 Fabrication process for patterning the silicon bulk . . . 72
5-4 Fabrication process for creating the lithographic mask . . . 73
5-5 Lithographic masks used to fabricate circular (a) and elliptical (b) membranes . . . 74
5-6 Membrane releasing process using DRIE and wet etching . . . 74
5-7 Anisotropic wet etching of silicon . . . 76
5-8 SEM of the membrane (bottom side view) released with the HNA solution . . . 77
5-9 SEM of the membrane (bottom side view) released with the TMAH/IPA solution . . . 78
5-10 Membrane releasing process using DRIE with an etch-stop layer . . . 78
5-11 Alternative membrane release methods based on (a) patterning of a sacrificial layer or (b) wafer bonding . . . 80
5-12 Operating principle of a high-reflectance multilayer dielectric coating 80
5-13 Coating deposition through lift-off process . . . 82
5-14 First version of the complete fabrication process . . . 82
5-15 Fabricated membrane mirrors with circular (a) and elliptical (b) boundary . . . 83
5-16 Optical microscopy of defects on the reflective coating due to impurities trapped between the nitride and gold layers . . . 84
5-17 Improved version of the complete fabrication process . . . 84

6-1 Design of the mirror holder part . . . 87
6-2 Schematic diagram of the varifocal mirror connected to the mirror holder part . . . 87
6-3 Hydraulic actuation system . . . 88
6-4 Schematic diagram of the measurement system for the focal length of the mirror f_M using a wavefront sensor . . . 89
6-5 Operating principle of a Shack-Hartmann wavefront sensor . . . 89
6-6 Measurement model of the wavefront sensor. . . . 91
6-7 Comparison between the far-field approximation and the measurement model of the wavefront sensor. . . . 93
6-8 Experimental setup used in the static characterization of the varifocal mirror . . . 95

6-9 Static characterization of the elliptical varifocal mirror. 96
6-10 Diameter of the measured laser spot shown alongside the results of the static characterization. 97
6-11 Radius of curvature *RoC* measured by the wavefront sensor during the static characterization. 98
6-12 Deflection curve of the varifocal mirror calculated from the results of the static characterization. 99
6-13 Static characterization with a prefocusing lens. 100
6-14 Deflection curve of the varifocal mirror obtained from 2 datasets. . . 102
6-15 Corresponding focal length of the system f_{sys}. 104
6-16 Expected focusing error. 105
6-17 Relationship between the focusing error and the corresponding variation in the laser spot diameter. 106
6-18 Aberrations Tip Y (Z2) and Tilt X (Z3) induced by the varifocal mirror 107
6-19 Vertical astigmatism (Z6) induced by the varifocal mirror 108
6-20 Other optical aberrations induced by the varifocal mirror 108
6-21 Pictures of the focused beam propagating through a fluorescent medium for different values of mirror deflection 109
6-22 Comparison between the focal length of the mirror calculated from the fluorescent images and the mirror deflection model obtained from the static characterization 110
6-23 Experimental setup used in the thermal characterization of the varifocal mirror 111
6-24 Schematic diagram of the designed reflective fiber-coupler 112
6-25 Fabricated fiber-coupler attached to the delivery arm of the Deka laser system 113
6-26 Characterization of the mirror deflection with and without CO_2 laser irradiation. 114
6-27 Deflection curve of the varifocal mirror with and without CO_2 laser irradiation. 116
6-28 Step response of the system obtained using (a) the microinjection system and (b) the microvalve 118
6-29 Schematic diagram of the proposed fiber laser tool with varifocal mirror-based focusing system. 118

A-1 Schematic diagram of a laser beam reflected by an off-axis parabolic mirror 126
A-2 Schematic diagram of a laser beam entering a glass cuvette and being focused inside water 130

1 Introduction

Today, lasers are used in many surgical interventions due to their ability of performing precise incisions and ablations [1]. This allows surgeons to preserve more healthy tissue, which can be critical for the patient, especially in microsurgical procedures. For example, in vocal cord tumor resection, even 1 mm of additionally resected tissue can result in permanent vocal impairment [2]. Besides that, lasers possess the unique ability to cauterize small blood vessels while cutting, which reduces bleeding during the operation [3]. This avoids complications and increases the safety and performance of the procedure.

One of the main disadvantages of laser tools, however, is that the target site must be accessed by a straight-line trajectory. This poses accessibility issues, especially when the area to be operated cannot be properly exposed. With the development of fiber-coupled lasers, endoscopic laser systems have been proposed, allowing to deliver the laser closer to the target site [4]. These endoscopes provide improved visualization of the surgical site, while expanding the applicability of laser tools to minimally invasive procedures [5].

In order to ensure the precision of the ablation, the laser beam must be focused at the target tissue. To achieve that, traditional laser tools contain focusing units which are able to change the focal length of the beam by translating lenses or mirrors over linear stages. These units can be operated manually or automatically if the distance to the target tissue can be determined. However this approach is not used in fiber laser tools, since these focusing units are too large and bulky to be integrated in an endoscopic setup [6, 7].

Instead, fiber tools typically use no optics at all and rely on placing the tip of the fiber in contact with or in close proximity to the tissue being ablated [5]. In this

case, the diameter of the laser spot on the tissue is slightly larger than the core of the optical fiber. This method results in a series of disadvantages including reduced precision [8] and excessive thermal damage to the surrounding tissue, often leading to tissue carbonization [9]. This is bad for the patient as it increases recovery time and post-operative pain and may even reduce function of the tissue after the surgery. To avoid these issues, a compact focusing unit would be necessary.

Instead of miniaturizing standard focusing units, a different approach can be obtained with adaptive optical elements, such as varifocal mirrors. Varifocal mirrors are mirrors whose curvature can be dynamically controlled in order to change the focal length of the laser beam. Since they do not require physical displacement, they allow for more compact focusing systems. On the last decade, several types of MEMS (microelectromechanical systems) varifocal mirrors have been proposed for imaging systems, such as confocal microscopy and OCT (optical coherence tomography) [7]. However until now, this technology has not been used for controlling high-power laser systems. We believe this to be a promising approach to improve the precision and safety of fiber laser tools.

1.1 Technical and Scientific Challenges

Varifocal mirrors have already been proposed for imaging [7] and material processing [10] applications. Even though the principle of the focusing task in these applications is the same as in tissue ablation – the mirror deflects to change the focal length of the reflected beam – the technical requirements are quite different. In imaging systems, the mirror must be compact and fast, but the power of the laser beam is in the order of 70 mW. This allows using MEMS membrane mirrors with a few millimeters of diameter and a few microns of thickness. These mirrors are usually deflected with electrostatic [11] or piezoelectric [12] actuation, which provide operating frequencies in the range of kHz, but results in limited deflection.

For material processing, the power of the laser beam can reach 2 kW, but the size of the mirror is usually not a constraint. To deal with the high-power laser, these mirrors are made from clamped thick membranes with large diameter and deflection is generated by hydraulic actuation [10]. The large thickness of the membrane results in very limited deflection, however the required optical power range is typically low, since the minimal focal length of the beam is in the order of 100 mm.

For tissue ablation, the mirror must be compact and must withstand a surgical laser beam with at least 3W of power. Imaging mirrors are not suitable for that, because their low aperture and thin membrane makes them too sensitive to thermal effects caused by the high-power laser irradiation. On the other hand, thick mirrors such as the ones used for material processing do not provide enough deflection. Therefore focusing a high-power laser for tissue ablation requires a new type of varifocal mirror.

To reduce the thermal sensitivity of the mirror and make it withstand the high-power laser, it is necessary to limit the heating of the mirror by increasing the heat dissipation on it. This can be achieved by using a mirror with large aperture. However, the required deflection to achieve a certain optical power increases with the diameter of the mirror. Therefore, to achieve large deflection on a large aperture mirror, we need an actuation mechanism capable of applying large pressure, such as hydraulic actuation. Moreover, hydraulic actuation helps cooling the mirror, which reduces its thermal sensitivity even further. Based on this analysis, our proposed design of varifocal mirror for tissue ablation consists on a large aperture MEMS varifocal mirror with hydraulic actuation.

Since MEMS varifocal mirrors have not yet been explored with high-power lasers, neither with hydraulic actuation, this proposal raises several questions:

- How does hydraulic actuation compare to other actuation mechanisms – such as electrostatic and piezoelectric – in terms of maximum deflection, precision, optical quality and actuation speed?
- Is hydraulic actuation enough to prevent thermal damage on a MEMS varifocal mirror? Can the thermal sensitivity of the mirror be reduced to a point where the mirror deflection can be precisely controlled even under high-power laser irradiation? How large the mirror must be for that?
- Is this a suitable solution for the focusing problem on fiber laser tools? How does this approach compare to the near-contact ablation in terms of precision and safety?

The main goal of this thesis is to investigate this problem by developing a novel varifocal mirror and a proof-of-concept focusing system.

1.2 Contributions of the Thesis

This thesis presents a novel MEMS varifocal mirror with hydraulic actuation, for high-power laser focusing. The development of such mirror comprised the theoretical work of modeling and simulation of the laser focusing task as well as the experimental work of design and fabrication of the varifocal mirror. This required interdisciplinary research involving four disciplines: Optics, Microfabrication, Mechatronics Design and Control Theory.

From the theoretical work, two main contributions were achieved. The first one is the development of a model for the deflection of a varifocal mirror under high-power laser irradiation. Even though the deflection of circular and elliptical membranes is a well-known problem, it does not have a closed-form solution [13]. Solutions presented in the literature are based on approximations [14] or numerical simulations [15]. In this thesis, we review some of the most used approximations

and extend them to incorporate the thermal effects caused by the high-power laser irradiation. This allows us to predict the membrane behavior under high-power laser irradiation and to understand how the mirror design affects its thermal sensitivity.

The second theoretical contribution is the modeling of the laser focusing task as a control problem. This allows us to calculate the sensitivity of the focusing task to the parameters of the laser and the varifocal mirrors. It also brings us to the following counter-intuitive conclusion: to keep the laser spot diameter constant when ablating tissue at variable distance, the focal length of the beam must be different from the distance to the tissue, in order to compensate the variation of the numerical aperture of the beam. The proposed model allows us to calculate the required focal length of the beam based on the distance to the tissue and the parameters of the focusing system.

Finally, the design of the varifocal mirror with hydraulic actuation is also novel as, to the best of our knowledge, this is the first time this actuation mechanism is used to control the deflection of a MEMS varifocal mirror. Despite its advantages for the proposed application, the hydraulic actuation poses new constraints to the mirror fabrication process, since the membrane must be contiguous (without any holes). After investigating different processes for dry and wet etching of silicon, we obtained a complete fabrication process for building the mirrors from a single silicon wafer.

1.3 Outline of the Thesis

This thesis is organized as follows:

Chapter 2 presents the theoretical background of the thesis. It describes the fundamentals of laser technology, laser beam focusing and laser-tissue interactions. It also presents clinical applications of lasers and compares different methods for delivering laser to the surgical site. This comparison is used to present the laser focusing problem in fiber tools in more detail.

Chapter 3 reviews the state of the art of varifocal mirrors. It presents the main actuation mechanisms of varifocal mirrors, describing their operating principle and comparing the performance of mirrors presented in recent works. At the end of this chapter, we compare the actuation mechanisms in the context of laser focusing for tissue ablation.

Chapter 4 presents mathematical models and simulations of laser beam focusing with a varifocal mirror. We begin this chapter reviewing the membrane deflection theory and extending it to account for thermal effects of the high-power laser irradiation over the mirror. Then we present a mathematical formulation of the laser focusing task as a control problem and derive a feed forward controller for the varifocal mirror to ensure precise focusing.

Chapter 5 presents the microfabrication process used to create MEMS varifocal

mirrors for hydraulic actuation. We describe all the steps of the fabrication process and how they are related to the mirror design. We also present fabricated prototypes of circular and elliptical mirrors.

Chapter 6 presents experiments performed to characterize the fabricated varifocal mirrors. These experiments analyze the mirror deflection in terms of maximum range, optical quality, thermal effects and dynamic behavior. We also demonstrate the focusing of the laser beam, by analyzing its propagation through fluorescent medium.

Chapter 7 concludes the thesis by summarizing the obtained results and presenting directions for future work.

This thesis also has an **Appendix A**, which shows the mathematical derivations for some of the formulas used throughout the thesis.

2
Laser Surgery Fundamentals

Surgical laser tools are now common in the operating room, being used in several types of surgical procedures. The technology that has enabled that, the laser, has been invented by Theodore H. Maiman in 1960 and has drastically evolved since then. Today lasers can be used to perform very complex and precise procedures such as eye surgery or tumor ablation. This is possible due to decades of research on fields such as fundamental properties of laser light, laser-matter interaction and advanced optics. In the first part of this chapter, we review the state-of-the-art of these three topics, presenting the concepts required to understand the process of tissue ablation using lasers.

In its second part, we present clinical applications of lasers, with emphasis on laser phonomicrosurgery, which is the main application of this research project. We also present different types of laser systems used in surgery (the free-beam and the fiber system) and compare theirs benefits for this type of procedure. Finally, we present a detailed description of the open problems with existing fiber laser tools, which served as motivation for this project.

2.1 Laser Fundamentals

Laser is an acronym that stands for *light amplification by stimulated emission of radiation*. It is used to describe both the physical process and the devices based on it for generating a highly directional monochromatic light beam. This beam can be distinguished from other light sources for presenting high spatial and temporal coherence, which are a consequence of its operating principle [16].

When light travels through a medium it interacts with its atoms resulting in

different phenomena. The most common one is absorption, when a photon of the beam is annihilated to promote the energy level transition of an electron. Later on, the excited electron transitions to a lower energy level, emitting a new photon in the process. The exact time of this spontaneous emission, as well as the direction of the emitted photon are random. However, when an excited electron collides with a photon whose energy level corresponds to the gap between the energy levels of the electron, stimulated emission occurs. In this case, the emitted photon has the same energy, direction and phase of the original photon [16]. These three phenomena are illustrated in Fig. 2-1.

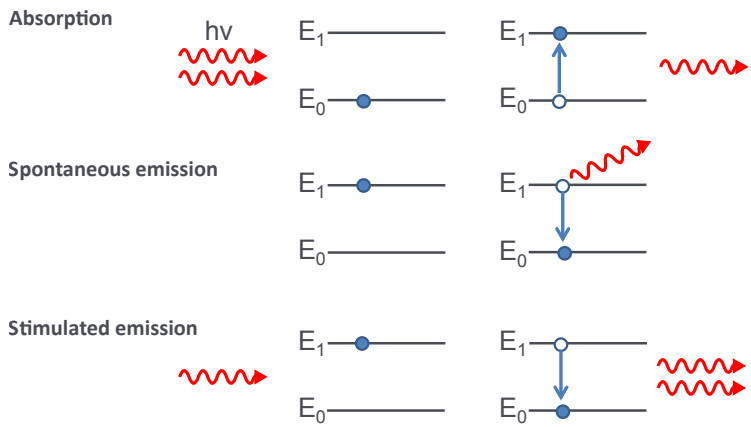

Figure 2-1: Stimulated emission of radiation effect, which occurs when a photon interacts with an excited electron. (Source: [17])

In normal conditions, the energy obtained from spontaneous and stimulation emission equals the absorbed energy. However in an active medium with population inversion – which contains more electrons in high energy than low energy states – stimulated emission becomes dominant [16]. This state can be obtained by pumping energy into the system using an optical or an electrical pump. In this condition the active medium becomes an optical amplifier.

Laser devices take advantage of this effect, by placing the active medium in a resonant cavity as shown in Fig. 2-2. Using two parallel mirrors, photons can pass through the medium multiple times, creating a stationary wave. If the length of the cavity is an integer multiple of the wavelength of the emitted photons, the stationary wave suffers constructive interference, increasing in energy over time. If one of the mirrors is a partial reflector, light can exit the cavity as a highly directional beam.

The reason the beam is highly directional (also called spatially coherent), is because only the photons traveling parallel to the axis of the cavity get amplified. On the other hand. its high monochromaticity (also called temporal coherence), is due to the fact that the energy of the emitted photons all correspond to the energy level of the transitions that occur in the active medium, which depends on the material of the medium. Ideally this would mean all photons would have the same wavelength,

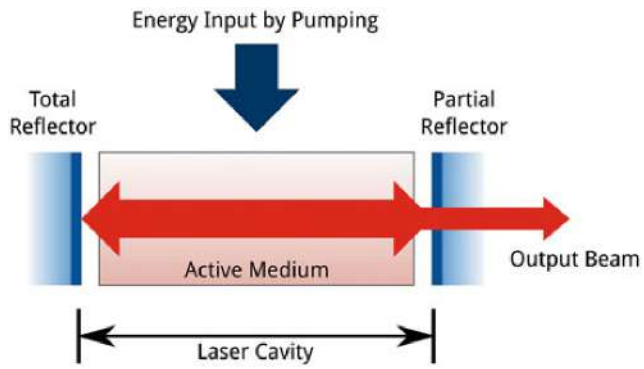

Figure 2-2: Schematic diagram of a laser device. (Source: [18])

but in practice their frequencies are distributed over a central value, due to natural broadening. However the length of the resonant cavity determines which frequencies get amplified. Therefore it is possible to design the cavity so that only one or a few frequencies fall within the band gap of the natural broadening. These selected frequencies are called the longitudinal modes of the cavity.

Besides their frequency spectrum, laser beams are also qualified for their Transverse Electromagnetic Mode (TEM). In the same way the length of the cavity defines the longitudinal mode, the width and the shape of the walls of the cavity define which modes can be amplified in the transverse direction. Fig. 2-3 shows some transverse modes that can be generated in cylindrical and rectangular cavities.

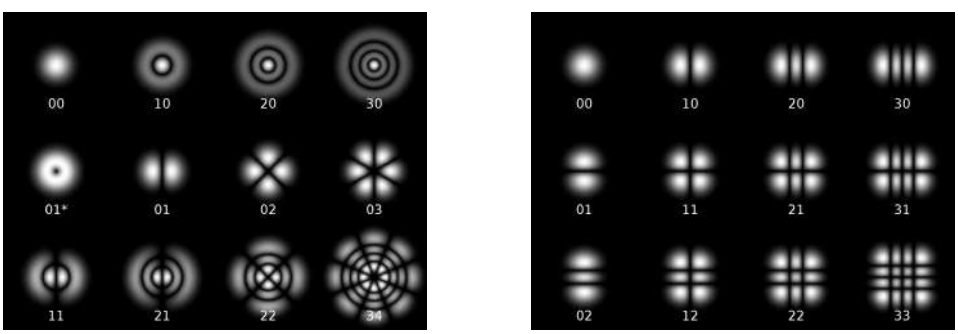

(a) (b)

Figure 2-3: Transverse modes of a laser beam in a cylindrical (a) or a rectangular (b) cavity.

As it can be seen, low order modes have energy more concentrated, therefore are easier to focus than high order modes. For this reason, most laser systems have low TEM. In particular the TEM_{00}, also known as Gaussian beam, has the smallest possible divergence, therefore the maximum focusing power. It also has another interesting property that when a Gaussian beam traverses a lens, the output beam is also Gaussian.

2.2 Laser Beam Optics

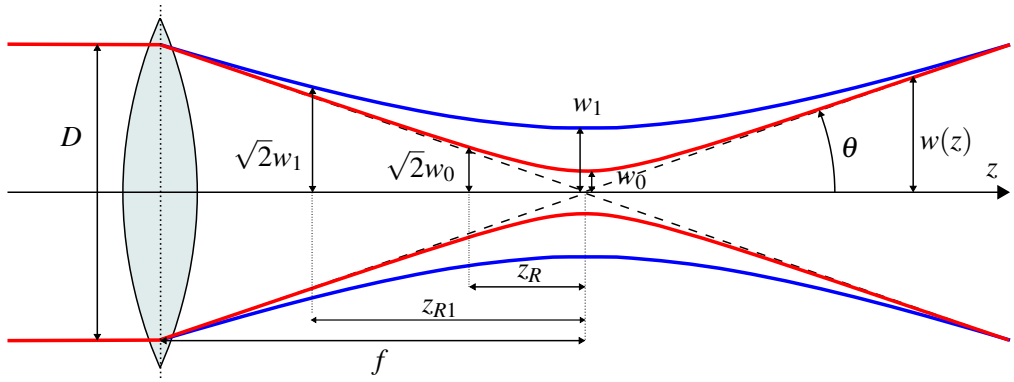

Figure 2-4: Propagation of a focused Gaussian beam in free space.

When a Gaussian beam is focused, its diameter decreases to a minimum at the focal point or waist location, as shown in Fig. 2-4. At this point the radius of the beam is equal to w_0, which is called the beam waist. This parameter completely determines the beam and allows calculating its propagation over free-space as:

$$w(z) = w_0\sqrt{1+\left(\frac{z}{z_R}\right)^2}, \tag{2.1}$$

where $w(z)$ is the radius of the beam at a distance z from the waist and z_R is called the Rayleigh range of the beam and is given by

$$z_R = \frac{\pi w_0^2}{\lambda}, \tag{2.2}$$

with λ being the wavelength of the beam. The Rayleigh range corresponds to the distance from the waist where the beam radius becomes $\sqrt{2}w_0$ and it determines the depth of focus ($b = 2z_R$) of the beam. On the far-field, the propagation of the beam becomes conical, with a divergence angle of

$$\theta = \frac{\lambda}{\pi w_0}. \tag{2.3}$$

Due to the paraxial approximation, the far-field divergence equals the numerical aperture of the beam, which means $\theta = NA = D/2f$. Therefore, the beam waist can be calculated as

$$w_0 = \frac{\lambda}{\pi}\frac{1}{NA} = \frac{\lambda}{\pi}\frac{2f}{D}. \tag{2.4}$$

If the beam is not perfectly Gaussian, it presents larger divergence, resulting in

a larger beam waist [19]. For this case, we can compute the beam quality factor M^2 as

$$M^2 = \frac{\pi}{\lambda} w_1 \theta, \tag{2.5}$$

which corresponds to the beam parameter product (BPP) of the beam ($w_1\theta$) divided by the BPP of the Gaussian beam (λ/π). From this definition, $M^2 = 1$ for a Gaussian beam and $M^2 > 1$ for all other beams. From equation 2.5, we can calculate the beam waist of a non-Gaussian beam as

$$w_1 = M^2 \frac{\lambda}{\pi} \frac{1}{\theta} = M^2 w_0. \tag{2.6}$$

The propagation of a non-Gaussian beam is given by an equivalent equation to 2.1:

$$w(z) = w_1 \sqrt{1 + \left(\frac{z}{z_{R1}}\right)^2} \tag{2.7}$$

with the new Rayleigh range z_{R1} given by

$$z_{R1} = \frac{\pi w_1^2}{M^2 \lambda}. \tag{2.8}$$

Another important parameter to characterize a Gaussian laser beam is the radius of curvature *RoC* of the wavefront of the beam. At the waist, the wavefront of the beam is flat, therefore the radius of curvature is infinite. As the beam propagates in free space, it starts diverging and its wavefront becomes curved. The relationship between the radius of curvature of the wavefront and the distance to the beam waist is given by:

$$RoC(z) = z \left[1 + \left(\frac{z_R}{z}\right)^2\right], \tag{2.9}$$

2.2.1 Laser Beam Propagation

When a Gaussian beam propagates in free space, its diameter and radius of curvature vary with the propagation distance z according to the 2.1 and 2.9, respectively. However, when it travels through an optical element, such as a thin lens, its wavefront suffers a phase shift, changing the propagation equations. In this case, it is better to express the propagation of the beam using ray tracing techniques [20]. For that, we must first define the complex beam parameter q of the Gaussian beam as:

$$\frac{1}{q(z)} = \frac{1}{RoC(z)} - i \frac{\lambda}{\pi w^2(z)} \tag{2.10}$$

This parameter encodes the radius of curvature and the beam diameter in a single complex variable, allowing us to fully represent the state of the propagating laser beam. When the beam travels through an optical element, the evolution of its beam parameter is given by

$$\begin{pmatrix} q_2 \\ 1 \end{pmatrix} = k \begin{pmatrix} A & B \\ C & D \end{pmatrix} \begin{pmatrix} q_1 \\ 1 \end{pmatrix}, \tag{2.11}$$

where the 2x2 matrix represents the phase shifting of the optical element. This matrix is called *ray transfer matrix*, but it is often referred to as ABCD matrix. The term k in the 2.11 is a normalization constant used to keep the second element of the ray vector equal to 1. The solution to this equation is given by:

$$\frac{1}{q_2} = \frac{C + D/q_1}{A + B/q_1}. \tag{2.12}$$

Once q_2 is determined, the radius of curvature and diameter of the propagated beam can be extracted from the real and complex parts of q_2, respectively. The ABCD matrices for simple optical elements have been reported in the literature [21]. For example, the matrices representing a thin lens with focal length f or the free space propagation over a distance d are given by:

$$\text{Thin lens:} \qquad M_{lens} = \begin{pmatrix} 1 & 0 \\ -\frac{1}{f} & 1 \end{pmatrix} \tag{2.13a}$$

$$\text{Free space:} \qquad M_{free} = \begin{pmatrix} 1 & d \\ 0 & 1 \end{pmatrix} \tag{2.13b}$$

If the beam travels through multiple optical elements in succession, 2.11 can be applied for each element. Alternatively, the ABCD matrix of the complete optical system can be obtained simply by multiplying the matrices of each optical element in the reverse order that they occur in the system. For example, if the beam travels through a thin lens, then propagates through free space, the ABCD matrix that represents this transformation is given by:

$$M_{comb} = M_{free} M_{lens} = \begin{pmatrix} 1 - \frac{d}{f} & d \\ -\frac{1}{f} & 1 \end{pmatrix} \tag{2.14}$$

2.2.2 Optical Aberrations

The equations presented above allow modeling the focusing of a laser beam with an ideal optical system. However real optics rarely produce focal spots as small as the theoretical beam waist, due to imperfections in the lenses, that cause deviations in the optical path of the beam. These deviations are called optical aberrations an they

can distort the beam in several ways. Fig. 2-5 illustrates the most common types of optical aberrations.

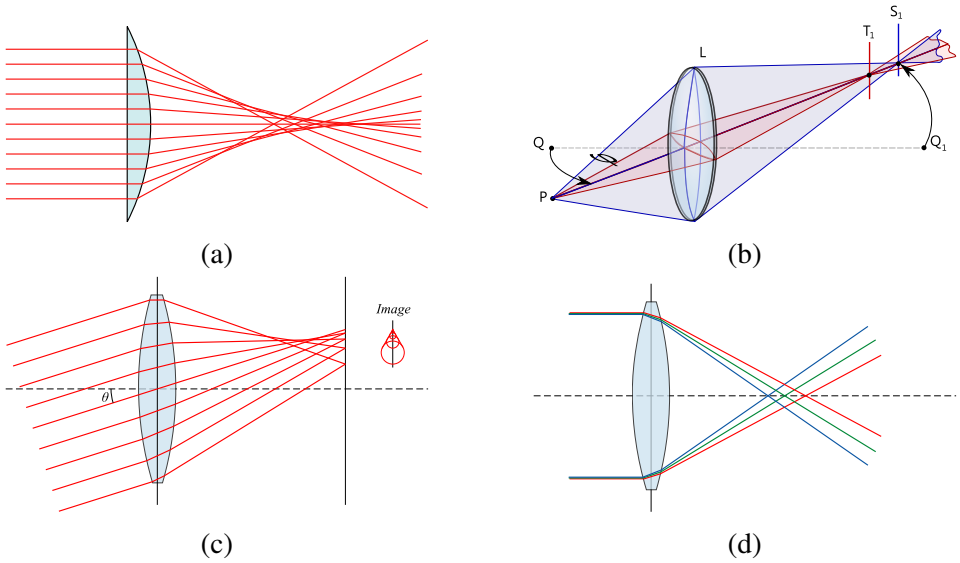

Figure 2-5: Common optical aberrations in focusing systems: (a) spherical aberration, (b) astigmatism, (c) coma and (d) chromatic aberration.

One of the most common types of aberration is the spherical aberration. It happens in lenses or mirrors when rays passing close to the edges of the optics are focused at a different distance than the ones passing through its center. Because of that, there is no single point where all rays are focused, which means that the cross-section of the beam at any point in the ”focal” region is larger than the expected beam waist.

Other common aberrations include astigmatism and coma. In astigmatism, the focal length of the beam in the X and Y directions are different, which also means the beam is not entirely focused in one position. In this case, the cross-section of the beam becomes elliptical. Coma, in the other hand, happens when the beam is not parallel to the axis of the optics, resulting in a focal spot with a comet like shape. Lastly chromatic aberration occurs when different wavelengths are focused at different focal lengths. This effect happens in lenses, since the refractive index of the lens material is wavelength dependent.

These aberrations decrease the optical quality of the beam, thus hindering the focusing properties of the system. They can be eliminated by using aberration free optics, such as aspheric lenses, which are often expensive, or by combining several optical elements so that their aberrations cancel each other. This is the principle used in complex optical systems, such as objective lenses.

Table 2.1: Zernike Polynomials

Coefficient	Zernike Polynomial	Associated Aberration
Z_0^0	1	Piston
Z_1^{-1}	$2\rho sin\theta$	Vertical tilt
Z_1^1	$2\rho cos\theta$	Horizontal tilt
Z_2^{-2}	$\sqrt{6}\rho^2 sin2\theta$	Oblique astigmatism
Z_2^0	$\sqrt{3}\left(2\rho^2-1\right)$	Defocus
Z_2^2	$\sqrt{6}\rho^2 cos2\theta$	Vertical astigmatism
Z_3^{-3}	$\sqrt{8}\rho^3 sin3\theta$	Vertical trefoil
Z_3^{-1}	$\sqrt{8}\left(3\rho^3-2\rho\right) sin\theta$	Vertical coma
Z_3^1	$\sqrt{8}\left(3\rho^3-2\rho\right) cos\theta$	Horizontal coma
Z_3^3	$\sqrt{8}\rho^3 cos3\theta$	Oblique trefoil
Z_4^{-4}	$\sqrt{10}\rho^4 sin4\theta$	Oblique quadrafoil
Z_4^{-2}	$\sqrt{10}\left(4\rho^4-3\rho^2\right) sin2\theta$	Oblique secondary astigmatism
Z_4^0	$\sqrt{5}\left(6\rho^4-6\rho^2+1\right)$	Spherical aberration
Z_4^2	$\sqrt{10}\left(4\rho^4-3\rho^2\right) cos2\theta$	Vertical secondary astigmatism
Z_4^4	$\sqrt{10}\rho^4 cos4\theta$	Vertical quadrafoil

2.2.3 Quantifying Optical Aberrations

The beam quality factor M^2 is an aggregated representation of all the aberrations present in the beam. However each optical aberration impacts the shape of the focal spot and the beam propagation in a different way, therefore it is necessary to describe them quantitatively. To achieve that, we can describe the wavefront of the laser beam as sum of Zernike polynomials [22].

Zernike polynomials are orthogonal on the unit disk and can be easily normalized to create an orthonormal base to describe a 3D surface. Table 2.1 presents a list of the Zernike polynomials up to the fourth order in polar coordinates. The main advantage of using this parametric representation of the wavefront is that each Zernike coefficient is related to one type of optical aberration. For example, the coefficients Z_2^{-2} and Z_2^2 represent the first order astigmatism in the vertical and oblique direction, while Z_4^0 represents the first order spherical aberration. The coefficient Z_2^0 represents the defocus of the beam and allow us to calculate the focal length of the beam from the measurement of its wavefront at a single point. Fig. 2-6 illustrates the surface shape described by each Zernike polynomial.

Using this representation, we can quantify each optical aberration by its corresponding Zernike coefficient, which allows direct comparison of individual aberrations in different systems. Moreover, since the set of Zernike coefficients provide a complete representation of the beam, it is possible to calculate the beam quality factor M^2 directly from the Zernike coefficients [23].

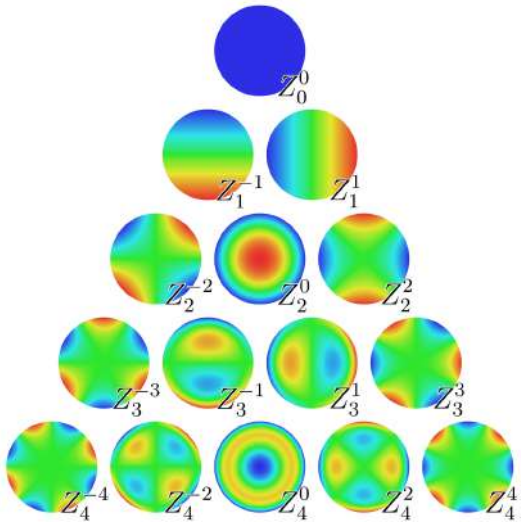

Figure 2-6: Zernike polynomials on the unit circle up to the fourth order.

2.3 Laser-Matter Interaction

When a laser beam is incident on a material, several types of interactions may occur, as illustrated in Fig. 2-7. The three basic interactions are: reflection, transmission and absorption. Reflection occurs when the direction of propagation of the beam is changed at the surface of the material, preventing the beam from penetrating it. Transmission, on the other hand, occurs when the beam is able to travel through the material. In this case, the direction of propagation is changed at the interface of the material due to refraction. The directions of the reflected and refracted beams can be determined using the Fresnel's Equations [24]. Finally, absorption occurs when the energy of the laser beam is absorbed by the atoms of the material, usually going to its electrons. This effect can induce different reactions on the material depending on the energy absorbed, and is the main mechanism through which lasers can be used to manipulate matter.

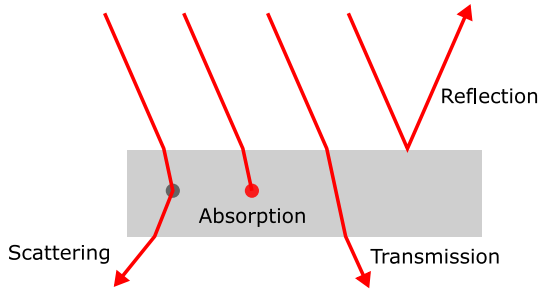

Figure 2-7: Basic interactions between laser light and matter.

In most real cases, all these effects happen simultaneously, but in different pro-

portions. This means that the energy of the incident beam is divided into the reflect beam, the transmitted beam and the absorbed portion. For uniform materials, the energy proportion between those beams is defined by the coefficients of reflectance, transmittance and absorbance. These coefficients are wavelength-dependent, which means that a material can be transparent for a certain wavelength and opaque to another. These coefficients also depend on the angle of incidence and on the polarization of the light.

In non-uniform materials, the direction of the laser beam can also be changed inside the material, due to reflection and refraction at each non-uniformity present. This effect is called scattering. Due to its random nature, scattering results in spreading of the beam in all directions, effectively causing the scattered energy to be lost in the material. In this case, the total energy of the beam lost in the material can be expressed in terms of attenuation, which comprises both absorption and scattering.

2.3.1 Interaction with Biological Tissue

In biological tissue, absorption and scattering are the dominant effects. Absorption can lead to physical and chemical changes at the tissue causing different types of interactions, as shown in Fig. 2-8. The main factors to determine the nature of the interaction that occurs are the power density of the beam and the exposure time [25].

At low energy levels photochemical interactions occur. One example of this type of interaction is photodynamic therapy (PDT), in which laser pulses are used to activate an injected photosensitizer [26]. When the power density increases, the laser beam is able to increase the temperature of the tissue, leading to thermal interactions. This results in several effects, which are described in detail in the next section. At even higher power densities, ultra fast lasers with femtosecond pulses are able to interact with tissue, leading to photodisruption, photoablation and plasma-induced ablation. These phenomena are so fast that they can break the molecular structure of the tissue without even heating it up. This enables very localized effects, allowing even to ablate tissue underneath the surface [27].

2.3.2 Thermal Interactions

Thermal interactions correspond to the largest group of interactions and one of the most used in medicine. This is due to their usefulness in ablating tissue, as well as the ease to achieve their parameters. This interaction happens for laser pulses with duration from 1 µs to 1 min, which means the laser can be used even in continuous mode, for a few seconds. The power density is between 10 and 10^6 W/cm^2, which means a laser power of few watts can be used if the beam is focused at submillimiter spot. Most commercial laser systems ablate tissue with thermal interactions.

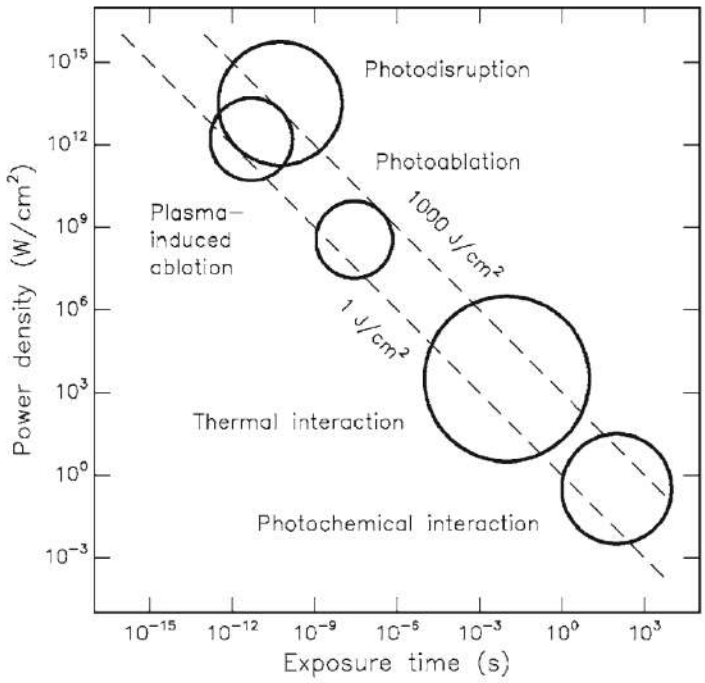

Figure 2-8: Laser-tissue interaction types as a function of the exposure time and the power density of the beam. (Source: [18])

When tissue heats up, different effects can happen, depending on the temperature. Table 2.2 lists these effects. For temperatures bellow 60 °C, no permanent damage occurs, assuming the heat increase only persists for a few seconds. Above 60 °C, tissue coagulation occurs. At 100 °C, the water inside the cells vaporizes. This results in a quick expansion in the cell volume, leading to an explosion of the cell, which results in tissue removal. This process is called ablation by vaporization. If irradiation persists and the temperature surpasses 100 °C, carbonization occurs. This phenomenon consists on the formation of rigid scars that can be identified by blackening of the tissue and the release of smoke. Finally, if temperature reaches 300 °C, tissue may even melt.

Both coagulation and vaporization are useful effects in surgical procedures. While vaporization is used to ablate tissue, coagulation can be used to close small blood vessels. This reduces bleeding during the ablation. Carbonization is often negative, as it cause tissue necrosis, creating rigid scars, which decrease the function of the tissue.

When tissue is irradiated with laser, heating happens due to absorption of the laser beam, but also due to heat conduction inside the tissue. This creates a temperature gradient within the tissue, which means that several thermal effects may happen at the same time. For example, when tissue is vaporized, the surrounding tissue usually suffers coagulation or at least hyperthermia. A small layer of car-

Table 2.2: Thermal Effects

Temperature (°C)	Thermal Effect
37	None
45	Hyperthermia
50	Reduction of enzyme activity, cell immobility
60	Denaturation of proteins and collagen, coagulation
80	Permeabilization of membranes
100	Vaporization
>100	Carbonization
>300	Melting

bonized tissue is also common around the ablated tissue, depending on the power of the laser beam. This is illustrated in Fig. 2-9.

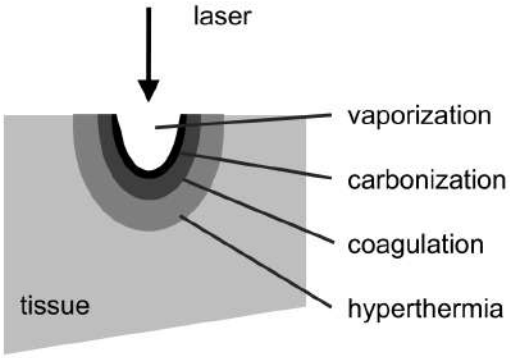

Figure 2-9: Thermal effects that occur in biological tissue during thermal ablation. (Source: [28])

2.4 Clinical Applications

Due to its ability to generate localized effects on biological tissue, one of the first applications of lasers was as a surgical tool. In 1962, only two years after the creation of the first laser, lasers were used in dermatology, for removing skin tattoos [29]. Since then, the use of lasers in medicine has expanded to virtually all types of surgical procedures, including fields such as neurology [30], urology [31], ophthalmology [27] and otolaryngology [32].

One example of surgical procedure in which the laser is an essential tool is phonomicrosurgery, which consists in the treatment of abnormalities in the larynx, including larynx tumor resection [33]. In this procedure, the structures being manipulated are very delicate and preserving healthy tissue is critical for the patient,

as it impacts his ability of swallowing and speech. However, the confined environment of the larynx makes difficult to manipulate cutting tools with precision. For this reason, the laser is used as a scalpel, as shown in Fig. 2-10.

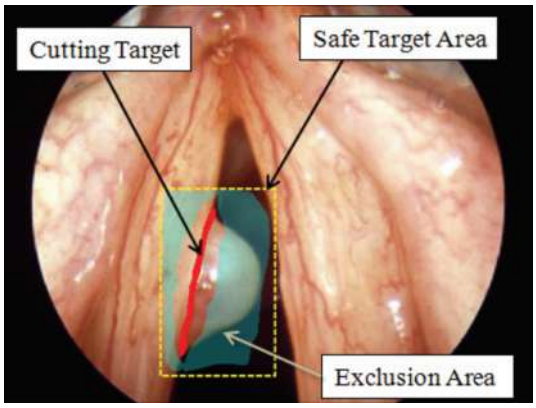

Figure 2-10: Laser phonomicrosurgery for vocal cord tumor resection. (Source: [33])

The main advantages of the laser, when compared to other incision tools such as the rigid scalpel are its ability to perform precise cuts and to coagulate small blood vessels while cutting (hemostatic effect). When compared to tools that provide comparable hemostasis, such as the monopolar and bipolar electrosurgery, the laser offers the advantage of performing contactless ablation, which avoids tissue sticking [34]. Among all types of lasers, the CO_2 is the one that provides minimal collateral damage, when ablating soft tissue.

2.4.1 Laser Delivery Systems

Fig. 2-11a illustrates the typical setup of a laser phonomicrosurgery using a free-beam laser system. In this system, the laser is delivered to the target tissue by an articulated arm, containing a series of mirrors. The surgeon manipulates the laser by operating a micromanipulator, which controls the tip and tilt angles of the last mirror of the series. The main limitation of this system is that the target tissue must be reached by a straight line trajectory, requiring direct exposure of the larynx using a rigid laryngoscope. This limits the areas that can be accessed and often poses ergonomic issues for the patient, sometimes making the procedure unfeasible.

To overcome these problems, flexible delivery systems have been proposed [5]. In these systems, the laser beam is delivered through an optical fiber or hollow core waveguide, allowing the laser to be delivered much closer to the target tissue. This allows integrating the laser tool in an endoscopic setup, as illustrated in Fig. 2-11b. This new approach provides better visualization of the tissue being operated and allows using lasers even in minimally invasive procedures.

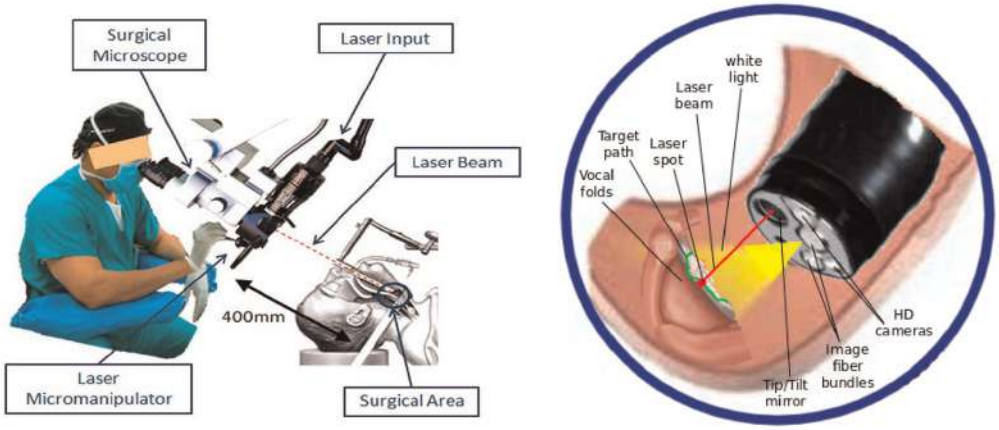

(a) (b)

Figure 2-11: Laser delivery systems: (a) free-beam system and (b) optical fiber. (Source: [35])

Even though both the free-beam and the fiber systems can use the same type of laser (e.g. CO_2), the ablation method used in these systems are different. In free-beam systems, the collimated beam is tightly focused on the target tissue, producing a laser spot as small as 100 µm. As the laser spot is moved over the target tissue, the focal length of the beam is manually adjusted by the surgeon by moving the focusing lens or mirror.

In fiber laser tools, this approach is not used, since focusing units are too large and bulky to be integrated in endoscopic system. Instead of that, the optical fiber is placed in direct contact with or very close to the target tissue. In this case, the laser spot becomes slightly larger than the core of the fiber. The smallest fibers for CO_2 provide a spot size of 250 µm, but most fiber systems work with spot sizes of 500 µm.

2.4.2 Open Challenges with fiber laser tools

Despite fiber laser tools being very intuitive – since the surgeon steers the laser tool over the tissue as a scalpel – the near-contact ablation method has notable disadvantages when compared to focused ablation. First, the laser steering precision is limited by the surgeon's dexterity, while in the free-beam system a robotic steering device can be used to provide features such as motion scaling and tremor compensation [36]. Secondly, the close proximity or the contact of the fiber tip with the tissue hinders the visualization of the tissue being ablated and increase the risk of contamination while ablating a tumor. Finally, the lack of optics in the fiber tool prevents the use of fast scanning of the laser spot, which causes excessive thermal damage to the surrounding tissue often leading to tissue carbonization. This has been verified

by comparative studies showing that focused ablation provides better precision and less carbonization than near-contact ablation, even when laser scanning is not used [8]. These results are illustrated in Fig. 2-12.

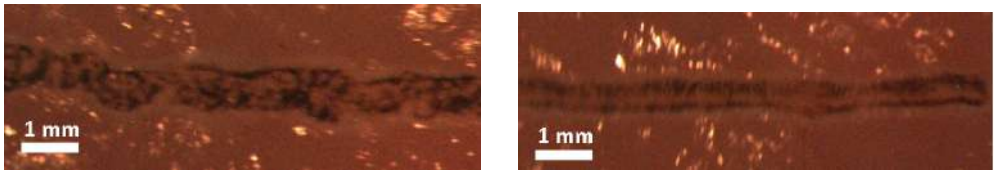

(a) (b)

Figure 2-12: Comparison of ablated tissue in contact (a) and focused (b) modes. The black pixels represent carbonized tissue. (Source: [8])

In order to reduce the tissue carbonization and increase the precision of the ablation in fiber laser systems, it is necessary to integrate a focusing system with adjustable focal length in the fiber laser tool. This is challenging due to the limited space in the fiber tool. Even using miniaturized actuators such as the squiggle motor [37], systems based on moving lenses or mirrors still require large space to provide significant focal length variation.

An alternative approach to solve this problem is to control the focal length of the beam using varifocal mirrors, as illustrated in Fig. 2-13. Varifocal mirrors can bend dynamically, changing their focal length without the need of physical displacement. Using micro and nanofabrication technology, they can be made arbitrarily small. Over the last decade, several MEMS varifocal mirrors have been proposed for microscopy applications, such as confocal microscopy and OCT [7]. However until the present moment, such technology has not been used with high-power lasers.

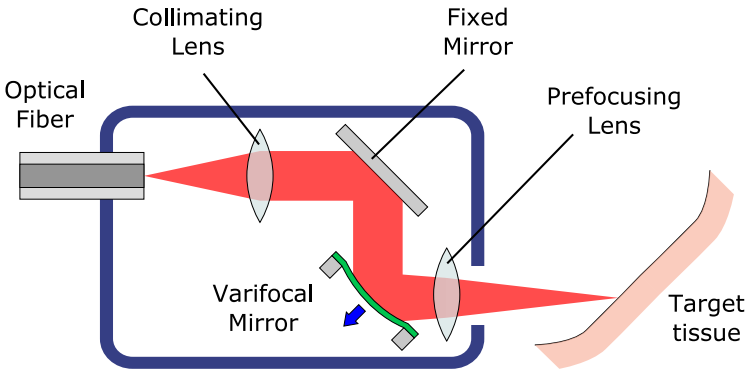

Figure 2-13: Proposed focusing system with variable focal length, based on a varifocal mirror.

2.5 Conclusion

Lasers are powerful surgical tools as they provide increased safety and precision for several surgical procedures. However the development of minimally invasive surgery has increased the need of miniaturized surgical tools, in order to perform the procedure with minimal trauma for the patient. Fiber lasers are a key technology to achieve that, as they allow integrating laser tools even in endoscopic systems. However, the performance of fiber laser tools is still lower than traditional free-beam systems, due to the lack of optical systems for focusing and scanning the laser beam.

Adaptive optical devices, such as MEMS varifocal mirrors have the potential to solve this problem, enabling focused ablation to be performed with fiber laser tools. However the design and control of such MEMS devices under irradiation of high-power laser remains a challenge. The next chapter reviews the state of the art of MEMS varifocal mirrors for focus control. It presents the operating principle of such mirrors and compares the advantages and drawbacks of the different actuation mechanisms that can be used to control the mirror deflection.

3

Review of MEMS Varifocal Mirrors

This chapter reviews the state of the art of MEMS varifocal mirrors. It starts by defining varifocal mirrors and comparing their definition to deformable mirrors, a broader class of adaptive optical elements. Then we present the different actuation mechanisms for MEMS varifocal mirrors. For each mechanism, we explain its operating principle, present their main characteristics and review the most relevant works proposed in the literature. At the end of the chapter, we compare the most suitable applications of each type of varifocal mirror, while discussing how suitable each actuation mechanism would be for endoscopic laser surgery.

3.1 Fundamentals of Varifocal Mirrors

The simplest optical elements that can be used for focusing a laser beam are lenses and curved mirrors. The focusing power of a lens or mirror is constant and is determined by its focal length. In the case of lenses, its focal length depends on the curvature of its two surfaces and on its refractive index. In the case of spherical mirrors, its focal length is given as half of its radius of curvature.

When several lenses or mirrors are combined, the focal length of the complete focusing system depends on the focal length of each element, as well as on the distances between them. For example, the combined focal length f of two lenses with aligned optical axes is given by:

$$\frac{1}{f} = \frac{1}{f_1} + \frac{1}{f_2} - \frac{d}{f_1 f_2}, \tag{3.1}$$

where f_1 and f_2 are the focal lengths of each lens and d is the distance between

the two lenses. Therefore, the focal length of this system can be changed simply by changing the distance between the two lenses. This is how focusing units based on moving lenses work. Focusing units based on moving mirrors work similarly, except that the mirrors can be arranged in several different telescopic configurations.

Deformable mirrors, in the other hand, are mirrors whose curvature can be dynamically changed. They contain an array of actuators allowing to deform their surface, changing their focal length as well as compensating for optical aberrations. They were initially proposed for imaging systems in astronomy applications, in order to compensate optical aberrations induced by the atmosphere. Since then, they have been developed for different applications, including microscopy imaging systems and material processing.

Varifocal mirrors are deformable mirrors specially designed for focus control. They have less degrees of freedom (DOF) than standard deformable mirrors (typically 4 or less), allowing to control only the focal length and a few optical aberrations such as spherical. Having few DOFs makes easier to miniaturize the mirror, since few connections are required, and makes the mirror control simpler. High-DOF deformable mirrors are usually controlled in closed-loop, requiring to measure the reflected beam with a wavefront sensor. Varifocal mirrors, however, can be controlled in open-loop, using mathematical models to estimate the mirror deflection. Besides that, being specially designed for focus control, varifocal mirrors can provide large deflections, while the maximum curvature of high-DOF deformable mirrors is usually of a few diopters (around 1 m^{-1}).

Different actuation mechanisms can be used to control the curvature of a varifocal mirror. The next sections present operating principle of each type of actuation mechanism and review some of the most relevant works proposed until now. We separate the varifocal mirrors in two classes: membrane mirrors, which consist of passive membranes deflected by external pressure, and bimorph mirrors, whose curvature can be directly controlled.

3.2 Membrane Mirrors

Membrane mirrors are composed of thin flexible membranes, which are deflected by external pressure. The membranes are completely passive, which means the shape of the mirror is determined by the applied pressure profile. To achieve high flexibility, the membrane thickness typically ranges from 0.5 to 10 µm, which requires using micro or nanofabrication techniques. For this reason, membranes are usually made of silicon or silicon nitride films coated with high-reflectance coating. Other popular choices of membrane material are polymeric films, due to their high flexibility and compatibility with micofabrication processes.

There are two main methods for exerting pressure on membrane mirrors: electrostatic and pneumatic/hydraulic actuation. The next subsections describe each of

these actuation mechanisms.

3.2.1 Electrostatic Mirrors

In electrostatic mirrors, deflection is caused by electrostatic pressure, which is generated by an electric field applied between the membrane and a back plane of electrodes. This operating principle is illustrated in Fig. 3-1. By applying voltage between the membrane and the electrodes placed beneath it, the mirror deflects towards the electrodes, bending in concave shape. The metallic coating of the membrane is usually used as common ground for the voltage applied to all electrodes. The higher is the applied voltage, the higher is the mirror deflection and consequently the shorter is the focal length of the reflected beam. Fig. 3-2 shows some examples of varifocal mirrors with electrostatic actuation reported in the literature.

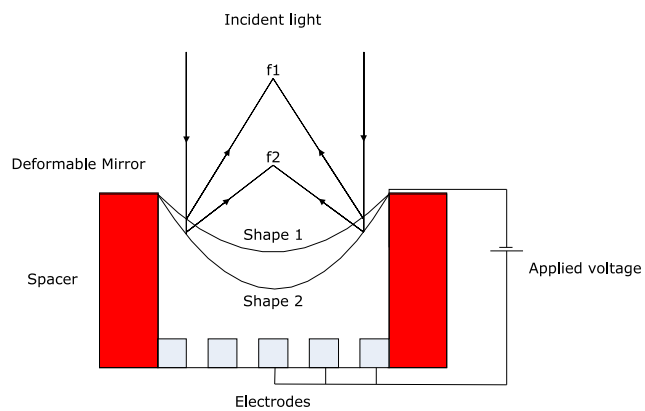

Figure 3-1: Operating principle of varifocal mirrors with electrostatic actuation. (Source: [38])

The electrostatic pressure generated on the membrane can be calculated as:

$$p(r) = \frac{\varepsilon_0 V(r)^2}{2(g - w(r))^2}, \tag{3.2}$$

where g is the gap between the rim of the mirror and the back plate of electrodes, ε_0 is the permittivity of air, $w(r)$ is the obtained deflection of the mirror from its flat shape and $V(r)$ is the voltage profile applied to the electrodes. If a single electrode is used for the entire back plate (e.g. $V(r) = V$) and the mirror deflection is small relatively to the air gap (e.g. $w(r) \ll g$), the electrostatic pressure distribution becomes uniform. This results in parabolic deflection of the mirror [14], which allows focusing a collimated beam without inducing optical aberrations. However, when the deflection of the mirror is large, the pressure distribution becomes non-uniform. In this case, the mirror induces spherical aberration in the focused beam.

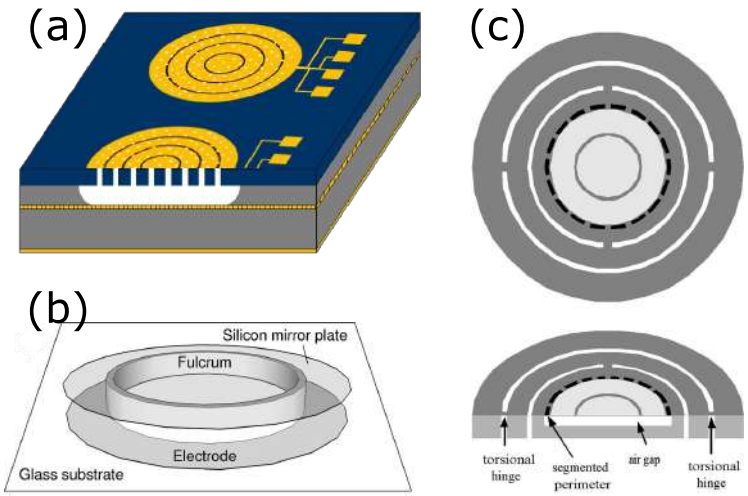

Figure 3-2: Examples of varifocal mirrors with electrostatic actuation. (Sources: (a) [11], (b) [39], (c) [40])

To achieve large deflection, without inducing spherical aberration, a variable voltage profile is needed. The voltage profile that results in parabolic deflection is given by:

$$V_{par}(r) = K\left(g - w_{par}(r)\right), \tag{3.3}$$

where K is a constant determined based on the membrane parameters and $w_{par}(r)$ is a parabolic profile with central deflection $w_{par}(0) = w_0$. Since generating a continuous voltage profile is challenging, electrostatic mirrors often use an array of two [41, 40, 42, 43, 6], three [44, 45, 46, 47] or four [11] concentric electrodes (as shown in Fig. 3-2a). This discrete actuation method does not allow achieving perfect parabolic deflection, but allows compensating for spherical aberration up to its third order, which often results in good optical quality.

The first proposed electrostatic mirrors were made of silicon [39, 48] or silicon nitride membranes [6, 42, 43, 40]. They were fabricated by depositing the membrane on a silicon bulk and releasing it with wet or dry etching. The membrane was typically patterned with micro holes to allow etching the underlying silicon. These micro holes, together with larger holes at the rim of the membrane (as shown in Fig. 3-2c), also allowed to reduce the intrinsic stress of the membrane, increasing the mirror deflection.

To achieve even larger deflection, more recent mirrors use polymeric membranes made from SU-8 2002 [44, 45, 46, 49, 50, 47, 11]. The fabrication methods used for these mirrors include dry and wet etching, but also wafer bonding techniques [44, 45, 49, 50]. Using a wafer bonding process, it is possible to fabricate the membrane and the electrodes on separated wafers and build the mirror by bonding those wafers together. This provides better control over the design of the electrodes

pattern and the structure of the supporting wafer. For example in [50] air holes are created on the support wafer to regulate the damping inside the air gap and optimize the dynamic behavior of the mirror.

One of the main advantages of electrostatic mirrors is their fast actuation. Due to the low mass of the membrane and the low power consumption of the actuation, operating frequencies of electrostatic mirrors can reach up to 87 kHz [39]. Another relevant advantage of this type of mirrors is the simplicity of the actuation mechanism, since the mirror deflection is controlled only by the voltage of the electrodes. This allows easy integration of the mirror with electronic and control systems, as only a few wires must be connected. The voltages used to deflect the mirrors typically range from 100 to 400 V.

One of its main limitations is that the mirror deflection is unidirectional, since the electrostatic force is always attractive. Most electrostatic mirrors only bend in concave direction, however in [39] a convex mirror was developed by supporting the membrane with a ring-shaped fulcrum (as shown in Fig. 3-2b) and applying the electrostatic actuation to the outer portion of the membrane. In this way, as the outer part of the membrane is pulled towards the electrode, its central part bend in convex shape.

Another significant problem is that the mirror deflection is limited by the electrostatic pull-in. As the mirror deflection increases, the distance between the membrane and the electrodes decreases, increasing the electrostatic pressure even further. This creates a positive feedback on the mirror actuation, eventually causing the membrane to touch the electrodes and collapse (snapdown effect). To avoid snapdown, the mirror deflection is usually limited to 44% of the air gap [41].

Due to these limitations and the weak nature of electrostatic force, the maximum reported stroke obtained by electrostatic mirrors was 3.5 µm for silicon nitride membranes [40] and 16.7 µm for polymeric membranes [46] Since the optical power of the mirror is given by $P = {}^{4w_0}/_{R^2}$, this limited stroke ends up limiting the diameter of the mirror that can be used to achieve large optical power range (OPR). Mirrors with small diameter, such as 1 mm, can achieve OPR higher than 40 m^{-1} [39], however larger mirrors with 3 mm of diameter can only reach 21 m^{-1} of OPR [45]. Table 3.1 summarizes the characteristics and compares the performance of the most relevant electrostatic mirrors presented until now.

3.2.2 Pneumatic and Hydraulic Mirrors

In mirrors with pneumatic or hydraulic actuation, the pressure on the membrane is exerted by the fluid itself. This results in two main differences in respect to electrostatic mirrors. The first one is that the pressure distribution on the membrane is always uniform, regardless of the mirror stroke. This results in parabolic deflection of the mirror, which avoids spherical aberration. The second difference is that the membrane design must be contiguous (without any holes), since the fluidic cham-

Table 3.1: Comparison of varifocal mirrors with electrostatic actuation

Reference	**Year**	**Diameter (mm)**	**OPR (m^{-1})**	**Actuation Voltage**	**Max Freq**
Dickensheets et al. [48]	1999	0.2	160	190	20 kHz
Dickensheets et al. [6]	2000	0.3	204.4	88	-
Himmer et al. [42]	2001	1	25	100	25 kHz
Himmer et al. [43]	2003	1 x 1.414	28.3	141	-
Shao et al. [40]	2004	0.7	114.3	240	-
Dickensheets et al. [41]	2006	1.25	41.5	-	10 kHz
Wang et al. [51]	2007	4.5	20	160	70 Hz
Lukes et al. [44]	2009	2	33.2	120	-
Hokari *et al.* [39]	2009	1	41.3	215	87 kHz
Lutzenberger et al. [45]	2010	3	21.3	415	40 kHz
Lukes et al. [46]	2011	3 x 4.24	21	220	-
Moghimi *et al.* [49]	2012	4	10	305	7 kHz
Moghimi *et al.* [50]	2013	3	17.8	332	25 kHz
Lukes *et al.* [47]	2013	3 x 4.24	18.6	313	500 Hz
Lukes *et al.* [11]	2014	3 x 3.01	7.7	350	222 Hz

ber used to deflect the mirror must be sealed. This poses additional constraints to the fabrication process of the mirror, preventing us to use the same methods of electrostatic mirrors.

To control the pressure in the fluidic chamber, there are two main approaches. The first one is to use a microfluidic channel to pump fluid in and out of the fluidic chamber, causing the mirror to deflect in convex or concave direction. The second approach is to use a different actuation mechanism on an actuation membrane placed at the opposite side of the fluidic chamber. In this way, the fluid is used simply to transfer force from the actuation membrane to the mirror membrane.

There are three benefits of using this approach instead of actuating the mirror membrane directly. The first one is that the pressure distribution on the mirror membrane is uniform regardless of the pressure profile applied to the actuation membrane. This allows using linear actuators, such as a solenoid or a piezoelectric piston. The second one is that the mirror membrane deflection can change from concave to convex, even if the deflection of the actuation membrane is unidirectional, which may be necessary for some applications. Finally the diameters of the actuation and mirror membranes can be designed in order to provide an amplification factor on the actuation, increasing the stroke of the mirror membrane.

Fig. 3-3 shows two examples of varifocal mirrors with pneumatic actuation. In [52] (Fig. 3-3a), magnetic actuation is used to deflect the actuation membrane upward, causing the mirror membrane with 5 mm of diameter to deflect in convex direction. When actuation is removed, the mirror membrane returns to its original shape, which can be convex, flat or concave, depending on the initial pressure of

the air chamber. Using a current of 0.8 A, the mirror can achieve an OPR of 20 m^{-1}, which corresponds to a stroke variation of 31.25 µm.

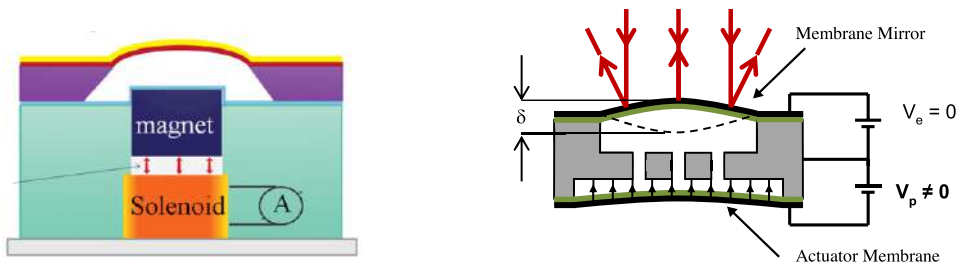

(a) (b)

Figure 3-3: Examples of varifocal mirrors with pneumatic actuation. (Sources: (a) [52], (b) [53])

In [53] (Fig. 3-3b), electrostatic and pneumatic actuation are combined to increase the stroke of the mirror. Both the mirror and the actuation membrane are deflected with electrostatic actuation. Actuating the mirror membrane causes it to deflect in concave direction, while actuating the other membrane results in convex deflection of the mirror due to the pressure applied to the air chamber. Using this actuation mechanism, the total stroke of the mirror membrane was 21 µm.

Hydraulic actuation has the potential to generate larger deflection than pneumatic due to the incompressibility of the fluid, however, until now, no MEMS varifocal mirror has been proposed with this actuation mechanism. This may be related to the difficulty of filling and sealing the fluidic chamber. Fig 3-4 shows two varifocal mirrors that are not MEMS devices, but use hydraulic actuation. The first one (Fig. 3-4a) is a 60 mm mirror that uses a piezoelectric piston to apply pressure to the fluidic chamber [10]. It was designed for material processing applications, being able to withstand a laser beam with 2 kW. Due to its large diameter and a membrane thickness of 1.5 mm, the obtained OPR was only 0.08 m^{-1}.

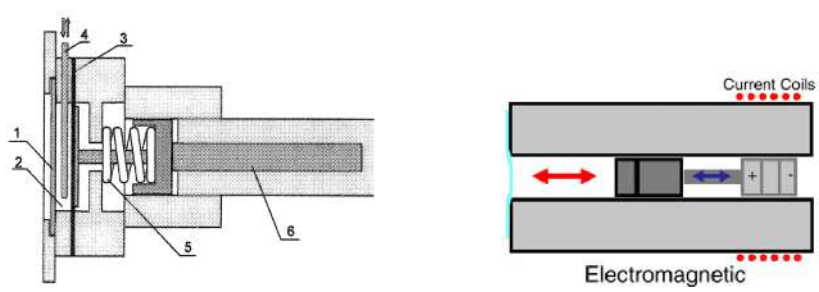

(a) (b)

Figure 3-4: Examples of varifocal mirrors with hydraulic actuation. (Sources: (a) [10], (b) [54])

Table 3.2: Comparison of varifocal mirrors with pneumatic or hydraulic actuation

Reference	**Year**	**Diameter**	**OPR (m^{-1})**	**Primary Actuator**	**Operating Conditions**	**Max Freq**
Pneumatic						
Hossain *et al.* [52]	2015	5 mm	20	Magnetic	0.8 A, 2 W	-
Moghimi *et al.* [53]	2015	4 mm	21	Electrostatic	300 V	2 kHz
Hydraulic						
Rabczuk *et al.* [10]	2004	60 mm	0.08	Piezoelectric	90 kPa	-
Alzaydi *et al.* [54]	2008	950 μm	286	Magnetic	22.5 kPa	15 Hz

The second one (Fig. 3-4b) is a proof-of-concept device made from a 0.5 µm-thick polyester sheet clamped by a metallic holder [54]. The interface between the sheet and the fluidic chamber is a 1 mm hole in the holder and the fluid is displaced using magnetic actuation. By applying 22.5 kPa to the fluidic chamber, the mirror was able to deflect 71.5 µm, resulting in an OPR of 286 m^{-1}. The main drawback of this actuation mechanism was that the maximum operating frequency was limited to 15 Hz. Table 3.2 summarizes the characteristics and performance of these four mirrors with pneumatic and hydraulic actuation.

3.3 Bimorph Mirrors

Bimorph mirrors are made from active membranes composed of two or more layers of different materials, whose expansion and contraction can be controlled. Instead of deflecting due to an applied pressure, the curvature of these mirrors is directly controlled by expansion of one material of the membrane in respect to the other. The expansion and contraction of the membrane materials can be controlled by thermal dilation or by the piezoelectric effect.

3.3.1 Electrothermal Mirrors

Electrothermal mirrors are made of membranes with two layers of materials with different coefficients of thermal expansion. When an electrical current passes through the mirror, its temperature increases, causing its two layers to expand in different proportions, changing the curvature of the mirror κ. This operating principle is illustrated in Fig. 3-5.

The deflection of the mirror can be determined by the temperature variation ΔT it undergoes. For example, for a mirror made from polysilicon and gold [55], its

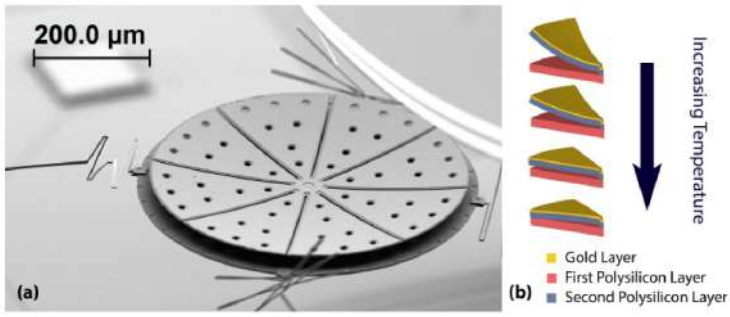

Figure 3-5: Operating principle of varifocal mirrors with electrothermal actuation. (Source: (a) [55])

curvature is given by:

$$\kappa(\Delta T) = \frac{1}{r(\Delta T)} = \frac{1}{r_0} + \frac{6\,(h_{Au}+h_{Si})\,(\alpha_{Au}-\alpha_{Si})\,\triangle T}{4h_{Au}^2+4h_{Si}^2+6h_{Au}h_{Si}+\left(\frac{E_{Au}h_{Au}^3}{E_{Au}h_{Si}}\right)+\left(\frac{E_{Au}h_{Si}^3}{E_{Au}h_{Au}}\right)}, \tag{3.4}$$

where r_0 is the initial radius of curvature of the mirror, ΔT is the temperature variation, h_{Au} and h_{Si} are the thickness of the gold and the polysilicon layer respectively, α_{Au} and α_{Si} are the coefficients of thermal expansion of each layer and E_{Au} and E_{Si} are the Young's modulus of each layer. Since the temperature of the mirror is increased due to Joule heating, the temperature variation is proportional to the dissipated electrical power

$$\Delta T \propto I^2 R(T), \tag{3.5}$$

where I is the electrical current used to heat the mirror and $R(T)$ is the resistance of the mirror at the temperature T.

One of the main advantages of electrothermal mirrors is that they can achieve very large curvatures, with focal lengths as low as -0.48 mm [55]. Such short focal length is usually not achieved by any type of membrane mirror. Their actuation speed is not so slow – considering that deflecting the membrane requires heating the entire mirror – as some electrothermal mirrors can reach operating frequencies of 120 Hz [56]. However their diameter is typically bellow 1 mm, as electrothermal mirrors with large diameter would be impractical, since the energy required to heat the mirror increases with the mass of the membrane. Table 3.3 presents the characteristics and performances of the most relevant electrothermal mirrors reported in the literature.

Table 3.3: Comparison of varifocal mirrors with electrothermal actuation

Reference	**Year**	**Diameter**	**OPR (m^{-1})**	**Operating Conditions**	**Max Freq**
Burns *et al.* [56]	1998	1 mm	66	480 mW	120 Hz
Liu *et al.* [57]	2003	100 μm	556	22 °C to 72 °C	-
Hou *et al.* [58]	2003	200 μm	45	0 °C to 100 °C	-
Li *et al.* [59]	2013	1 mm	28	10 °C to 100 °C	8 Hz
Paterson *et al.* [60]	2015	1 mm	39	10 °C to 100 °C	-
Morisson *et al.* [55]	2015	400 μm	2132	27 mW	83 Hz

3.3.2 Piezoelectric Mirrors

Piezoelectric mirrors are made of thin reflective mirrors attached to layers of piezoelectric material. When voltage is applied to the piezoelectric material, it expands in respect to the reflective layer, causing the mirror to bend. If two piezoelectric layers are used – separated by a dielectric layer – one layer can be expanded while the other is contracted, increasing the bending effect even further. Fig. 3-6 shows two examples of piezoelectric mirrors.

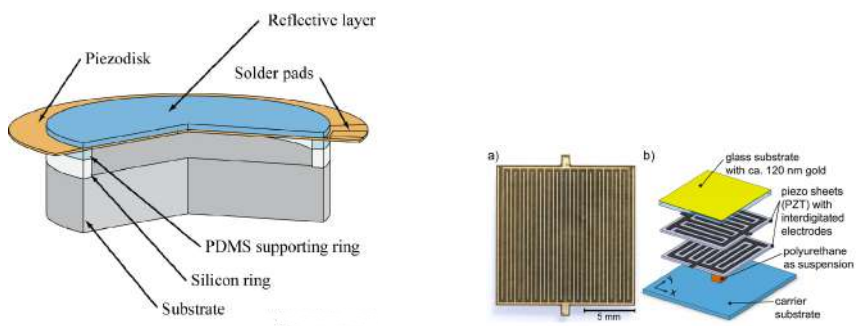

(a) (b)

Figure 3-6: Examples of varifocal mirrors with piezoelectric actuation. (Sources: (a) [12], (b) [61])

In [12] (Fig. 3-6a) a 120 µm thick piezodisk was glued to a 300 µm-thick silicon mirror coated with a silver layer. The backside of the piezodisk was structured with radial electrodes, allowing a radial voltage profile to be applied to the disk, controlling its expansion. By adjusting the voltage profile, it was possible to deflect the mirror in a conical shape, creating an adaptive axicon mirror. On the other hand, in [61] (Fig. 3-6b) two orthogonal layers of PZT were used to control the curvature of the mirror in the X and Y directions. By adjusting the expansion of these two layers, not only the focal length of the mirror, but also its eccentricity could be controlled.

The main advantage of piezoelectric mirrors is their excellent optical quality,

Table 3.4: Comparison of varifocal mirrors with piezoelectric actuation

Reference	**Year**	**Diameter**	**OPR (m^{-1})**	**Operating Conditions**	**Resonant Freq**
Mescher *et al.* [62]	2002	300 μm	46	700 V	low MHz
Brunne *et al.* [12]	2011	15 mm	0.23	60 V	9.9 kHz
Sturmer *et al.* [61]	2013	14 x 14 mm	0.08	120 V	-
Janin *et al.* [63]	2018	1.4 mm	1.10	30 V	26.1 kHz

since they induce less aberrations than any other type of varifocal mirrors, resulting in almost diffraction limit focusing [12]. However, the stroke they can provide is very limited, usually around 1 µm. This means they can only achieve large OPR with diameters of a few hundred microns [62].

Another way to achieve large OPR with piezoelectric mirrors is to operate them in their resonance frequency, which is usually in the kHz range. In [63], the proposed piezoelectric mirror has an OPR of only 1.1 m^{-1} in static deflection, but can reach 26 m^{-1} if operated in resonance at 26.1 kHz. When operated in its fourth resonant mode, at 107 kHz, it can reach 74 m^{-1}. Table 3.4 presents the characteristics and performances of some piezoelectric mirrors reported in the literature. Indicated OPR values correspond to static deflection, not resonant operation.

3.4 Comparison between Varifocal Mirrors

Even though MEMS varifocal mirrors are still an active area of research, there has been considerable development on membrane mirrors for imaging applications. Over the last 20 years, the design and fabrication methods for electrostatic mirrors have been significantly improved, allowing these mirrors to be integrated in optical microscopes [47], confocal microscopy systems [11, 50] and OCT systems [41]. Some of these mirrors are already reaching the market as components for microscopy systems (Agile Focus Designs, USA).

On the other hand, bimorph mirrors have been showing better potential for different applications. Electrothermal mirrors are being proposed for usage in optical switches and optical wireless communication systems [55], while piezoelectric mirrors would be useful in high-precision applications such as nanomachining or optical tweezers [12]. It is clear, however, that none of these actuation mechanisms is suitable for focusing high-power lasers. Electrothermal mirrors have small diameter, which increases the laser induced damage over the mirror, as the high power of the laser beam has to be concentrated in a small area. Besides that, since their actuation is based on the temperature of the mirror, the heating induced by the high-power laser would probably disrupt the mirror control. Piezoelectric mirrors, on the other hand, are only able to provide large optical power range when operated in resonance. This is not acceptable, since tissue ablation requires keeping the beam

focused at an specific point.

Electrostatic mirrors could theoretically be used with high-power laser, however a large diameter would be needed to avoid laser induced damage. Since electrostatic stroke is limited, large aperture electrostatic mirrors exhibit optical power ranges lower than 20 m^{-1}, which is insufficient for beam focusing in endoscopic laser surgery. To achieve larger stroke, the actuation voltage would need to be increased further than 400 V. Furthermore, as the stroke increases, the air gap must also increase to avoid snapdown, which makes necessary to increase the voltage even further. Considering that, the design of a large aperture electrostatic mirror with large optical power range seems impractical.

Pneumatic and hydraulic actuation can produce larger stroke than electrostatic, assuming a sufficiently strong primary actuator is selected. This allows achieving large OPR even for large aperture mirrors. Furthermore, hydraulic actuation can potentially help cooling the mirror, decreasing its thermal sensitivity even further. The main drawback of hydraulic actuation compared to electrostatic is the operating frequency, which drops from the kHz range to the order of 10 Hz. However tissue ablation does not require such a high operating frequency, since the motion of the laser spot is not so fast. Based on these considerations, hydraulic actuation seems to be the most suitable actuation mechanism for beam focusing in endoscopic laser surgery.

4
Modeling and Simulation

In this chapter, we present the mathematical models used to describe the deflection of a membrane mirror and the focusing of a laser beam in an optical setup containing such type of mirror. First, we present the mechanical models used to determine the deflection of a membrane mirror, including the thermal effects caused by the high-power laser irradiation. Then, we analyze how the surface of a deflected mirror focus a collimated laser beam. After that, we present a new model for the laser focusing task from a control problem perspective. Finally, we combine these three models to present a feed-forward controller to actuate the varifocal mirror in open loop and analyze the impact of the mirror's design parameters on its performance.

4.1 Membrane Deflection Model

The problem of modeling the deflection of a freestanding membrane consists on determining how the membrane surface deforms as a function of its mechanical properties and the applied load. The solution to this problem for small deflections is given by the Kirchhoff-Love's plate theory [64], according to which the membrane deflection is determined by the bending moments acting at the membrane boundary. However, when the deflection is much larger than the membrane thickness, the elastic stress generated by the straining of its neutral fiber becomes significant, adding non-linearities to the model [65]. In this case, the solution depends largely on the boundary conditions and the load profile, and analytical solutions can only be obtained by approximations, thus resulting in a variety of proposed models [66].

In this project, we are interested in obtaining an analytical model for the deflection of circular and elliptical membranes in the large-deflections regime, under

uniform pressure (the hydraulic actuation) and thermal load (generated by the high-power laser irradiation). We achieve that by combining different models proposed in the literature, as presented in the following sections. In Section 4.1.1, we review the formulation of the deflection model for circular membranes under uniform pressure, presented by Schomburg [14]. In Section 4.1.2, we extend this model for the case of elliptical membranes. Then in Sections 4.1.3 and 4.1.4, we incorporate the thermal effects of the laser irradiation in the membrane deflection. Finally, in Section 4.1.5 we combine the obtained results presenting the explicit equations for the membrane deflection and analyzing the conditions that lead to membrane rupture.

4.1.1 Deflection Model for Circular Membranes

When uniform pressure difference Δp is applied to a thin circular membrane, the membrane deflects in the direction of the applied pressure, as illustrated in Fig. 4-1. Assuming the membrane deflection to be much larger than its thickness, the bending moments at the membrane rim can be neglected and the membrane deflection becomes parabolic. Therefore the shape of the deflected membrane is given by

$$w(r) = w_0 \left(1 - \left(\frac{r}{R}\right)^2\right), \tag{4.1}$$

where R is the radius of the membrane and w_0 is its central deflection.

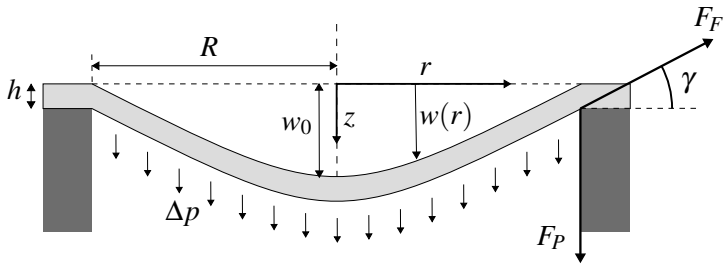

Figure 4-1: Deflection of a thin circular membrane under uniform pressure difference.

The central deflection of the membrane can be calculated based on the force equilibrium at the rim. When the membrane is in equilibrium, the balance of forces in the Z direction implies on

$$F_P = -F_F sin(\gamma), \tag{4.2}$$

where F_P is the deflection force caused by the pressure difference Δp and F_F is the clamping force of the membrane under elastic stress in the radial direction. The term F_P can be calculated simply as

$$F_P = \Delta p \pi R^2, \tag{4.3}$$

while F_F is given by

$$F_F = \sigma h 2\pi R, \tag{4.4}$$

in which σ is the total stress on the membrane and $h2\pi R$ is the membrane thickness times its perimeter. For small angles γ, the sine is approximately equal to the tangent, which is the slope of the parabola. In this case, the following approximation can be used:

$$sin(\gamma) \approx tan(\gamma) = \frac{\partial w}{\partial r}\bigg|_{r=R} = \frac{-2w_0}{R}. \tag{4.5}$$

Replacing 4.3, 4.4 and 4.5 into the 4.2, we obtain

$$\Delta p = \frac{4w_0 h}{R^2}\sigma. \tag{4.6}$$

The stress σ on the membrane is composed by the residual stress σ_0 – which exists even when the membrane is not deflected – and the elastic stress in the radial direction σ_r due to the straining of the membrane's neutral fiber. The later one can be calculate with the Hooke's law

$$\varepsilon_r = \frac{1}{E}\left(\sigma_r - \nu\sigma_\theta\right) \tag{4.7a}$$

$$\varepsilon_\theta = \frac{1}{E}\left(\sigma_\theta - \nu\sigma_r\right), \tag{4.7b}$$

where ε_r and ε_θ are the strains in the radial and tangential directions, respectively, σ_θ is the tangential stress and E and ν are the Young's modulus and Poisson's ratio of the membrane material.

The radial strain ε_r can be obtained by the formula of the arc length of the parabola. For a parabola with width $2R$ and height w_0, as illustrated in Fig. 4-2, its arc length is given by

$$L_{Pa} \approx 2R\left(1 + \frac{2}{3}\frac{w_0^2}{R^2} - \frac{2}{5}\frac{w_0^4}{R^4}\right), \tag{4.8}$$

which means the radial strain ε_r can be expressed as

$$\varepsilon_r \approx \frac{2}{3}\frac{w_0^2}{R^2}. \tag{4.9}$$

Since the tangential strain of the membrane is currently unknown, the equation 4.7 cannot be fully solved. However, this can be obtained if we make an assumption over the tangential strain. One assumption commonly made is that the radial and tangential strains are equal everywhere in the membrane, as this is true at least for

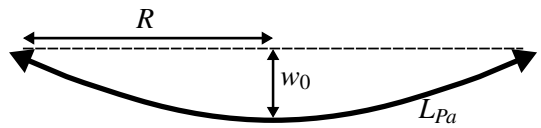

Figure 4-2: Arc length L_{Pa} of a parabola with height w_0 and width $2R$.

the central point. Assuming $\varepsilon_\theta = \varepsilon_r$, the solution to the 4.7 becomes

$$\sigma_r = \frac{E}{1-\nu}\varepsilon_r. \tag{4.10}$$

Replacing 4.9 into 4.10, we are able to calculate the total stress σ as a sum of the residual stress σ_0 and the elastic stress σ_r:

$$\sigma = \sigma_0 + \frac{2}{3}\frac{w_0^2}{R^2}\frac{E}{1-\nu}. \tag{4.11}$$

Replacing 4.11 into 4.6 gives us the full expression that relates the membrane central deflection to the applied pressure:

$$\Delta p = \frac{4w_0 h}{R^2}\left(\sigma_0 + \frac{2}{3}\frac{w_0^2}{R^2}\frac{E}{1-\nu}\right). \tag{4.12}$$

This is known as the *Cabrera's equation* and is often used to model membrane deflections [67]. Since we assumed $\varepsilon_\theta = \varepsilon_r$, which is not necessarily true for the entire membrane, equation 4.12 is only an approximate solution. However the exact solution for this problem was found using finite element methods [15] and corresponds to

$$\Delta p = \frac{4w_0 h}{R^2}\left(\sigma_0 + \frac{2}{3}\frac{w_0^2}{R^2}\frac{E}{1.026 - 0.793\nu - 0.233\nu^2}\right). \tag{4.13}$$

For materials with low Poisson's ratio ($\nu < 0.3$), the difference between the 4.12 and the 4.13 is lower than 10% [14]. For this reason, equation 4.12 is sometimes preferred for convenience. From this point forward, this expression will be written as

$$\Delta p = \frac{4w_0 h}{R^2}\left(\sigma_0 + \frac{2}{3}\frac{w_0^2}{R^2}E_\nu\right), \tag{4.14}$$

where E_ν can be used to represent the exact FEM solution or *Cabrera's* approximation interchangeably.

4.1.2 Deflection Model for Elliptical Membranes

When the boundary of the membrane is elliptical instead of circular, the membrane deflection becomes an elliptical paraboloid [43], described by

$$w(x,y) = w_0 \left(1 - \left(\frac{x^2}{R_x^2} + \frac{y^2}{R_y^2}\right)\right), \tag{4.15}$$

with R_x and R_y being the half-axes of the ellipse in the x and y direction, respectively. This surface has the property that both its tangential section ($y = 0$ plane) and its sagittal section ($x = 0$ plane) are parabolas. Therefore, we may define the proportionality factor $K_{x/y}$ of the paraboloid as the ratio between its tangential and sagittal curvatures:

$$K_{x/y} = \frac{\frac{-w_0}{R_x^2}}{\frac{-w_0}{R_y^2}} = \frac{R_y^2}{R_x^2}. \tag{4.16}$$

If we define α as the aspect ratio of the ellipse, such that $R_x = \alpha R_y$, than $K_{x/y}$ becomes

$$K_{x/y} = \frac{1}{\alpha^2}. \tag{4.17}$$

The expression for the central deflection w_0 is given in [43] as

$$w_0 = \frac{\Delta p R_x^2 R_y^2}{2h\sigma_0 \left(R_x^2 + R_y^2\right)}. \tag{4.18}$$

If we isolate Δp and replace R_x with αR_y, the 4.18 becomes

$$\Delta p = \frac{4 w_0 h \sigma_0}{k_\alpha R_y^2}, \tag{4.19}$$

with the term k_α defined as:

$$k_\alpha = \frac{2\alpha^2}{(1+\alpha^2)}. \tag{4.20}$$

It is worth noting that for circular membranes $k_\alpha = 1$, in which case the 4.19 becomes equivalent to the 4.14, if the cubic term is ignored. This approximation is valid only for small deflections, since the cubic term is negligible when w_0 is small. However for large deflections, the entire expression must be considered. Therefore, we can obtain the full solution for the deflection of the elliptical membrane by

generalizing the 4.14, replacing R^2 with $k_\alpha R_y^2$:

$$\Delta p = \frac{4w_0 h}{k_\alpha R_y^2}\left(\sigma_0 + \frac{2}{3}\frac{w_0^2}{k_\alpha R_y^2}E_\nu\right). \tag{4.21}$$

4.1.3 Thermal Deflection Model

Besides the applied pressure, the shape of the membrane can also be deformed by a thermal load. More specifically, if the membrane undergoes an uniform temperature variation ΔT, the membrane shape remains parabolic, but the thermal expansion of the membrane changes its central deflection. This effect can be modeled by using the Hooke's law with thermal strain, instead of the 4.7:

$$\varepsilon_r = \frac{1}{E}\left(\sigma_r - \nu\sigma_\theta\right) + \alpha_m \Delta T \tag{4.22a}$$

$$\varepsilon_\theta = \frac{1}{E}\left(\sigma_\theta - \nu\sigma_r\right) + \alpha_m \Delta T \tag{4.22b}$$

The difference between the 4.22 and the 4.7 is that the thermal strain $\alpha_m \Delta T$ (in which α_m is the coefficient of thermal expansion of the membrane material) is added to ε_r and ε_θ. This assumes the membrane material is isotropic, which means that the thermal strain is the same in both the radial and tangential directions. Once again, assuming $\varepsilon_r = \varepsilon_\theta$ throughout the membrane, the radial stress becomes

$$\sigma_r = \frac{E}{1-\nu}\left(\varepsilon_r - \alpha_m \Delta T\right) \tag{4.23}$$

Replacing 4.23 and 4.9 into 4.6, we obtain

$$\Delta p = \frac{4w_0 h}{R^2}\left(\sigma_0 + \frac{2}{3}\frac{w_0^2}{R^2}\frac{E}{1-\nu} - \frac{E\alpha_m \Delta T}{1-\nu}\right), \tag{4.24}$$

which can be simplified as

$$\Delta p = \frac{4w_0 h}{R^2}\left(\left(\sigma_0 - \sigma_T\right) + \frac{2}{3}\frac{w_0^2}{R^2}E_\nu\right), \tag{4.25}$$

in which

$$\sigma_T = \alpha_m E_\nu \Delta T \tag{4.26}$$

is defined as the thermal stress. Generalizing this result for elliptical membranes

as well, we obtain:

$$\Delta p = \frac{4w_0 h}{k_\alpha R_y^2}\left((\sigma_0 - \sigma_T) + \frac{2}{3}\frac{w_0^2}{k_\alpha R_y^2}E_\nu\right), \tag{4.27}$$

As it can be seen, the effect of a temperature increase alleviates the residual stress of the membrane, decreasing the pressure necessary to deflect it, thus increasing the membrane deflection. Moreover, depending on the magnitude of ΔT, it may cause the stress of the membrane to switch from tensile to compressive.

When the membrane is under compressive stress, i.e. $(\sigma_0 - \sigma_T) < 0$, the expression for Δp is no longer monotonic. This means that there is a pressure range for which the membrane may buckle in any direction, as illustrated in Fig. 4-3. A membrane in this configuration is called a bistable membrane. This condition is usually undesirable since the shape of the membrane cannot be properly controlled. To avoid that, it is possible to calculate the maximum temperature variation ΔT_{max} the membrane can undergo without entering the bistable regime as

$$\Delta T_{max} = \frac{\sigma_0}{\alpha_m E_\nu}. \tag{4.28}$$

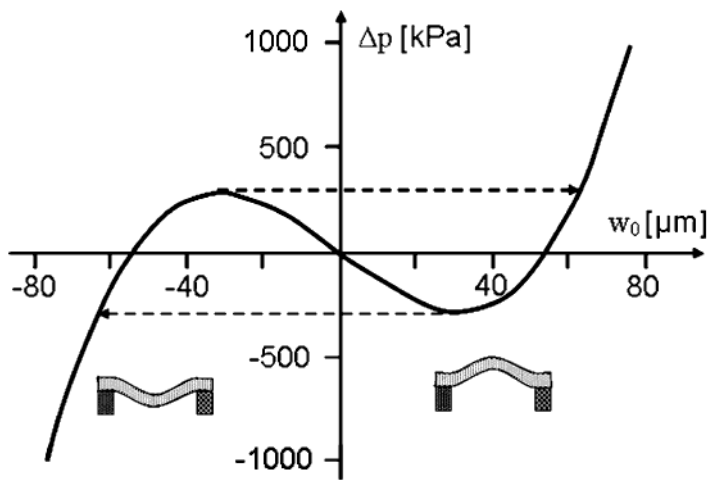

Figure 4-3: Relationship between the applied pressure difference and the central deflection of a circular membrane under compressive residual stress. (Source: [14])

4.1.4 Membrane Heating under Laser Irradiation

When the membrane is heated by laser irradiation, its temperature variation may not be uniform, especially if the intensity profile of the laser beam is Gaussian. The resulting temperature gradient in the membrane may distort its deflected shape,

causing it to deviate from the elliptical paraboloid. The solution to the deflected membrane shape in this condition becomes complex and cannot be obtained analytically. However, the expression 4.27 can still be used to calculate the central deflection of the membrane, as long as ΔT is assumed to be an average value of the temperature variation. In this case, the deformation in the membrane shape caused by the difference between ΔT and the real temperature gradient will induce optical aberrations in the mirror. The magnitude of such aberrations depend on the range of temperatures present in the membrane.

To investigate the expected temperature variation of the membrane under laser irradiation, as a function of the properties of the laser and the mirror, we performed FEM thermal simulation using ANSYS. In this simulation, a 3W laser beam was used to heat the mirror and the only cooling mechanisms considered were irradiation and convection to stagnant air. The reflectivity of the mirror was assumed to be 98%.

Figure 4-4 shows the temperature gradient obtained in the mirror for laser beams of 1 mm and 4 mm of diameter. As it can be seen, the larger laser beam results in lower temperature variation, since the energy of the laser is less concentrated. This type of simulation allows us to determine the maximum temperature variation in the mirror as a function of the diameter of the laser beam, which allows us to design the aperture of the mirror to be sufficiently large in order to prevent the temperature variation from reaching ΔT_{max} .

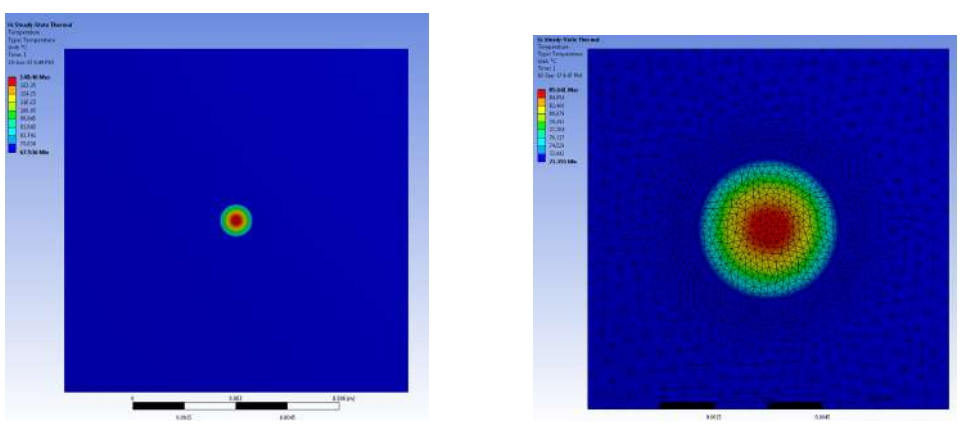

(a) (b)

Figure 4-4: Steady state solution of the FEM thermal simulation of the membrane under irradiation of a 3W continuous wave laser beam with diameter of (a) 1 mm and (b) 4 mm. The temperature range of the images are $\{67.536, 140.46\}$°C for the 1 mm beam and $\{71.355, 85.641\}$°C for the 4 mm beam.

4.1.5 Explicit Model for the Membrane Central Deflection

The Equation 4.27 represents the full solution of the membrane deflection model, as it allows us to calculate the pressure difference Δp associated with each central deflection of the membrane. However, in some cases it may be necessary to calculate w_0 explicitly. This can be obtained by *Cardan's* formula. Rewriting the 4.27 in the form of a depressed cubic equation, we obtain:

$$w_0^3 + w_0 \left(\frac{3k_\alpha R_y^2 (\sigma_0 - \sigma_T)}{2E_\nu} \right) - \left(\frac{3k_\alpha^2 R_y^4 \Delta p}{8hE_\nu} \right) = 0 \tag{4.29}$$

The solution to this equation given by *Cardan's formula* is:

$$w_0 = \sqrt[3]{\eta + \sqrt{\eta^2 + \xi^3}} + \sqrt[3]{\eta - \sqrt{\eta^2 + \xi^3}} \tag{4.30a}$$

$$\eta = \frac{3k_\alpha^2 R_y^4 \Delta p}{16hE_\nu} \tag{4.30b}$$

$$\xi = \frac{k_\alpha R_y^2 (\sigma_0 - \sigma_T)}{2E_\nu} \tag{4.30c}$$

As it can be seen, as long as the membrane is under tensile stress (i.e. $\sigma_0 - \sigma_T > 0$) the 4.30 always provides a single real solution for w_0, which means that the expression 4.27 is monotonic.

Membrane Rupture

Using the presented model, it is also possible to determine the maximum deflection the membrane can achieve before rupturing. Assuming the membrane is uniform, rupture occurs when the total stress on the membrane σ reaches the yield stress of the membrane material σ_y. This corresponds to

$$\sigma_y = \sigma_0 - \sigma_T + \frac{2}{3} \frac{w_{0y}^2}{k_\alpha R_y^2} E_\nu, \tag{4.31}$$

where w_{0y} is the central deflection of the membrane that leads to rupture. Isolating w_{0y} in 4.31, we obtain

$$w_{0y} = R_y \sqrt{\frac{3k_\alpha}{2} \frac{(\sigma_y + \sigma_T - \sigma_0)}{E_\nu}}. \tag{4.32}$$

The corresponding rupture pressure is obtained as

$$\Delta p_y = \frac{4w_{0y}h}{k_\alpha R_y^2}\sigma_y. \tag{4.33}$$

Finally replacing 4.32 into 4.33, we can calculate the maximum pressure that can be applied to the membrane before rupture occurs as

$$\Delta p_y = 4\sigma_y \frac{h}{R_y}\sqrt{\frac{3}{2k_\alpha}\frac{(\sigma_y+\sigma_T-\sigma_0)}{E_\nu}}. \tag{4.34}$$

4.2 Laser Focusing with a Varifocal Mirror

Since the deflection of an elliptical membrane assumes the shape of an elliptical paraboloid, the varifocal membrane mirror behaves as a parabolic mirror. The main property of such type of mirror is that all light rays parallel to its axis are reflected to the mirror's focal point, regardless of the curvature of the paraboloid or the diameter of the beam. This is especially useful for laser focusing, as it allows focusing a collimated beam without inducing any optical aberration. However, the main problem with a parabolic mirror is that its focal point lies in the optical path of the laser beam, therefore it is not possible to access the focal point without blocking the collimated beam.

There are two main methods to avoid this problem. The first one is to use the mirror in a telescopic configuration. The second one is to use the mirror in an off-axis configuration, such that it behaves as an off-axis parabolic mirror. The following sections analyze the advantages and drawbacks of these two approaches.

4.2.1 On-Axis Telescopic System

One example of telescopic focusing system is the optical system composed of two mirrors illustrated in Fig. 4-5. In this system, the collimated beam passes through a hole in the primary mirror and is reflected by the secondary mirror, which is a convex parabolic mirror. Then the divergent beam is focused by the primary mirror at a point behind the secondary mirror. This focusing system is used in many surgical laser systems, in which case the focal length of the beam is adjusted by changing the distance between the two mirrors. To achieve variable focal length without the need of displacing the mirrors, we could replace the secondary mirror with a varifocal membrane mirror.

The main issue with this approach is that the ratio between the diameters of the primary and the secondary mirrors must be large, otherwise a significant part of the collimated beam is reflected back through the hole of the primary mirror. This means that, in order to keep the focusing system compact, the varifocal mirror

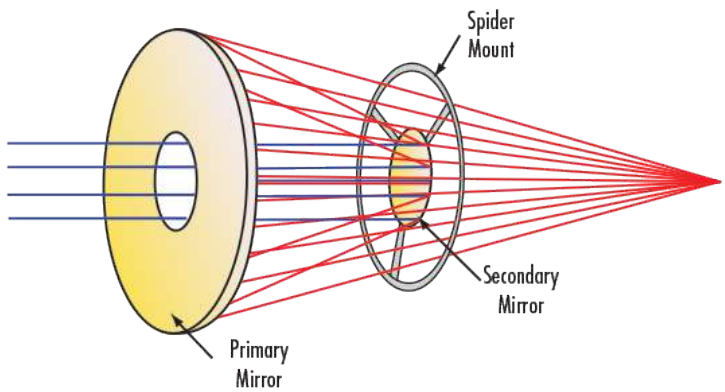

Figure 4-5: Telescopic focusing system with two mirrors.

would have to be very small (less than 1 mm), resulting in high power density of the laser over the mirror. This would result in a large temperature variation of the membrane, preventing proper control of the deflection of the mirror. Therefore this focusing approach is not suitable for a MEMS varifocal mirror.

4.2.2 Off-Axis Parabolic Mirrors

In order to focus the collimated laser beam outside the optical path of the beam, an off-axis parabolic mirror can be used. An off-axis parabolic mirror is a curved surface which corresponds to a lateral segment of a larger paraboloid. To illustrate that, let's consider the collimated beam in Fig. 4-6 that is parallel to the axis of a paraboloid and intercepts it at the point $P_0 = (x_0, 0, z_0)$. Since the focal point of the paraboloid lies in the Z-axis, the collimated beam is reflected with an angle of 2θ while being perfectly focused.

The equation that describes the paraboloid is

$$z = a\left(x^2 + y^2\right) \tag{4.35}$$

and the coordinates of its focal point are $f = (0, 0, 1/4a)$. This means that the relationship between the angle of incidence θ and the position of the beam is given by:

$$tan(2\theta) = \frac{x_0}{\frac{1}{4a} - z_0}. \tag{4.36}$$

Replacing $z_0 = ax_0^2$ and solving the 4.36 for x_0 we obtain:

$$x_0 = \frac{tan(\theta)}{2a}. \tag{4.37}$$

This result is demonstrated in the Appendix A.

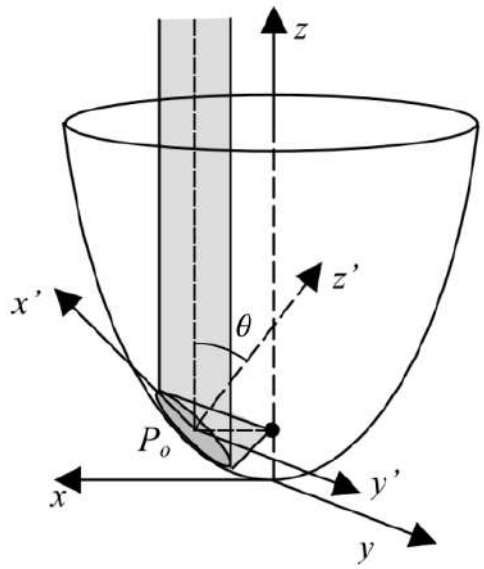

Figure 4-6: Paraboloid with incident collimated beam parallel to its axis. (Source: [43])

We can then define a new coordinate system (x', y', z') centered at the off-axis paraboloid, by translating the original coordinate system in $(x_0, 0, z_0)$ and rotating it in θ around the Y-axis. The transformation between these coordinates systems is given by the following equations:

$$x' = (x - x_0)c_\theta + (z - z_0)s_\theta \tag{4.38a}$$
$$y' = y \tag{4.38b}$$
$$z' = -(x - x_0)s_\theta + (z - z_0)c_\theta \tag{4.38c}$$

For compactness, the following notation is being used: $cos(\alpha) = c_\alpha$, $sin(\alpha) = s_\alpha$ and $tan(\alpha) = t_\alpha$. The inverse transformation is given by:

$$x = x_0 + x'c_\theta - z's_\theta \tag{4.39a}$$
$$y = y' \tag{4.39b}$$
$$z = z_0 + x's_\theta + z'c_\theta \tag{4.39c}$$

If we replace the 4.39 into the 4.35, we obtain the shape of the off-axis paraboloid

in the transformed coordinate system as:

$$ax_0^2 + x's_\theta + z'c_\theta = ay'^2 + a(x_0^2 + x'^2c_\theta^2 + z'^2s_\theta^2 + 2x_0x'c_\theta - 2x_0z's_\theta - 2x'z'c_\theta s_\theta) \tag{4.40}$$

Simplifying this expression and replacing $2ax_0 = t_\theta$, we obtain:

$$az'^2s_\theta^2c_\theta + ay'^2c_\theta + ax'^2c_\theta^3 - z' - 2ax'z'c_\theta^2s_\theta = 0 \tag{4.41}$$

Since the term z'^2 is several orders of magnitude smaller than the others, it can be omitted from the equations without inducing significant error. This reduces 4.41 to:

$$ay'^2c_\theta + ax'^2c_\theta^3 - z' - 2ax'z'c_\theta^2s_\theta = 0 \tag{4.42}$$

If we analyze the tangential ($y' = 0$) and the sagittal ($x' = 0$) sections of this surface, we obtain:

$$\text{Tangential section} \qquad z'\left(2ax'c_\theta^2s_\theta + 1\right) = ax'^2c_\theta^3, \tag{4.43a}$$

$$\text{Sagittal section} \qquad z' = ay'^2c_\theta, \tag{4.43b}$$

As it can be seen, the sagittal section is a parabola, but the tangential section is not. In fact, the tangential section is not even symmetric in respect to x', as it is illustrated in Fig. 4-7. To better compare the shape of the tangential section to the deflection of the membrane mirror, we can approximate 4.43a by its Taylor series up to the fourth order. This expansion is also demonstrated in the Appendix A and gives us the following expression:

$$z' \cong ac_\theta^3x'^2 - 2a^2c_\theta^5s_\theta x'^3 + 4a^3c_\theta^7s_\theta^2x'^4, \tag{4.44}$$

The difference between the obtained expression and a parabola are the terms with x'^3 and x'^4. Therefore, if we consider these two terms as an approximation error, the surface of the off-axis paraboloid can be approximated by an elliptical paraboloid. If we calculate the proportionality factor $K_{x/y}$ of this surface, we obtain

$$K_{x/y} = \frac{acos(\theta)^3}{acos(\theta)} = cos(\theta)^2 \tag{4.45}$$

Comparing the 4.45 with the 4.17, we can see that the shape of the off-axis paraboloid can be approximated by an elliptical paraboloid with aspect ratio

$$\alpha = \frac{1}{cos\theta}. \tag{4.46}$$

The central deflection w_0 of the elliptical paraboloid can be calculated by com-

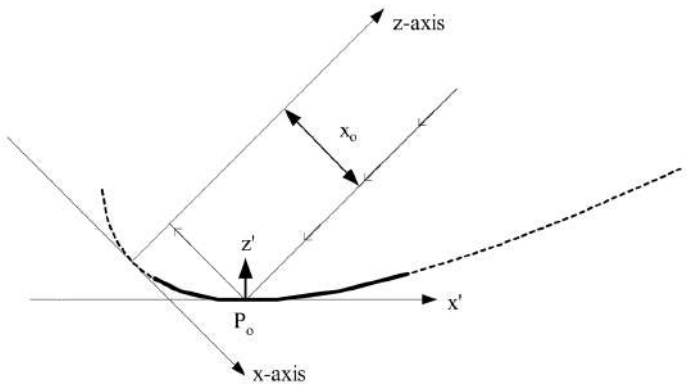

Figure 4-7: Tangential cross section of the paraboloid centered at the transposed coordinate system. (Source: [43])

paring the curvature of the sagittal sections given by the equations 4.15 and 4.43b.

$$\frac{w_0}{R_y^2} = acos(\theta) \rightarrow a = \frac{w_0}{R_y^2 cos(\theta)} \tag{4.47}$$

The same result is obtained if we compare the tangential curvatures instead, given by equations 4.15 and 4.44. Finally, we are able to calculate the effective focal length of the mirror as

$$f_M = \frac{x_0}{sin(2\theta)} = \frac{tan(\theta)}{2asin(2\theta)} \tag{4.48}$$

Replacing 4.47 into 4.48 gives:

$$f_M = \frac{R_y^2}{2w_0}\frac{cos(\theta)tan(\theta)}{sin(2\theta)} = \frac{R_y^2}{2w_0}\frac{sin(\theta)}{sin(2\theta)} \tag{4.49}$$

Simplifying this expression we obtain:

$$f_M = \frac{R_y^2}{4w_0 cos(\theta)} \tag{4.50}$$

Finally, by replacing $cos(\theta) = 1/\alpha$, we obtain

$$f_M = \frac{\alpha R_y^2}{4w_0} \tag{4.51}$$

4.2.3 Validity of the Approximation of the Off-Axis Paraboloid as an Elliptical Paraboloid

The approximation used for the tangential section of the off-axis paraboloid as a parabola can induce optical aberrations in the focused beam. These aberrations can be calculated as the deviation between the the elliptical paraboloid and the off-axis paraboloid, given by equations 4.15 and 4.42 respectively, for any given value of focal length of the mirror. In [43], it has been demonstrated that for focal lengths longer than 10 mm the peak-to-peak value of these aberrations is lower than 0.06 µm, which is negligible. Therefore the elliptical varifocal mirror can be considered a good approximation for an off-axis paraboloid.

4.3 Laser Focusing as a Control Problem

4.3.1 Problem Formulation

Using an elliptical varifocal mirror in an off-axis configuration, we can build a focusing system for a fiber laser tool as illustrated in Fig. 4-8. In this system, the laser beam exiting the optical fiber is collimated by a thin lens and reflected in 90° by a fixed mirror. The diameter of the collimated laser beam is D_M. Then the collimated beam reaches the varifocal mirror with an incidence angle of 45°, being reflected at 90°. If the aspect ratio of the varifocal mirror is $\alpha = \sqrt{2}$, the collimated beam is properly focused at a distance f_M of the center point of the mirror.

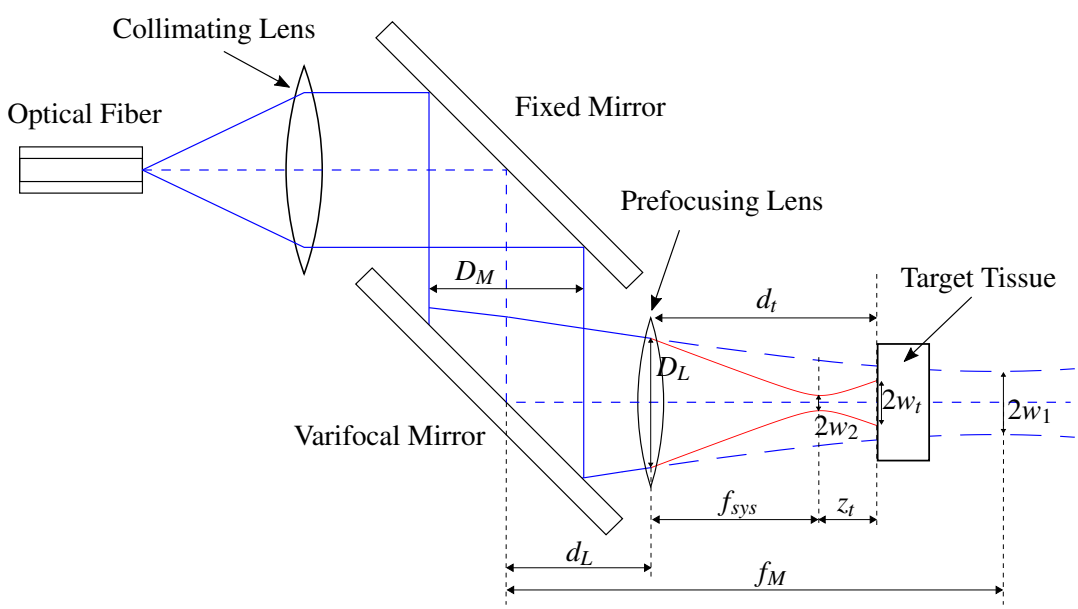

Figure 4-8: Diagram of focusing system in a fiber tool using a varifocal mirror.

As indicated in the 4.51, the sign of focal length f_M is the same as the mirror's deflection w_0, which means that the focal length of the beam is only positive when the mirror deflects in the concave direction. To obtain a positive focal length even when the mirror deflects in the convex direction, a convergent lens can be placed in front of the mirror. The equivalent focal length of the system f_{sys}, obtained by the combination of the varifocal mirror and this prefocusing lens is given by

$$\frac{1}{f_{sys}} = \frac{1}{f_L} + \frac{1}{f_M - d_L} \rightarrow f_{sys} = \frac{f_L(f_M - d_L)}{f_L + f_M - d_L}, \tag{4.52}$$

where f_L is the focal length of the prefocusing lens and d_L is the distance between the prefocusing lens and the center of the varifocal mirror. The diameter of the focused laser spot obtained by this focusing system can be determined based on the waists w_1 and w_2 of the beams focused by the varifocal mirror and the prefocusing lens, respectively. These can be calculated using the Gaussian beam propagation equations presented in Section 2.2. The waist of the beam focused only by the mirror (assuming the prefocusing lens was removed) can be obtained by

$$w(f_M) = \frac{D_M}{2} = w_1 \sqrt{1 + \left(\frac{f_M}{z_{R1}}\right)^2} \tag{4.53}$$

where

$$z_{R1} = \frac{\pi w_1^2}{M_1^2 \lambda} \tag{4.54}$$

is the Rayleigh range associated to the waist w_1 and M_1^2 is the beam quality factor of the beam reflected by the varifocal mirror. Using the far-field approximation (i.e. assuming $f_M \gg z_{R1}$), we are able to calculate w_1 as

$$w_1 = \frac{2M_1^2 \lambda}{\pi} \frac{f_M}{D_M} \tag{4.55}$$

This allows us to calculate the diameter of the beam over the prefocusing lens as

$$w(f_M - d_L) = \frac{D_L}{2} = w_1 \sqrt{1 + \left(\frac{f_M - d_L}{z_{R1}}\right)^2} \tag{4.56}$$

Once again, assuming $f_M - d_L \gg z_{R1}$, we obtain

$$D_L = \frac{2w_1}{z_{R1}} (f_M - d_L) = D_M \frac{f_M - d_L}{f_M} \tag{4.57}$$

which is what one would expect for a perfectly conical beam shape. Using the

same reasoning of 4.53, w_2 can be derived as

$$w_2 = \frac{2M_2^2\lambda}{\pi}\frac{f_{sys}}{D_L} \tag{4.58}$$

with associated Rayleigh range

$$z_{R2} = \frac{\pi w_2^2}{M_2^2\lambda} \tag{4.59}$$

Once again, this result uses the far-field approximation, i.e. it assumes that $f_{sys} \gg z_{R2}$. Replacing the 4.52 and the 4.57 into the 4.58, we obtain the beam waist w_2 as a function of f_M:

$$w_2 = \frac{2M_2^2\lambda}{\pi}\frac{f_L}{D_M}\left(\frac{f_M}{f_M + f_L - d_L}\right). \tag{4.60}$$

It is worth noting that the beam quality factor M_2^2 used in 4.60 is not necessarily equal to the one used in 4.55, as the prefocusing lens itself may add aberrations to the beam. The factor M_1^2 represents the aggregated effects of the quality factor of the original beam M_{beam}^2 and the aberrations created by the fixed elements (collimating lens and fixed mirror) M_{fixed}^2 and the varifocal mirror M_M^2.

$$M_1^2 = M_{beam}^2 M_{fixed}^2 M_M^2 \tag{4.61}$$

The quality factor M_2^2 combines the aberrations of M_1^2 with the aberrations induced by the lens M_L^2

$$M_2^2 = M_1^2 M_L^2 \tag{4.62}$$

Therefore it is necessary to distinguish these terms. From the 4.60, it can be seen that the diameter of the focused laser spot $2w_2$ depends on the focal length of the varifocal mirror f_M. Therefore, if the focal length of the system f_{sys} is set to always match the distance to the target d_t, the diameter of the laser spot may not be constant. To compensate this problem, the beam can be focused at a small distance to the target, given by:

$$z_t = d_t - f_{sys}. \tag{4.63}$$

Assuming this intentional defocusing of the laser beam, the diameter of the laser spot at the target becomes:

$$2w(z_t) = 2w_2\sqrt{1 + \left(\frac{z_t}{z_{R2}}\right)^2}. \tag{4.64}$$

Therefore, the laser focusing problem can be defined as the adjustment of the

focal length of the system f_{sys}, such that the diameter of the laser spot at the target is equal to a target spot diameter $2w_t$. This corresponds to solving the equation

$$w_t = w_2\sqrt{1+\left(\frac{z_t}{z_{R2}}\right)^2}. \tag{4.65}$$

The solution to the 4.65 in terms of f_M is not trivial, since both w_2 and z_t change with f_M.

4.3.2 Simplified Solution

It is possible to obtain a simple solution to the presented laser focusing problem for the particular case when $d_L = f_L$. If the distance between the prefocusing lens and the varifocal mirror is adjusted to match the focal length of the prefocusing lens, the 4.60 reduces to

$$w_2 = \frac{2M_2^2\lambda}{\pi}\frac{f_L}{D_M}. \tag{4.66}$$

This means that the diameter of the focal spot of the system no longer depends on f_M, which means that the laser beam can be focused exactly at the target. In this case the focusing problem can be solved by having $w_2 = w_t$, therefore the solution to the 4.65 becomes simply

$$z_t = 0. \tag{4.67}$$

Limitations of the Simplified Solution

The presented simplified solution is based on two requirements:

1. $d_L = f_L$;
2. The target spot diameter $2w_t$ is determined by twice the expression 4.66.

Although these requirements can be considered reasonable, they may not apply for all situations. For example, the first requirement limits the design of the focusing system by eliminating one degree of freedom. In this case, the selection of f_L must be made considering, at the same time, the focal length range and the overall size of the tool.

Assuming, $d_L = f_L$, the 4.52 becomes

$$f_{sys} = f_L - P_M f_L^2, \tag{4.68}$$

where $P_M = {}^1/_{f_M}$ is the optical power of the varifocal mirror. In this case, the focal length range of the system is given by

$$\Delta f_{sys} = -\Delta P_M f_L^2, \tag{4.69}$$

As it can be seen, the focal length range increases with f_L. Therefore, depending on the focal length range required for the application and the optical power range ΔP_M provided by the varifocal mirror, it may be necessary to use a prefocusing lens with large focal length. However, since the distance between the varifocal mirror and the prefocusing lens must be equal to f_L, this limits the compactness of the overall focusing system.

The second requirement of the simplified solution also limits the design of the focusing tool, especially in applications where the required diameter of the laser spot is relatively large. Moreover, it implies that the target spot diameter w_t cannot change during the operation, since it is fixed by the design parameters of the focusing system. Depending on the application, the ability of changing the diameter of the focal spot during the operation may be necessary, in order to alternate between cutting and coagulating tissue. Considering these limitations, it may be interesting to find a general solution to the 4.65 that does not rely on these two requirements.

4.3.3 General Solution

To solve the focusing problem for the general case, we need to determine the required defocusing of the laser z_t as function of the distance d_t between the target and the focusing system. This consist in obtaining a function F_1 such that:

$$z_t = F_1(d_t). \tag{4.70}$$

To achieve that, we must first isolate z_t in the 4.65, which results in

$$z_t = \pm z_{R2}\sqrt{\left(\frac{w_t}{w_2}\right)^2 - 1}. \tag{4.71}$$

This expression allows us to calculate the required defocusing z_t as a function of w_2, for the case when $w_2 < w_t$. In the case of $w_2 > w_t$, the beam waist is already larger than the target focal spot, which means the focusing system is not able to keep the diameter of the laser spot equal to $2w_t$. Since w_2 depends only on f_M, the 4.71 is also a function of f_M. Analogously, since f_{sys} also depends only on f_M, d_t can also be written as a function of f_M, by isolating d_t in the 4.63:

$$d_t = z_t + f_{sys}. \tag{4.72}$$

Therefore, 4.71 and 4.72 can be written as functions of f_M, such as:

$$z_t = F_2(f_M) = F_4(F_5(f_M)) \tag{4.73}$$

and

$$d_t = F_3(f_M) = F_2(f_M) + F_6(f_M), \tag{4.74}$$

where F_4, F_5 and F_6 correspond to the equations 4.71, 4.60 and 4.52 respectively. Based on that, the general solution to the focusing problem can be obtained as

$$z_t = F_1(d_t) = F_2(F_3^{-1}(d_t)). \tag{4.75}$$

Unfortunately, 4.75 cannot be solved analytically, as the function F_3 cannot be inverted explicitly. However we can calculate it numerically to analyze the behavior of the system. Fig. 4-9 shows the obtained curve for the following set of parameters: $D_M = 4\,\text{mm}$, $d_L = 10\,\text{mm}$, $f_L = 30\,\text{mm}$, $w_t = 250\,\mu\text{m}$, $\lambda = 10.6\,\mu\text{m}$, $M_1^2 = 1.5$, $M_2^2 = 1.65$.

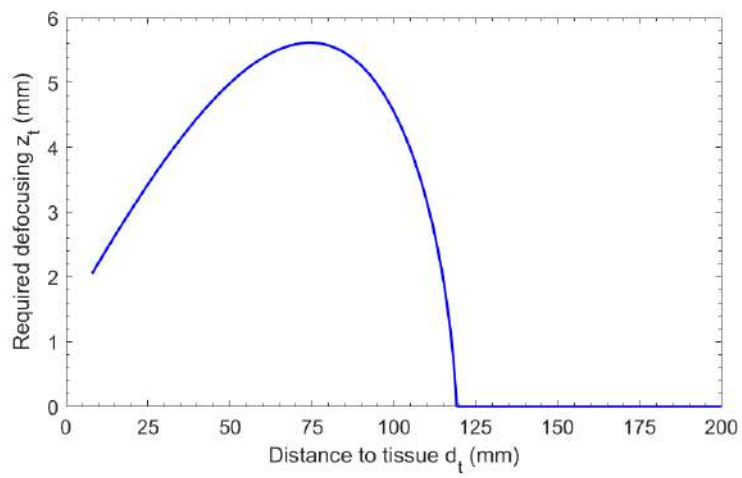

Figure 4-9: Numerical solution to the required defocusing as a function of the distance to the tissue.

As it can be seen, when the target is closest to the system, the required defocusing is small (about 2 mm). This happens because at this point, the numerical aperture of the system is maximal, resulting in short depth of focus. As the distance to the tissue increases, the NA decreases, increasing the required defocusing. This phenomenon persists until w_2 starts approaching w_t, decreasing the required defocusing again. For distances above 120 mm, this system is no longer able to achieve $w_t = 250\,\mu\text{m}$.

It is important to note however that the expression for z_t given in 4.71 can provide two different values. These correspond to the two positions where the laser

beam has the same diameter, before or after the beam waist, as shown in Fig. 4-10. This allows us to chose between two approaches: focus the beam before or inside the tissue.

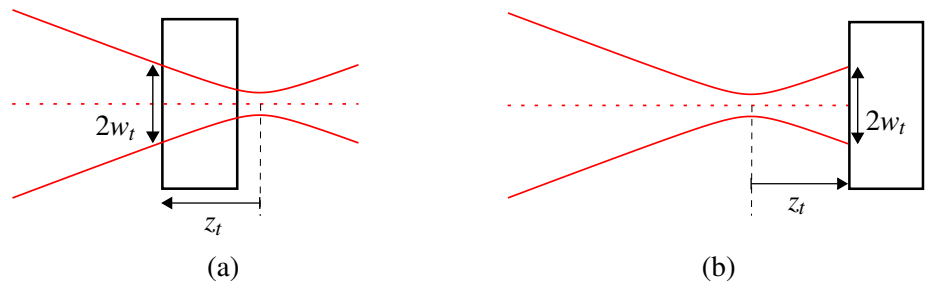

Figure 4-10: Laser focusing with the beam waist placed inside (a) or before (b) the tissue.

There are two main differences between these approaches. The first one is the way the laser beam propagates inside the tissue. However, since the optical penetration of the CO_2 laser in soft tissue is in the order of 10 µm, this difference can be considered negligible. The second one is the numerical aperture of the system, which determines its depth of focus. When a positive defocus is used (the beam is focused inside the tissue), the NA is lower, resulting in higher depth of focus. This makes the system less sensitive to errors in the actuation of f_{sys} or the measured distance d_t. For this reason, the use of a positive defocus increases the robustness of the focusing system.

4.3.4 Errors due to the Far-field Approximations

When formulating the problem and obtaining the general solution, we used the far-field approximation in the equations 4.55, 4.57 and 4.58. However, depending on the range of d_t and the parameters of the system, this approximation may not be always valid. To verify the validity of the obtained results, we calculated z_t numerically without using the far-field approximation and measured the error between this simulation and the value provided by 4.75. The result of this comparison is shown in Fig. 4-11.

As it can be seen, the error is only significant for values of d_t higher than 75 mm. For these values, w_2, and consequently z_{R2}, becomes large, which makes the near-field effects significant. However, even for $d_t = 120$ mm, the error in the calculated z_t was only 0.5 mm. For distances lower than 75 mm, the error is always lower than 5 µm. Therefore we can state that the far-field approximation is good enough, at least for d_t lower than 75 mm.

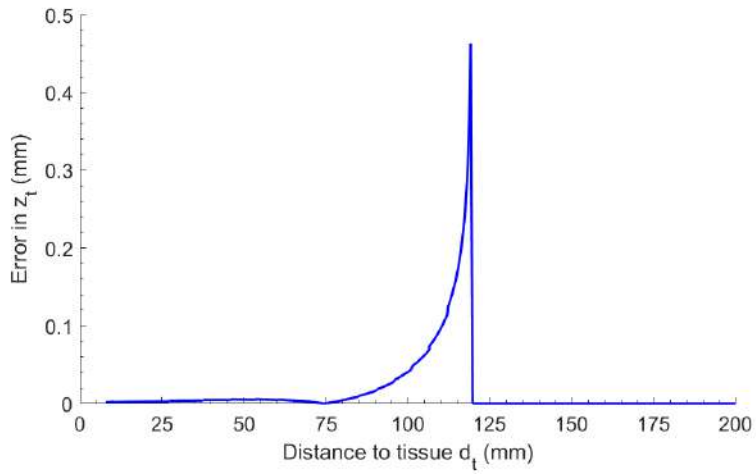

Figure 4-11: Error in the calculated value of z_t due to the far-field approximation.

4.4 Varifocal Mirror Design and Control

With mathematical models to represent the deflection of the varifocal mirror, the focusing of the reflected beam and the requirements of the laser focusing task, we are able to propose methods to control the mirror deflection and to optimize the mirror design based on the application requirements.

4.4.1 Feed-Forward Controller for the Varifocal Mirror

Combining the models presented in Sections 4.1, 4.2 and 4.3, it is possible to design a feed-forward controller to calculate the required actuation pressure Δp as a function of the distance to the target d_t, in order to guarantee that the laser beam is always on focus. This can be obtained by determining the required defocusing of the beam z_t with one of the presented solutions to the focus control task (4.67 or 4.75). If the general solution is used, with $d_L \neq f_L$, the 4.75 can be calculated numerically – based on the parameters of the focusing system – and stored in a lookup table.

Once z_t is determined, the calculation of the actuation pressure Δp can be obtained from the equations 4.72, 4.52, 4.51, 4.27. The complete solution for this feed-forward controller is presented in the following equations:

$$z_t = \text{Lookup Table}(d_t), \tag{4.76a}$$

$$f_{sys} = d_t + z_t, \tag{4.76b}$$

$$f_M = d_L + \frac{f_L f_{sys}}{f_L - f_{sys}}, \tag{4.76c}$$

$$w_0 = \frac{\alpha R_y^2}{4 f_M}, \tag{4.76d}$$

$$\Delta p = \frac{4 w_0 h}{k_\alpha R_y^2} \left((\sigma_0 - \sigma_T) + \frac{2}{3} \frac{w_0^2}{k_\alpha R_y^2} E_\nu \right). \tag{4.76e}$$

4.4.2 Varifocal Mirror Design Considerations

As presented in the previous sections, the deflection of the membrane mirror is defined by four main parameters of the membrane – thickness h, smaller half-axis R_y (or simply radius), aspect ratio α_m and residual stress σ_0 – and the membrane material, which determines E, ν, α and σ_y. Therefore these parameters can be designed in order to optimize the mirror's performance for any given application.

The aspect ratio α determines the angle of incidence θ of the collimated beam that the varifocal mirror is able to focus, as stated in the 4.46. Therefore it must be selected based on the optical setup of the fiber laser tool.

The radius R_y affects the central deflection of the membrane and also the focal length of the deflected mirror. Therefore it is better to analyze the deflection curve $\Delta p(P_M)$ of the mirror, by replacing the 4.76d into the 4.76e:

$$\Delta p = \frac{h\left(1+\alpha^2\right)}{2\alpha} P_M \left((\sigma_0 - \sigma_T) + \frac{E_\nu R_y^2 \left(1+\alpha^2\right)}{48} P_M^2 \right) \tag{4.77}$$

The deflection curve can be expressed in terms of focal length f_M or optical power $P_M = {}^1/_{f_M}$, however the optical power is often preferred to avoid dealing with infinite values. From this deflection curve, it can be seen that R_y only impacts the cubic term. For small deflections, in which the cubic term can be neglected, the required actuation pressure to control the optical power of the mirror does not depend on R_y. The radius of the membrane is mainly responsible for defining the overall size of the varifocal mirror and also the maximum diameter of the collimated beam, as D_M is limited to $2R_y$. As shown in Section 4.1.4, the diameter of the collimated beam plays a large role in the heating of the membrane. Therefore R_y must be made large enough to decrease the power density of the laser beam and avoid damage to the mirror, while still allowing for a compact focusing system.

The membrane thickness h is one of the parameters that determines if the mirror deflection is in the large-deflections regime, since this requires $w_0 \gg h$. To ensure the mirror is always parabolic, the deflection must be in this regime, therefore the membrane thickness must be made as small as possible. Moreover the thickness is directly proportional to the actuation pressure, which means that decreasing h

allows decreasing Δp, which can be useful for miniaturizing the actuation system.

Finally, the residual stress σ_0 is proportional to the linear coefficient of the $\Delta p(f_M)$ expression, but also determines the membrane deflection w_{0y} that causes the membrane to rupture, as shown in equation 4.32. When σ_0 is decreased, the Δp decreases and w_{0y} increases, which means reducing the residual stress of the membrane is important to achieve large deflections. However, the linear term of the $\Delta p(P_M)$ is also proportional to the thermal stress σ_T. This means that the sensitivity of the mirror deflection for ΔT can be decreased by increasing the residual stress.

Having said that, it is also important to note that these parameters cannot be chosen independently, as they are intricately related to the mirror microfabrication process. For example, if the aspect ratio of the membrane (R_y/h) is too large, the membrane becomes fragile, which can decrease the performance of the fabrication process. The same is true for the selection of the membrane material. Even though the material could be selected to provide the optimal set of mechanical properties, this choice also determines which fabrication methods can be employed. This topic is discussed in more details on the next chapter, which presents different methods that can be used to fabricate this type of membrane mirror.

4.5 Conclusions

The models presented in this chapter provide an accurate representation of the deflection of the mirror and the focusing of the laser beam. They contain a few approximations, but the analyses performed in this chapter indicate they are precise enough to allow controlling the focusing of the laser beam based only on the actuation pressure, without the need of measuring f_M. This is desirable since focal length sensors usually require the use of beam splitters, which increases the size of the focusing system significantly.

In the next chapter, we present the microfabrication methods for realizing elliptical membrane mirrors for hydraulic actuation. We present further discussion on the selection of the membrane parameters alongside the steps of the fabrication process. In chapter 6 we characterize the mirrors experimentally in order to validate the proposed models.

5
Mirror Fabrication

In the previous chapter we presented models to describe the deflection of a membrane mirror under uniform pressure and proved that a deflected elliptical mirror is a good approximation of an off-axis paraboloid. We also presented how such type of mirror can be used to focus a laser beam in a fiber laser system. The assumptions made in those models were that the membrane is thin (its thickness is much lower than its central deflection), uniform and that its boundary is elliptical. We also saw that the material properties of the membrane (such as Young's modulus, Poisson's ratio and coefficient of thermal expansion) and the residual stress affect the membrane deflection.

In this chapter we present the microfabrication techniques that allow building such type of membrane mirrors from a silicon wafer. We describe the main steps of the fabrication process and show how they are related to the mirror design.

5.1 Overview of the Fabrication Process

The conceptual design of our membrane mirror for hydraulic actuation is shown in Fig. 5-1. The membrane, which is the structural element of the mirror, consists of an uniform layer of flexible material deposited on a silicon substrate. The substrate contains an etched fluidic chamber that allows applying pressure to the membrane, thus controlling its deflection. The shape of the fluidic chamber determines the boundary of the membrane, therefore defines the surface of the deflected mirror. To maximize the mirror's reflectance, the top layer of the membrane is covered with a reflective coating.

The fabrication process presented here builds the mirror from a single wafer,

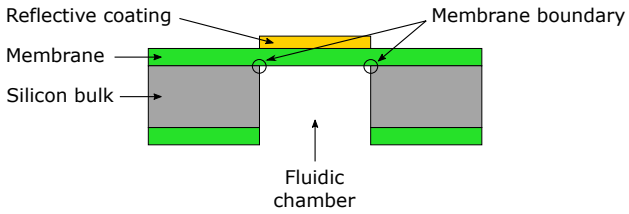

Figure 5-1: Cross-sectional diagram of a membrane mirror with elliptical boundary.

using a combination of surface and bulk micromachining. The process can be divided in four main phases: *membrane deposition*, *patterning of the silicon bulk*, *membrane release* and *coating deposition*. These phases are illustrated in Fig. 5-2 and explained in detail over the following sections.

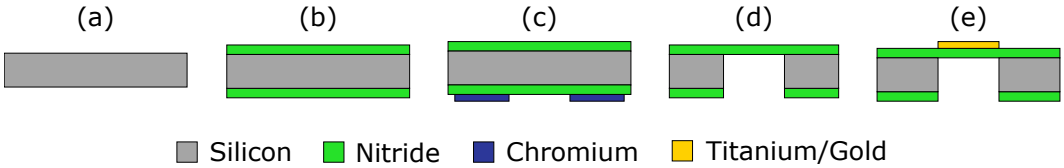

Figure 5-2: Main phases of the fabrication process of the membrane mirror: (a) starting silicon wafer, (b) deposition of membrane layer, (c) patterning the bottom side of the silicon bulk, (d) etching of the fluidic chamber and membrane releasing, (e) deposition of the reflective coating.

5.2 Membrane Deposition

Membrane deposition is the process that creates the membrane layer by depositing material in a controlled way on top of the substrate. Depending on the material of the membrane and the substrate, several deposition methods can be used such as physical vapor deposition (PVD), chemical vapor deposition (CVD) or spin coating (in the case of polymeric membranes). The selection of the deposition method and parameters can determine important properties of the membrane such as uniformity, adhesion to the substrate, residual stress and maximum thickness.

One of the most used materials for fabricating thin flexible membranes is silicon nitride [40], as it provides excellent adhesion to the silicon wafer and good stress uniformity, resulting in low aberrations. The main problem with silicon nitride is that it has a relatively high intrinsic stress, which increases the pressure required to deflect the membrane. For this reason, recent varifocal mirrors with electrostatic actuation use polymeric membranes made from SU-8 2002, whose intrinsic stress can be up to ten times lower than silicon nitride [68]. In this project, however, since we are using hydraulic actuation to deflect the membrane, which can create a much higher pressure than electrostatic, we decided to use silicon nitride membranes.

To deposit silicon nitride on a silicon substrate, CVD is the most appropriate method. In this process, the wafer is inserted in a reactor where two gas reactants interact to create silicon nitride molecules (Si_3N_4). Molecules are deposited as a thin film, which provides high uniformity and good adhesion to the silicon substrate. The thickness of the film is controlled by the amount of reactants and the duration of the process. Typical film thickness that can be deposited with this method range from 10 nm to 2 µm.

In this project, two different deposition methods were compared: low pressure CVD (LPCVD) and plasma enhanced CVD (PECVD). The LPCVD process produces membranes with higher uniformity and lower residual stress, but requires very high temperatures (between 700 °C and 800 °C), which could not be achieved by the equipment available in our clean room. For this reason, we used silicon wafers industrially coated with 500 nm of LPCVD silicon nitride on both sides. On the other hand, the PECVD process can operate at lower temperature since the activation energy of the reaction is lowered by an RF-induced plasma, which gives us more flexibility in selecting the thickness of the film. To achieve good mechanical stability, we tested films with thickness of 1 µm and 2 µm. The difference between those membranes is better evidenced during the membrane release process, presented in Section 5.4.

5.3 Patterning of the Silicon Bulk

The process of patterning the silicon bulk consists in depositing and patterning a masking layer on the bottom side of the silicon substrate to allow selective etching of the silicon bulk for creating the fluidic chamber. This process is achieved with photolithography and is illustrated in Fig. 5-3.

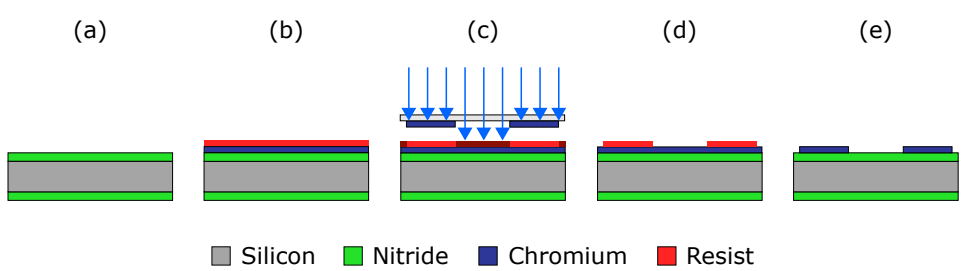

Figure 5-3: Fabrication process for patterning the silicon bulk: (a) starting wafer coated with silicon nitride, (b) deposition of the chromium and photoresist layers, (c) exposure of the photoresist with UV light through a lithographic mask, (d) development of the exposed resist, (e) etching of the chromium and resist stripping.

First, a masking layer – such as chromium – is deposited on the silicon bulk through a PVD process, such as sputtering or evaporation. Then, a photoresist layer is spun on top of the masking layer. After that, the photolithography takes place,

which consist on using a lithographic mask to selectively expose the photoresist to UV light. During development, the exposed areas of photoresist are removed, exposing part of the masking layer, which can then be etched away. After etching the masking layer, the remaining photoresist is stripped with solvent.

In summary, this process allows replicating the pattern of the lithographic mask on the masking layer deposited on the silicon bulk. However, the process of fabricating the mask itself is similar to this, as illustrated in Fig. 5-4. The main difference is that the exposure of the photoresist is done by a direct laser writer, which uses a focused beam to expose individual pixels of the photoresist. Because of that, patterning of the lithographic mask can take several hours.

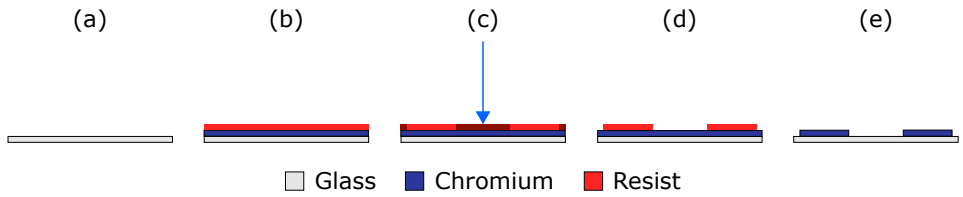

Figure 5-4: Fabrication process for creating the lithographic mask: (a) starting glass wafer, (b) deposition of the chromium and photoresist layers, (c) selective exposure of the photoresist using a laser writer, (d) development of the exposed resist, (e) etching of the chromium and resist stripping.

The pattern of the lithographic mask is used to define the shape of the fluidic chamber, but also the edges of the mirror sample, which are used for dicing the wafer into individual mirrors. This allows fabricating samples with exact external dimensions, which is important for integrating the membrane mirrors to the hydraulic actuation system. Fig. 5-5 shows two different masks used in this project for fabricating circular and elliptical membranes. The circular mask contains patterns with several different diameters. This was used to compare different types of mirrors in the early stages of the project. The elliptical mask contains only two different patterns of mirror, but allows fabricating an entire batch of 52 samples from a single silicon wafer.

5.4 Membrane Release

The membrane release process consists on etching the entire thickness of the silicon bulk – from the patterned bottom side until the top nitride layer – creating a freestanding membrane. To transfer the shape patterned in the masking layer to the membrane boundary, the silicon must be etched vertically. This can be achieved using a Deep Reactive-Ion Etching (DRIE) process. However, since the DRIE process has low selectivity for the silicon nitride, it is very difficult to etch the entire silicon bulk without etching the nitride as well. To solve this problem, two etching meth-

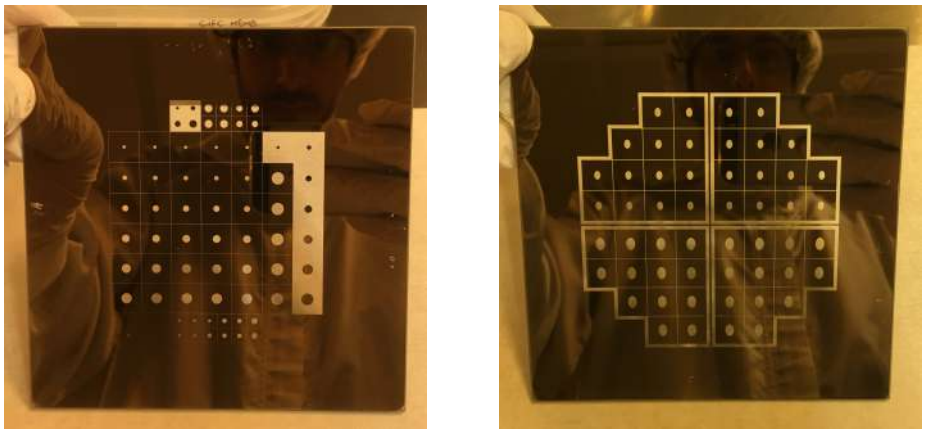

(a) (b)

Figure 5-5: Lithographic masks used to fabricate circular (a) and elliptical (b) membranes.

ods are presented here: a combination of DRIE and wet etching and a DRIE-only process with an etch-stop layer.

5.4.1 Membrane Release using DRIE and Wet Etching

Fig. 5-6 illustrates the process of membrane releasing through DRIE and wet etching. First, the bottom nitride layer is removed using Reactive-Ion Etching (RIE). Then the DRIE process is performed to etch the silicon bulk. Since the DRIE is a cyclic process, it is possible to select the number of cycles in order to leave a thin layer of silicon before reaching the membrane. Once the DRIE is interrupted, the masking layer and the remaining silicon layers are removed with wet etching, using solutions with high selectivity for the nitride, which allow releasing the membrane without damaging it.

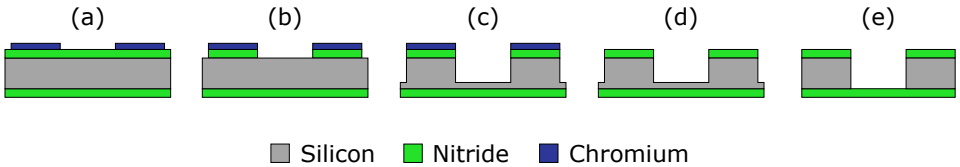

Figure 5-6: Membrane releasing process using DRIE and wet etching: (a) starting wafer with patterned chromium mask, (b) RIE of the nitride layer, (c) timed DRIE of the silicon bulk leaving a thin layer of silicon, (d) wet etching of the chromium mask, (e) wet etching the remaining silicon.

To calculate the required amount of DRIE cycles to leave only a thin layer of silicon, the etching rate of the DRIE was measured for every process. This was

obtained using a profilometer to measure the depth of etched silicon several times during the etching process. These measurements required interrupting the etching process and removing the samples from the DRIE reactor. This was also useful for keeping the temperature of the DRIE reactor constant, as it tends to warm up during a long etching process, despite its temperature controller. However, the profilometer measurements were only performed for the initial cycles of the process, since after 300 µm of etching there was a risk of damaging the sample while measuring it. Because of the uncertainty on the exact etching rate at the end of the process, we decided to leave at least 100 µm of silicon to be removed with the wet etching.

Anisotropic Wet Etching with KOH and TMAH

The first solution we used for etching the remaining silicon was potassium hydroxide(KOH), as it is a common silicon etchant and has excellent selectivity for silicon nitride. However, when we tried etching the wafer with the PECVD nitride, the membrane layer peeled off during the process. This indicates that the PECVD nitride contains pin-holes distributed along the membrane, due to the low uniformity of the deposition, which allow the KOH to etch the top silicon layer underneath the membrane. Based on that, we concluded that our PECVD nitride is not suitable for wet etching.

When etching the LPCVD nitride, the membrane remained intact, however its boundary did not preserve the shape patterned on the bottom side of the silicon bulk. The membrane boundary became rectangular, even if the hole etched by the DRIE was perfectly elliptical. This occurred because KOH is an anisotropic etchant, which means it does not etch all planes of the silicon's crystalline structure equally. In fact, KOH etches the planes $\langle 1\,0\,0 \rangle$ and $\langle 1\,1\,0 \rangle$ much faster than the $\langle 1\,1\,1 \rangle$ plane, as illustrated in Fig. 5-7. The same result was obtained with tetramethylammonium hydroxide (TMAH), another common silicon etchant, as it also etches silicon anisotropically.

Isotropic Wet Etching with HNA

To etch silicon isotropically, one can use a solution of hydrofluoric acid (HF), nitric acid and acetic acid called HNA [69]. The etching principle of HNA is based on two simultaneous chemical reactions. Nitric acid oxidizes the silicon, while the HF etches the silicon oxide. The acetic acid is used simply as diluent and is sometimes replaced with water.

According to the literature [69], HNA should not etch silicon nitride, however we observed etching of the membrane with an approximate selectivity of 200:1 in respect to silicon. This means that in the time needed to etch the remaining 100 µm of silicon, 500 nm of nitride were etched, which corresponds to the total thickness of our LPCVD membrane. The reason we observed lower selectivity than expected

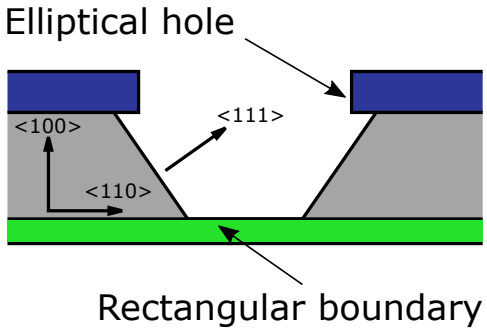

Figure 5-7: Anisotropic wet etching of silicon. Since the $\langle 1\,1\,1 \rangle$ plane is etched much slower than the $\langle 1\,0\,0 \rangle$ and the $\langle 1\,1\,0 \rangle$ planes, the boundary of the released membrane becomes rectangular, even when the patterned hole in the masking layer is elliptical.

is probably because our nitride layer has low residual stress, which is sometimes referred to as silicon-rich nitride.

Enhanced DRIE process

Since both isotropic and anisotropic solutions resulted in poor membrane release (due to distortion of the membrane boundary or membrane thinning), we decided to modify the DRIE process to reduce the thickness of the remaining silicon layer. To achieve that, we used the following process. First, a single sample (containing one single mirror) was inserted in the reactor and the DRIE was performed for 30 cycles. Then another sample was inserted and 30 more cycles of DRIE were performed. After that, all other samples were inserted and the DRIE was performed as before, until the thickness of the remaining silicon layer was around 100 µm. After that, the DRIE process was continued with visual inspection of the samples at every 20 cycles. The process was only interrupted when the silicon in the first sample inserted in the reactor was completely etched (breaking the membrane layer of that sample). This allowed us to obtain samples with less than 10 µm of remaining silicon. The main inconveniences of this process are that it cannot be applied to an entire silicon wafer and that one or two samples need to be sacrificed for every batch.

HNA Etching with Thinner Silicon Layer

With a thinner layer of remaining silicon, it was possible to release the membrane using the HNA solution. Fig. 5-8 shows a scanning electron microscopy (SEM) of a membrane released with this method. As it can be seen, the etching is perfectly isotropic and the shape of the obtained membrane boundary is the same patterned on the silicon bulk.

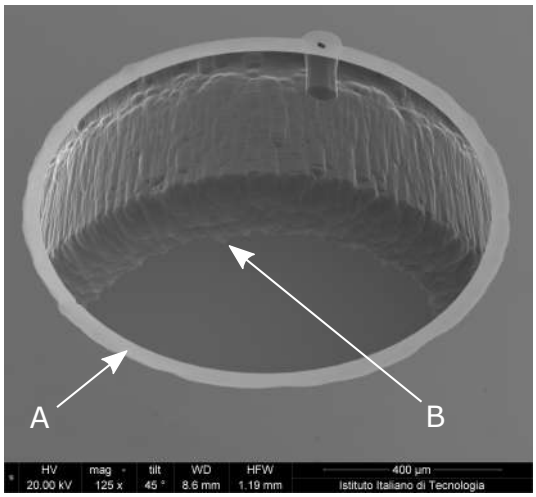

Figure 5-8: SEM of the membrane (bottom side view) released with the HNA solution, indicating the shape patterned on the silicon bulk (A) and the obtained membrane boundary (B).

Isotropic Wet Etching with TMAH/IPA

To avoid the membrane thinning caused by the HNA solution, we also tried to release the membrane using a solution of TMAH with 20% of isopropanol (TMAH/IPA). Isopropanol is known to reduce the etching rate of TMAH and increase the smoothness of the etched structures, thus making it less anisotropic [70]. Using this solution and the samples with thinner silicon layer, we were able to release the membrane as shown in Fig. 5-9. As it can be seen, the membrane boundary looks perfectly circular, even though the walls of the fluidic chamber show signs of anisotropic etching.

Conclusions About the Wet Etching Process

We believe none of the obtained solutions is ideal. The TMAH/IPA solution distorts the shape of the membrane boundary unless the remaining layer of silicon is very thin. This requires using an iterative DRIE method, which cannot be applied to the entire wafer and requires constant monitoring. On the other hand, the HNA solution did not provide enough selectivity to allow releasing the membrane without significant thinning. However, between the two solutions presented here we decided to use the TMAH/IPA as the preferred approach, since it provides satisfactory results on the membrane release without thinning the nitride layer.

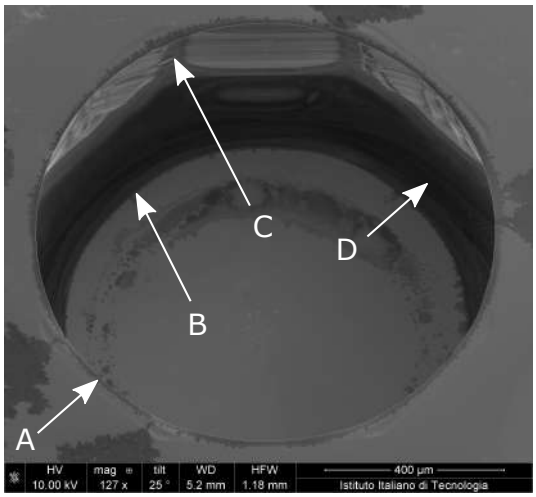

Figure 5-9: SEM of the membrane (bottom side view) released with the TMAH/IPA solution, indicating the shape patterned on the silicon bulk (A), the obtained membrane boundary (B), the walls of the fluidic chamber (C) and the $\langle 1\,1\,1 \rangle$ plane (D).

5.4.2 Membrane Release using DRIE with an Etch-Stop Layer

To avoid the issues associated with the wet etching of the silicon bulk, we can etch the entire thickness of the silicon wafer using the DRIE process. This requires depositing an etch-stop layer, such as silicon dioxide, between the silicon bulk and the nitride layer, as illustrated in Fig. 5-10. Since the DRIE has high selectivity for this material, a 1 or 2 µm thick layer of silicon dioxide is enough to protect the nitride layer. Once the DRIE is finished, the silicon dioxide can be etched with buffered HF (BHF).

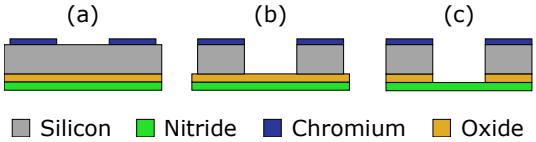

Figure 5-10: Membrane releasing process using DRIE with an etch-stop layer: (a) starting wafer with patterned chromium mask, (b) DRIE of the silicon bulk until reaching the silicon dioxide layer, (c) wet etching of the silicon dioxide with BHF.

Even though this process is simpler than the presented process involving wet etching, it cannot be performed with the LPCVD nitride wafers, since it is not possible to insert the silicon dioxide layer between the silicon bulk and the LPCVD nitride. This means we have to use the PECVD nitride (which has lower uniformity and higher residual stress than the LPCVD), or buy custom wafers with silicon dioxide and LPCVD nitride.

We attempted to perform this process on single-side polished silicon wafers, but

until now this was unsuccessful. The reason for that was because the roughness of the unpolished silicon side, where the chromium layer was deposited, caused some regions of the silicon dioxide layer to be exposed before others. In our experiments, the amount of DRIE cycles between the first exposure of part of the dioxide layer and the complete etching of the silicon was more than 100. This difference was large enough for the DRIE to be able to etch the section of the dioxide exposed first, causing the rupture of the membrane. In the near future, we expect to avoid this problem, by using a double-side polished wafer. This was not done so far, because those wafers were not available in our clean room.

5.4.3 Alternative Membrane Release Methods

Before closing this section, we would like to present two other membrane release methods, which could be used as alternatives to the ones implemented in this project.

The method based on sacrificial layer (illustrated in Fig. 5-11a) has been implemented in [40] and is very similar to the DRIE method with etch-stop layer. The main difference here is that the wafer's top surface can be patterned before the deposition of the etch-stop sacrificial layer. After the sacrificial layer and the nitride are deposited, the silicon bulk is etched from the bottom side with DRIE until reaching the sacrificial layer. The sacrificial layer is then removed with a wet etchant with high selectivity for both the nitride and the silicon. The main advantage of this method is that the membrane boundary is defined by the initial patterning of the top side of the silicon bulk, not by the wet etching release process, which provides more precise definition of the boundary shape.

The wafer bonding method, used in [53], fabricates the mirror from two separate wafers, as illustrated in Fig. 5-11b. In this method, the membrane is deposited on a *membrane wafer* and released with anisotropic wet etching, resulting in a rectangular boundary. Then the fluidic chamber is patterned on a *support wafer*, by etching through the wafer with DRIE. After that, the two wafers are bonded at high pressure using an adhesive film. As long as the released membrane is larger than the patterned fluidic chamber, the boundary of the membrane deflection is defined by the support wafer. The main advantage of this process is that the fabrication of the *membrane wafer* and *support wafer* are relatively simple, but the wafer bonding process requires precise alignment between the two wafers.

5.5 Coating Deposition

5.5.1 Metallic and Dielectric Coatings

Despite having good mechanical properties, silicon nitride has low reflectance for visible light and infrared radiation. For this reason, the top of the membrane must

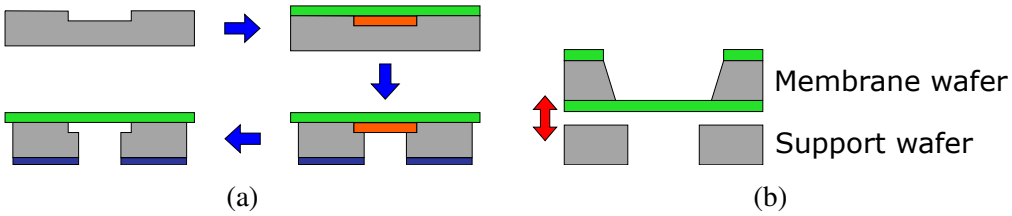

Figure 5-11: Alternative membrane release methods based on (a) patterning of a sacrificial layer or (b) wafer bonding.

be covered with a reflective coating. There are two types of reflective coatings: metallic and dielectric. Metallic coatings consist of thin films of metals, such as gold, silver or aluminum. They provide high reflectance for large spectrum, reaching up to 98% for infrared radiation. The thickness of the film typically ranges from 100 to 250 nm.

Dielectric coatings, on the other hand, are composed of several layers of dielectric materials with alternating refractive indexes, as illustrated in Fig. 5-12. Due to the contrast of refractive index, light is reflected at each interface of materials. The interference between the reflected waves depends on the thickness of the layers and the wavelength of the beam. Therefore it is possible to optimize the coating design, so that all interferences are constructive for a specific wavelength. This results in extremely high reflectance for a narrow band near the designed wavelength, reaching up to 99.9% [71].

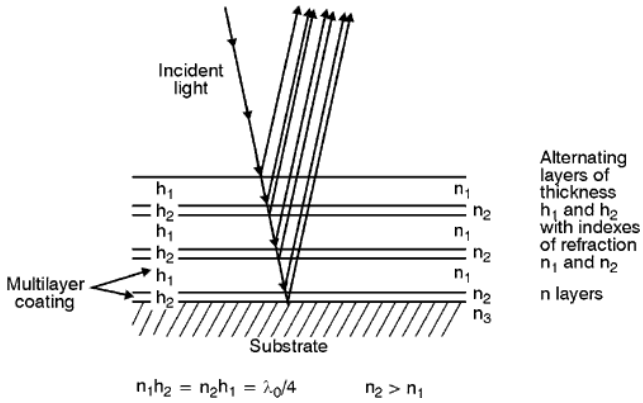

Figure 5-12: Operating principle of a high-reflectance multilayer dielectric coating.

This means dielectric coatings are more effective for reflecting a specific wavelength, but they are also much thicker. To ensure constructive interference, the path-length differences of the beams reflected on each layer must be integer multiples of the designed wavelength. This means the thickness of the layers must be in the order of $\lambda/4$. For CO_2 laser ($\lambda = 10.6\,\mu$m), the thickness of each layer must be around 2.5 µm. This means the minimum thickness of the coating should be be-

tween 10 µm and 15 µm, which is at least 20 times higher than the thickness of our nitride membrane.

Even though high reflectance is important for focusing high-power laser, the thickness of the dielectric coating makes it incompatible with our thin flexible membrane. For this reason, we decided to apply a metallic coating.

5.5.2 Deposition Methods for Metallic Coating

There are two main methods to deposit and pattern the metallic coating over the released membrane. The first one is the top-down approach. In this case, the metallic film is deposited over the entire nitride layer, using a PVD process such as sputtering or evaporation. Then photolithography is used to pattern the deposited coating, leaving the metal only over the released membrane. This process is similar to the one used to pattern the masking layer (illustrated in Fig. 5-3), however the lithographic mask used here is the negative of the previous one. To guarantee the proper patterning of the coating, it is necessary to align the lithographic mask to the fluidic chamber etched in the silicon bulk. This can be done by using a mask aligner with a bottom side microscope, which allows visualizing features on the bottom side of the wafer.

The second method is called lift-off and uses a bottom-up approach, as shown in Fig. 5-13. In this case, photoresist is spun on top of the released membrane and patterned using the same lithographic mask used to pattern the masking layer. In this case the mask is aligned to the membrane itself since it is visible through the photoresist. After the photoresist is developed, the metallic coating is deposited using evaporation. Finally, the photoresist is removed with solvent, which peels off the outer areas of the coating, leaving it only on top of the membrane. To increase the performance of this operation, a sacrificial layer, such as Lor 7B, is commonly deposited between the membrane and the photoresist. This sacrificial layer is etched by the developer faster than the photoresist resulting in an undercut, which prevents adhesion between the coating and the segment of the metallic film that must be removed.

5.6 Complete Fabrication Process

This section presents the complete fabrication process used to build membrane mirrors, using the LPCVD nitride and the wet etching membrane release method. The process is summarized in Fig. 5-14.

We start the process with the silicon wafers industrially coated with 500 nm of LPCVD silicon nitride on both sides. Then we deposit a 250 nm thick layer of chromium on the bottom nitride layer and pattern it using photolithography. Once the chromium is patterned, the silicon bulk is etched using the enhanced DRIE

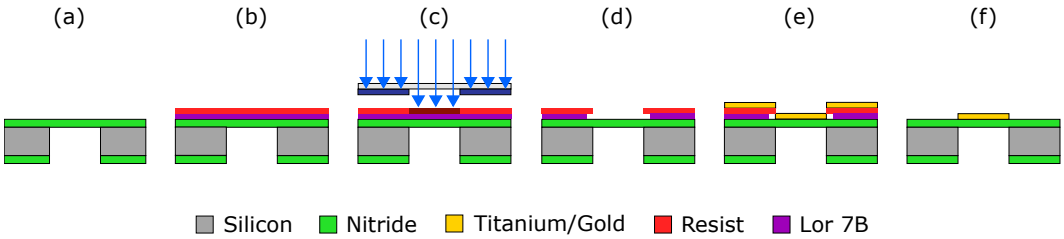

Figure 5-13: Coating deposition through lift-off process: (a) released membrane, (b) deposition of Lor 7B and photoresist layers, (c) exposure of the photoresist with UV light through the lithographic mask, (d) development of the photoresist and Lor 7B creating undercut, (e) evaporation of the gold coating, (f) removal of the photoresist and Lor 7B layers with solvent.

process. The DRIE is interrupted leaving around 10 µm of silicon before reaching the membrane. Then the chromium layer is removed with chromium etchant and the remaining silicon is etched with the TMAH/IPA solution. After the membrane is released it is coated with a Titanium-Gold film (7 nm of titanium and 200 nm of gold), deposited with a lift-off process. The titanium layer is used to increase the adhesion between the nitride and the gold layers.

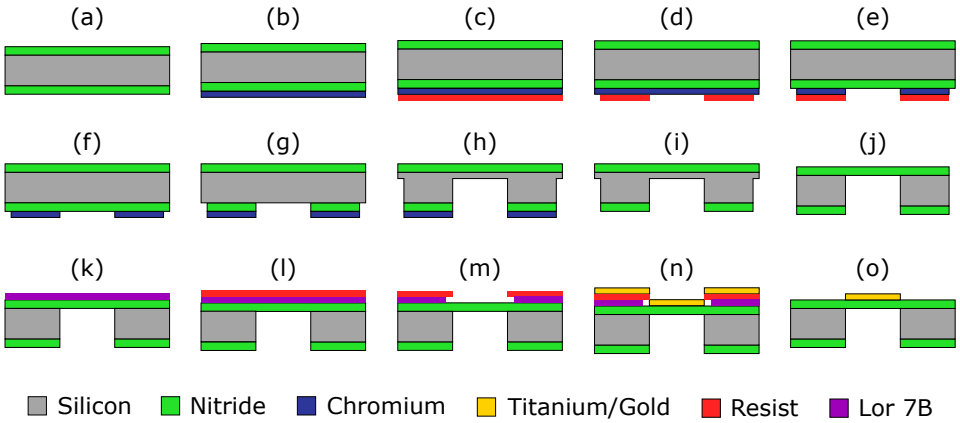

Figure 5-14: First version of the complete fabrication process: (a) starting wafer coated wiht LPCVD nitride on both sides, (b) chromium deposition, (c) resist spinning, (d) 1st photolithography, (e) chromium etching, (f) resist stripping, (g) RIE etching of the bottom nitride layer, (h) timed DRIE etching of the silicon bulk, (i) chromium etching, (j) wet etching of the remaining silicon, (k) Lor 7B spinning, (l) resist spinning, (m) 2nd photolithography, (n) evaporation of the titanium and gold films, (o) lift-off.

5.6.1 Obtained Results

Fig. 5-15 shows a circular and an elliptical membrane mirror obtained with this fabrication process. The diameter of the circular mirror is 4 mm, while the dimensions of the elliptical mirror are 3 x 4.24 mm. The outer edges of all samples were selected as 10 mm x 10 mm to facilitate handling the mirrors.

(a) (b)

Figure 5-15: Fabricated membrane mirrors with circular (a) and elliptical (b) boundary (1 euro cent coin as size reference). OBS: The picture of the circular mirror has been taken after experimental characterization with this sample, which is why the edges of the nitride layer are scratched.

When fabricating this mirror, it was possible to identify two main problems with this fabrication process. The first problem is that the samples become very fragile after releasing the membrane, since its aspect ratio (diameter of the membrane divided by its thickness) is very large. Because of that, steps performed after releasing the membrane (steps 'k' to 'o') have a relatively high chance probability of destroying the sample. This effect was more significant for mirrors of larger diameter. In the case of the 4 mm mirror, the average survivability of the samples at the end of the process was around 40%.

The second problem is that drying the samples after the membrane is released becomes challenging, since a strong flow of compressed nitrogen (standard method for drying samples) can rupture the membrane. This makes difficult to properly clean the membrane after the development of the second lithography (step 'm'). This problem is enhanced by the undercut produced in the Lor 7B layer, which helps trapping residual molecules of the developer. Due to such improper cleaning of the membrane, the quality of the gold deposition is compromised, as it can be seen in Fig. 5-16. These molecules trapped between the nitride and the gold layers decrease the flatness of the mirror, lowering its optical quality.

5.7 Improved Fabrication Process

To eliminate these problems, the fabrication process has been modified to perform the membrane releasing as the last step of the process, as shown in Fig. 5-17. By

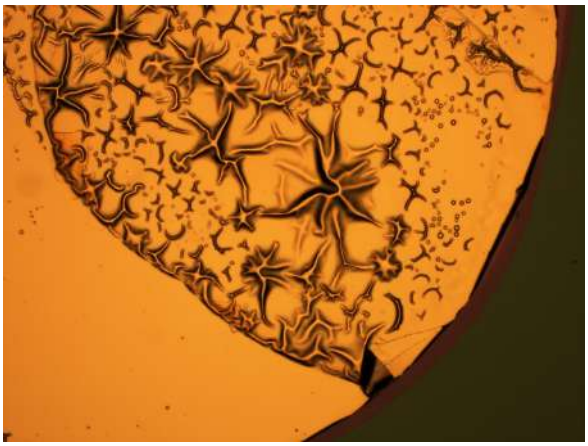

Figure 5-16: Optical microscopy of defects on the reflective coating due to impurities trapped between the nitride and gold layers.

changing that, the survivability of the process has increased to 85% and the defects in the gold coating disappeared. The process also became shorter since most steps can be performed on an entire wafer. Steps 'a' to 'h' can be performed on the entire wafer. Step 'i' requires splitting some samples from the wafer to identify the stopping point for the DRIE. Step 'j' is the only one being performed in individual samples.

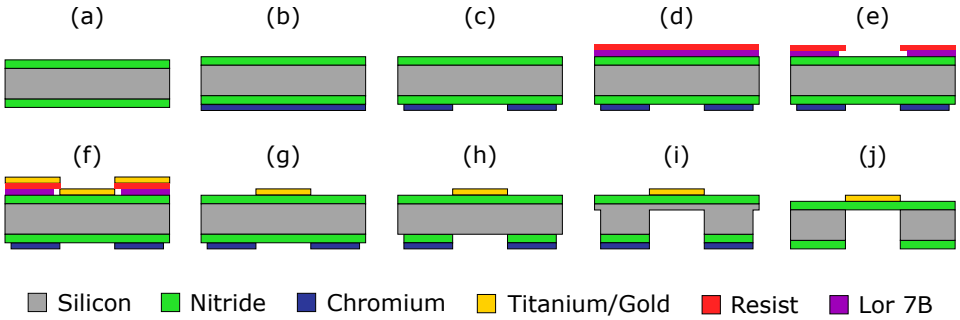

Figure 5-17: Improved version of the complete fabrication process: (a) starting wafer coated wiht LPCVD nitride on both sides, (b) chromium deposition, (c) patterning of chromium through photolithography, (d) Lor 7B and photoresist deposition, (e) 2nd photolithography with bottom side alignment, (f) evaporation of the titanium and gold films, (g) lift-off, (h) RIE etching of the bottom nitride, (i) timed DRIE etching of the silicon bulk, (j) chromium etching and wet etching of the remaining silicon.

5.8 Conclusion

This chapter presented the microfabrication process used to build circular and elliptical mirrors from a single wafer. These mirrors consist on freestanding LPCVD silicon nitride membranes coated with a titanium-gold film. The boundary of the mirror is defined by the shape of the fluidic chamber etched in the silicon bulk, which is defined by the lithographic mask used. Using this process, we were able to fabricate elliptical mirrors of up to 3 x 4.24 mm of diameter. The next chapter presents the experimental characterization of these mirrors.

6
Experimental Characterization

In this chapter, we present the experimental characterization of the fabricated varifocal mirrors. The goal of the experiments presented here is to determine how the mirror deflects with the applied pressure and the CO_2 laser irradiation. The results of these experiments are used to validate the models presented in chapter 4 and to evaluate the quality of the microfabrication process presented in chapter 5.

First, we present the hydraulic actuation system developed to control the pressure applied to the varifocal mirror. Then we present the method we applied for measuring the mirror deflection using a wavefront sensor. After that, we present three sets of experiments for static, thermal and dynamic characterization of the developed prototypes. In the static characterization, we measure the relationship between the applied pressure and the focal length of the mirror. We also analyze how the optical aberrations induced by the mirror change with the applied pressure. In the thermal characterization, we analyze how the CO_2 laser irradiation affects the mirror deflection. Finally, in the dynamic characterization, step response experiments are performed to measure the settling time of the varifocal mirror in conjunction with the hydraulic actuation system.

At the end of the chapter, we summarize the obtained results and compare the performance of the fabricated mirrors with other mirrors presented in the literature.

6.1 Hydraulic Actuation System

To control the pressure applied to the mirror, we implemented a hydraulic actuation system using the microinjection system CellTram® vario (Eppendorf). This microinjection system contains a piston actuated by a DC motor that allows dis-

placing mineral oil through a microfluidic tube with inner diameter of 1 mm. Its maximum volumetric displacement is 960 µL, with a resolution of 2 nL and it is compatible with pressures up to 2 MPa.

To connect the microfluidic tube to the fluidic chamber of the varifocal mirror, we designed a mirror holder part, as shown in Fig. 6-1. The mirror holder contains a 10 x 10 mm square hole where the varifocal mirror must be inserted. At the center of the square hole there is a 2 mm microfluidic channel that links it to the connector for the microfluidic tube. The microfluidic channel is also connected to a side channel that can be used to remove air bubbles when filling the system with oil. Once all the air has been removed from the system, the side channel can be closed with a cap.

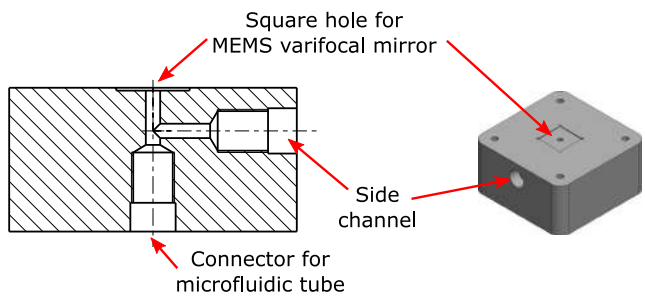

Figure 6-1: Design of the mirror holder part used to connect the fluidic chamber of the varifocal mirror to the microfluidic tube of the microinjection system. The side channel is used to remove air from the system while filling it with oil.

Fig. 6-2 illustrates the varifocal mirror connected to the mirror holder. The mirror is secured in place by a cover part, which is connected to the mirror holder by four screws. To prevent leakage of the oil from the fluidic chamber, a latex sealing sheet layer is placed between the mirror and the holder.

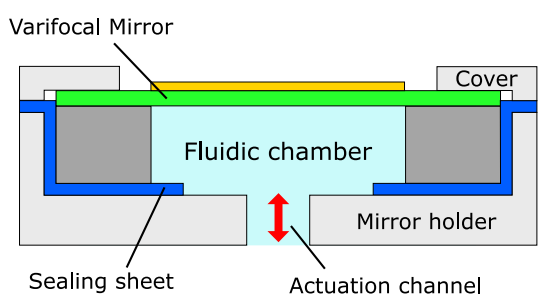

Figure 6-2: Schematic diagram of the varifocal mirror connected to the mirror holder part.

Fig. 6-3 shows the complete hydraulic circuit used to actuate the mirror. As it can be seen, a differential pressure sensor was connected to the actuation channel to measure the pressure in the fluidic chamber of the mirror. The sensor used was

a HSC TruStability pressure sensor (Honeywell, USA) for the pressure range of ± 6895 Pa. The total band error of this sensor is ± 69 Pa.

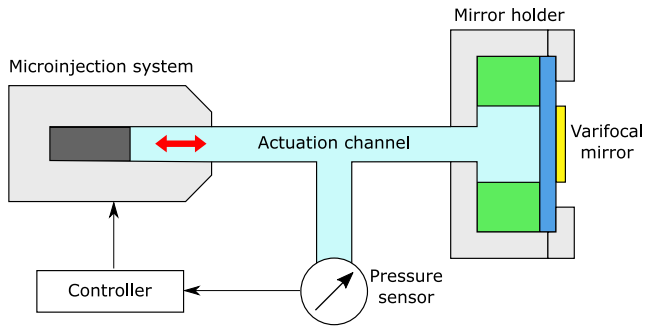

Figure 6-3: Hydraulic actuation circuit composed of mirror holder, microinjection system, pressure sensor and controller.

The controller used for reading the pressure sensor and commanding the microinjection system was an Arduino Nano microcontroller connected to a personal computer (PC) through the serial port. The low-level controller, implemented on the Arduino, was a PID controller for the pressure in the actuation channel, with the reference pressure being provided by the PC. The high-level software, implemented on the PC using Matlab, contained a graphical user interface allowing us to select the mirror deflection, tune the parameters of the PID controller and run several automated routines for system calibration and experimental characterization.

6.2 Methods for Measuring Mirror Deflection

To measure the deflection of the mirror as a function the applied hydraulic pressure, we used a collimated laser beam and a Shack-Hartman wavefront sensor, as shown in Fig 6-4. The wavefront sensor is a device that analyzes a cross section of a propagating beam and reconstructs the shape of its entire wavefront. This information is sufficient to completely determine the propagation of the beam in free space, which allow us to obtain the focal position of the beam as well as to measure the present optical aberrations. By irradiating the mirror with a collimated beam, which has a flat wavefront, the wavefront of the reflected beam can give us full information about the shape of the deflected mirror. For example, if the mirror is perfectly parabolic, the reflected beam will have a spherical wavefront.

The operating principle of the wavefront sensor is illustrated in Fig. 6-5. The wavefront sensor is composed of a CCD sensor and a microlens array. When the propagating beam reaches the microlens array, each microlens creates a focused spot on the CCD sensor. The coordinates of each focal spot allow us to calculate the gradient of the wavefront at the center of the microlens. Combining the measurements from all microlenses, the shape of the entire wavefront is reconstructed

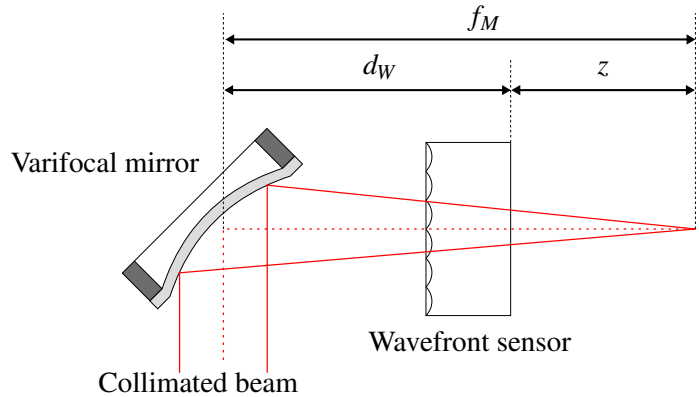

Figure 6-4: Schematic diagram of the measurement system for the focal length of the mirror f_M using a wavefront sensor.

as a series of Zernike polynomials. This is usually done by fitting the Zernike coefficients to the measurements using a least mean square method.

As mentioned in Section 2.2.3, each Zernike polynomial represents an optical aberration. Therefore the magnitude of the Zernike coefficients allows us to quantify the optical aberrations induced by the mirror, such as astigmatism, spherical aberration and others. One coefficient in particular, Z5, is used to calculate the radius of curvature of the wavefront *RoC*, which can be used to estimate the focal length of the mirror. The next sections present two different methods for making such estimation.

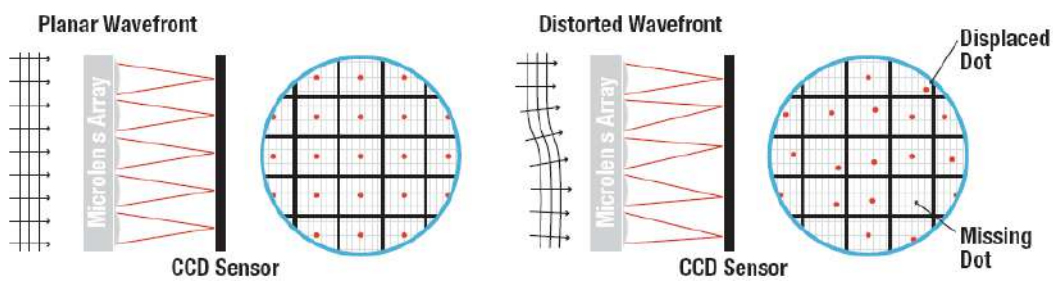

Figure 6-5: Operating principle of a Shack-Hartmann wavefront sensor: the coordinates of each dot focused in the CCD sensor are used to calculate the gradient of the wavefront at the center of each microlens. Combining the measurement from all microlenses allows reconstructing the complete surface of the wavefront. (Source: Thorlabs)

6.2.1 Parametric Fitting Method

The propagation of the laser beam through the proposed optical system can be determined using the ray tracing technique presented in Section 2.2.1. Assuming the

laser beam incident on the mirror to be perfectly collimated, its complex beam parameter q_1 is given by:

$$\frac{1}{q_1} = \frac{-i}{z_{R1}}, \tag{6.1}$$

where z_{R1} is the Rayleigh range of the collimated beam. Applying the formula 2.12, the complex beam parameter at the measurement plane of the wavefront sensor is given by:

$$\frac{1}{q_2} = \frac{C - i\frac{D}{z_{R1}}}{A - i\frac{B}{z_{R1}}} = \frac{AC + \frac{BD}{z_{R1}2} + i\left(\frac{BC-AD}{z_{R1}}\right)}{A^2 + \frac{B^2}{z_{R1}^2}}, \tag{6.2}$$

where A, B, C and D are the four terms of the ABCD matrix representing the optical system composed by the varifocal mirror and the free space propagation between the mirror and the wavefront sensor. Therefore, the radius of curvature measured by the wavefront sensor is

$$\kappa = \frac{1}{RoC} = \frac{AC + BDL}{A^2 + B^2 L}, \tag{6.3}$$

where $L = 1/z_{R1}^2$. It is usually more convenient to express the wavefront sensor measurement in terms of the curvature $\kappa = 1/RoC$, since the RoC variable often results in values close to ∞. Representing the varifocal mirror as a thin lens with focal length $f_M = 1/P_M$, the ABCD matrix of the system can be obtained by the 2.14:

$$M_{system} = \begin{pmatrix} A & B \\ C & D \end{pmatrix} = \begin{pmatrix} 1 - d_W P_M & d_W \\ -P_M & 1 \end{pmatrix} \tag{6.4}$$

This representation can be used without loss of generality, since the only difference between a thin lens and a curved mirror in terms of ray tracing is the change in direction of the beam axis. Replacing the ABCD terms into the 6.3, we obtain:

$$\kappa(P_M) = \frac{1}{RoC(P_M)} = \frac{d_W P_M^2 - P_M + d_W L}{d_W^2 P_M^2 - 2 d_W P_M + \left(1 + d_W^2 L\right)}. \tag{6.5}$$

This function is the measurement model of the optical system, as it allows us to determine the radius of curvature of the measured beam as a function of the optical power of the mirror, as long as the parameters L and d_W are known. Unfortunately, this function is not monotonic (Fig. 6-6 shows this function for $d_W = 80mm$ and $z_{R1} = 0.7m$), thus it is not invertible. This means P_M cannot be obtained from a single measurement of κ. However, this function can still be used to determine the properties of the mirror deflection using a parametric approach.

First, let us define the parametric mirror deflection curve $\Delta p(P_M)$, based on the

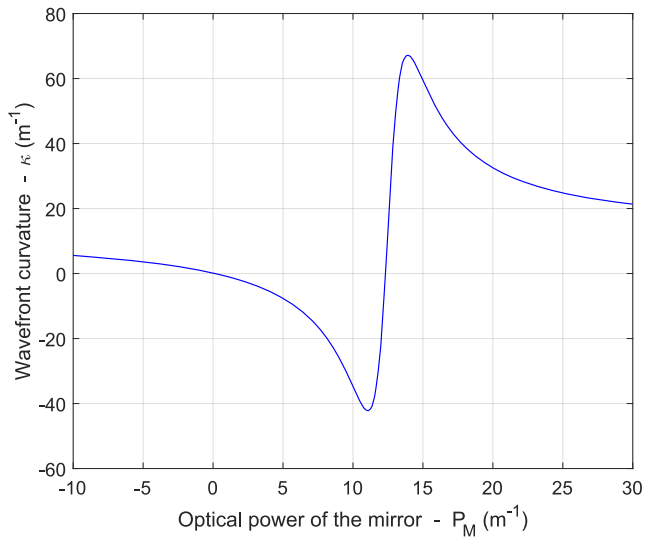

Figure 6-6: Measurement model of the wavefront sensor for the optical system shown in Fig. 6-4, using the parameters $d_W = 80$ mm and $z_{R1} = 0.7$ m.

4.77, as:

$$\Delta p = a + bP_M + cP_M^3, \tag{6.6}$$

with

$$b = \frac{h\left(\sigma_0 - \sigma_T\right)\left(1+\alpha^2\right)}{2\alpha} \tag{6.7}$$

and

$$c = \frac{hE_\nu R_y^2\left(1+\alpha^2\right)}{96\alpha}. \tag{6.8}$$

It is worth noting that in 6.6, a linear term a was added, which was not present in the 4.77. This term is used to represent the initial curvature of the mirror, caused by the thermal stress between the silicon nitride membrane and the reflective coating. As done in Section 4.1.5, the *Cardan's* formula can be used to invert the 6.6. This gives us:

$$P_M = \sqrt[3]{\frac{\Delta p - a}{2c} + \sqrt{\frac{(\Delta p - a)^2}{4c^2} + \frac{b^3}{27c^3}}} + \sqrt[3]{\frac{\Delta p - a}{2c} - \sqrt{\frac{(\Delta p - a)^2}{4c^2} + \frac{b^3}{27c^3}}}. \tag{6.9}$$

Combining the 6.5 and the 6.9, we obtain a function $\kappa(\Delta p)$, which corresponds to the measurement model of our experimental setup. Performing a parametric

fitting on the experimental data – composed by pairs $(\Delta p, \kappa)$ – we can determine the parameters of the mirror deflection curve (a, b, c) together with the parameters of the optical system (d_W, z_{R1}).

6.2.2 Far-Field Approximation Method

When the wavefront measurement is performed in the far-field of the beam, the radius of curvature becomes approximately equal to the distance to the waist location: $RoC(z) \approx -z$. The negative sign used here is simply due to the convention used by the wavefront sensor: curvature is positive for diverging beams and negative for converging ones. In this case, the focal length of the mirror f_M can be easily obtained by:

$$f_M = d_W - RoC. \tag{6.10}$$

Using this approximation, the measurement model of the optical system becomes:

$$\tilde{\kappa}(P_M) = \frac{P_M}{P_M d_W - 1}, \tag{6.11}$$

in which the symbol $\tilde{\kappa}$ is used to represent the far-field approximation of the κ. The validity of this approximation depends mainly on the beam quality factor of the collimated beam, which is encoded in the parameter z_{R1}.

Fig. 6-7 shows a numerical simulation comparing the approximation $\tilde{\kappa}(P_M)$ with the real measurement model $\kappa(P_M)$ for different values of z_{R1}. As it can be seen, when z_{R1} is large, the far-field approximation provides almost the same result as the real measurement model. The error of this approximation is only significant for a small range of values for P_M near a value P_{Mw} (in this simulation $P_{Mw} = 12.5m^{-1}$), which corresponds to the optical power of the mirror that focuses the beam exactly at the measurement plane of the wavefront sensor. As z_{R1} decreases, the error of the far-field approximation increases and the range of values of P_M for which the error is significant becomes wider. Therefore, the applicability of such approximation depends on the quality of the experimental setup.

6.2.3 Fourier Method

In order to avoid the limitations of these two methods, a third method can be used, which consists in determining the focal point of the beam directly from the analysis of the entire wavefront (not only the radius of curvature). This can be done by propagating the measured wavefront in the z direction using the Fourier transform, as proposed in [72]. This method allows calculating not only the position of the focal point, but also the associated beam waist w_0 and consequently the beam quality factor M^2.

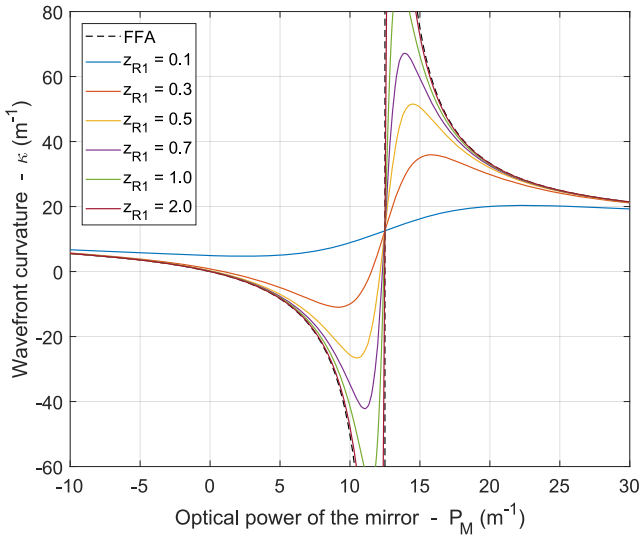

Figure 6-7: Comparison between the far-field approximation (FFA) and the real measurement model of the wavefront sensor for different values of z_{R1}.

Even though this method provides better results than the parametric fitting and the far-field approximation, it has one major limitation. Since the Fourier transform gets noisy close to the edges of the signal, it only provides accurate results if the measured beam fills less than 50% of the aperture of the wavefront sensor. This condition is difficult to be satisfied if the focal length of mirror varies through a wide range, since the diameter of the laser spot also varies a lot. In order to satisfy this condition it would be necessary to make the distance between the mirror and the measurement plane of the wavefront sensor to be shorter than 4 mm, which is physically impossible.

Another way of keeping the diameter of the beam on the wavefront sensor constant is to use a 4-f system, such as proposed in [73]. This system uses two lenses between the mirror and the wavefront sensor, causing the measurement plane of the wavefront sensor to be conjugate with the central plane of the mirror. The only requirement of this method is a precise alignment between the mirror, the two lenses and the wavefront sensor. We tried implementing this solution, however we observed tip and tilt associated with the deflection of our mirror, which resulted in significant misalignment of the beam. This problem is explained in detail in Section 6.3.5. Because of this problem, we were not able to use this approach.

Given these limitations of our system, we decided to use the parametric fitting as our main method for characterizing the deflection curve of the varifocal mirror. We also used the far-field approximation to help analyzing the $P_M(\Delta p)$ curve, however the error associated with it was significant for a wide range of P_M values. We discuss the implications of that on the obtained results in section 6.3.3.

6.3 Static Characterization

The goal of the static characterization is to analyze how the central deflection of the mirror and the induced optical aberrations change with the applied pressure. The analysis of the central deflection allows us to measure the optical power range of the mirror, as well as the precision of the deflection model presented in Section 4.1. The analysis of the optical aberrations allows us to quantify how close the mirror deflection is to a perfect paraboloid and how efficiently the mirror is able to focus the laser spot. This is important to determine the pressure range for which the optical quality of the mirror is considered good, which effectively defines the focal length range for which the mirror can provide precise focusing.

6.3.1 Experimental Setup

Fig. 6-8 shows the complete experimental setup used for the static characterization of the fabricated varifocal mirror. The mirror was inserted in the mirror holder, which was attached to a 3D-printed system support. The system support was fixed to an optical breadboard to provide stability for the measurement system. The support also contains an attachment for the optical fiber and the collimating lens, allowing us to easily align the collimated beam to the varifocal mirror at an angle of 45°.

The light beam used in these experiments was a 10 mW fiber-coupled LED, delivered through a 200 µm multi-mode optical fiber (Thorlabs, USA). The distance between the fiber tip and the collimating lens was adjusted manually, until collimation was achieved. In order to limit the laser beam to the diameter of the mirror, a 2 mm circular aperture was placed after the collimating lens.

The wavefront sensor WFS150-5C (Thorlabs, USA) was placed in front of the varifocal mirror, at an angle of 45°. The distance between the wavefront sensor and the system support was fixed, resulting in $d_W = 83.66$ mm. The hydraulic actuation system – composed by the microinjection system, the pressure sensor and the Arduino microcontroller – was placed next to the optical breadboard.

6.3.2 Experimental Procedure

The first step of the experiment consisted in the alignment of the collimated beam and the calibration of the wavefront sensor. For this step, the varifocal mirror was replaced by a flat gold mirror. After that, the position of the collimating lens was adjusted until the reflected beam measured by the wavefront sensor was as close as possible to a collimated beam. When this was achieved, the reflected beam was calibrated as a reference for the wavefront sensor. This operation allows removing the original optical aberrations of the beam and the collimating system from the measurements performed with the varifocal mirror.

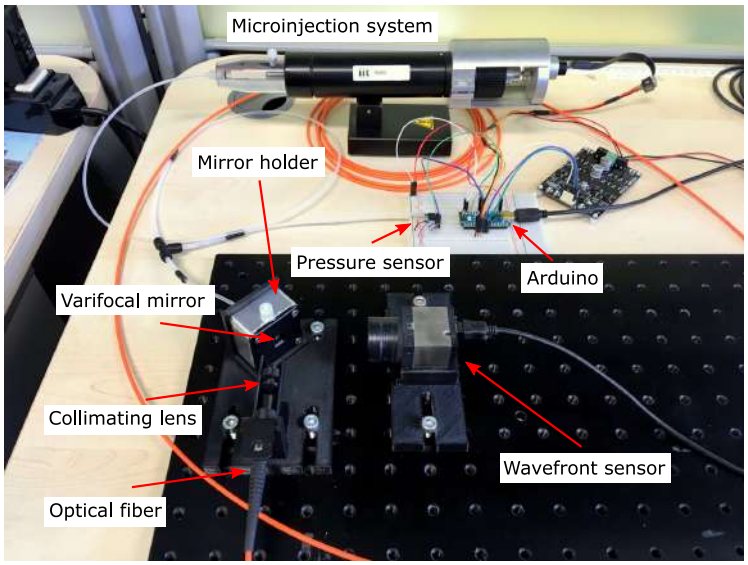

Figure 6-8: Experimental setup used in the static characterization of the varifocal mirror.

The second step of the experiment was the calibration of the pressure sensor. Since there is a height difference between the pressure sensor and the fluidic chamber of the mirror, the measured pressure contains an offset in respect to the pressure applied to the mirror – corresponding to the hydrostatic pressure of the oil. To determine this offset, the varifocal mirror was inserted in the mirror holder without the oil and its initial curvature was measured with the wavefront sensor. Then, after the fluidic chamber was filled with oil, the actuation pressure was adjusted until the initial curvature of the mirror was obtained. The obtained pressure offset was 300 Pa.

Once the calibration parameters were obtained, the static characterization was performed automatically by a routine implemented in Matlab. In this routine, the target pressure of the hydraulic system was changed every 2 s at steps of 50 Pa. The measurements of the reflected wavefront were performed at every 250 ms, but the measurements were interrupted for 1 s every time the target pressure was changed. This was done to ensure the settling of the membrane, since in this experiment we were not interested in capturing the dynamic behavior of the mirror. This resulted in 4 measurements per target pressure value. The profile of the target pressures was the following: it started at 0; then it was decreased until -5 kPa (maximum convex deflection of the mirror); then it was increased until 5 kPa (maximum concave deflection of the mirror); and finally it was decreased again until 0. This profile was chosen to examine the presence of hysteresis.

6.3.3 Obtained Results

Fig. 6-9 shows the obtained results of the static characterization, performed with an elliptical mirror with a diameter of 3 x 4.24 mm. The wavefront sensor measurements are expressed in terms of $\kappa = 1/R_{oC}$. The fitted curve was obtained by performing a parametric fitting on the experimental results using the model described by equations 6.5 and 6.9. The obtained values for the parameters are shown in Table 6.1.

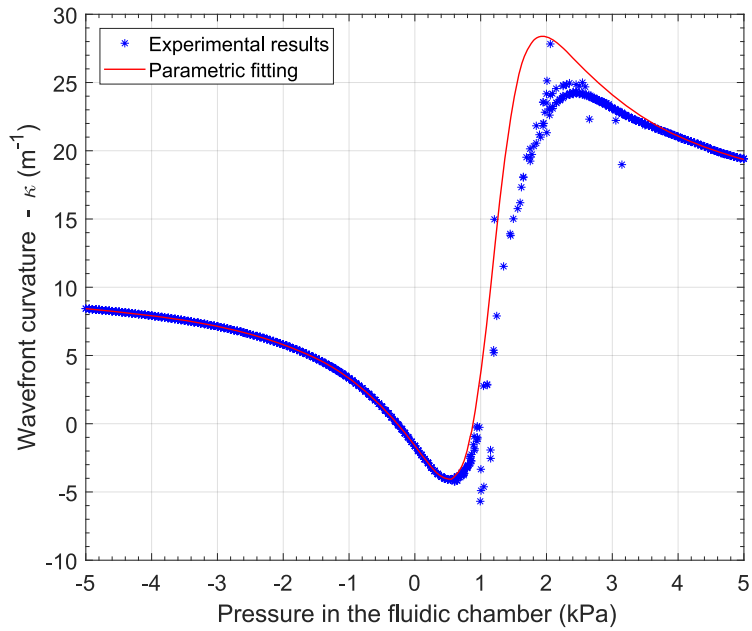

Figure 6-9: Static characterization of the elliptical varifocal mirror.

Table 6.1: Parametric fitting of the experimental results of the static characterization

Parameter	Fitted value
a	-551.5
b	138.4
c	0.03694
L	20.7
d_W	0.08222

The root mean square error (RMSE) between the κ measurements and the fitted curve is 1.512 m^{-1}. As it can be seen, there is good agreement between the experimental results and the parametric fitting, except for the pressure range between approximately 1 and 3 kPa. In this range, not only the measurements diverge from the parametric model, but they also exhibit more noise. This is because for this

pressure range the focal point of the beam is close to the measurement plane of the wavefront sensor, as it can be seen in Fig. 6-10.

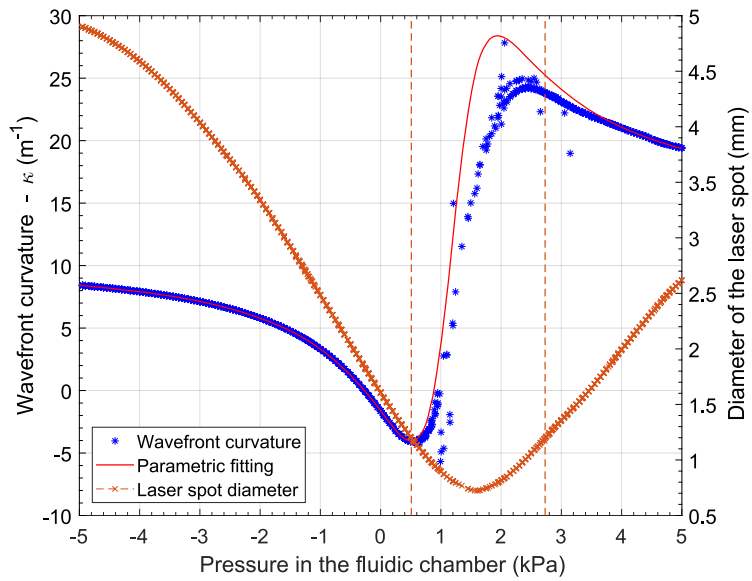

Figure 6-10: Diameter of the measured laser spot shown alongside the results of the static characterization. The left Y axis refers to the curvature and parametric fitting while the right Y axis refers to the laser spot diameter.

Fig. 6-10 shows the results of the static characterization alongside the values of laser spot diameter measured by the wavefront sensor. It is worth noting that this graph contains two Y axis, where the left one refers to the wavefront curvature and the parametric fitting and the right one refers to the laser spot diameter. As it can be seen, when the laser spot diameter is small, the noise in the wavefront sensor measurements increases and the experimental data diverges from the parametric model. This is because the diameter of the laser spot determines how many microlenses of the wavefront sensor are irradiated by the laser. When too few microlenses are irradiated, the wavefront sensor does not obtain enough data points to reconstruct the wavefront precisely. This means, that the reliability of the wavefront sensor measurements decrease when the laser spot is too small. This effect is more significant for the pressure range between 0.535 and 2.733 kPa, when the laser spot diameter is lower than 1.2 mm. From now on, we will refer to this pressure interval as $[\Delta p_{inv}]$.

To better understand the results of the static characterization, we may also analyze the graph for the radius of curvature *RoC*, shown in Fig. 6-11. The data shown here (both the experimental results and the fitted curve) were obtained simply by making $RoC = 1/\kappa$. From this curve, we can more easily identify how the focal point of the beam shifts with the mirror's deflection.

- For pressures between -5 and 0.551 kPa, the mirror deflection is convex and the reflected beam is divergent ($RoC > 0$).

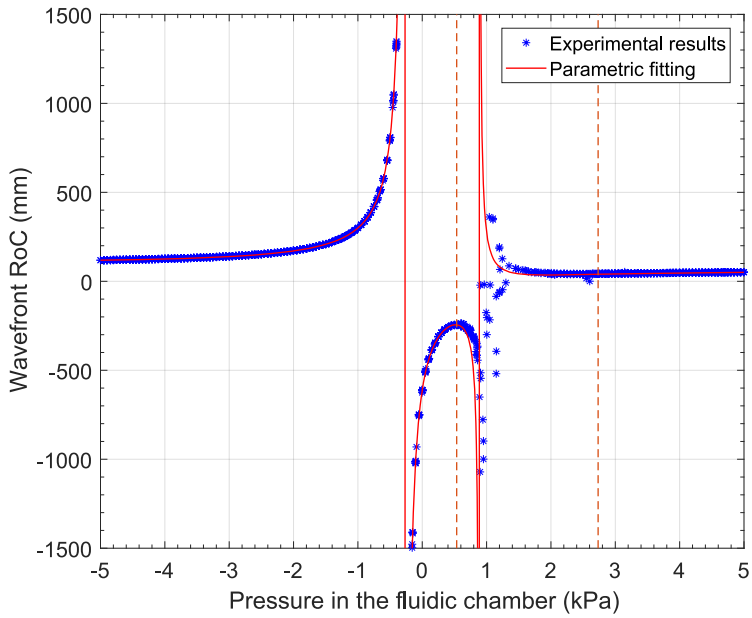

Figure 6-11: Radius of curvature $RoC = 1/\kappa$ measured by the wavefront sensor during the static characterization.

- For $\Delta p = -0.551$ kPa, the reflected beam is collimated, which is why RoC goes to ∞.
- For pressures between -0.551 and 1.198 kPa, the focal point of the beam is behind the wavefront sensor, so the measured beam is convergent ($RoC < 0$).
- For $\Delta p = 1.198$ kPa, the focal point of the beam is exactly at the measurement plane of the wavefront sensor. At this point, the measured wavefront is flat, which is why RoC goes back to $-\infty$ and then to ∞.
- For pressures between 1.198 and 5 kPa, the focal point of the beam is between the mirror and the wavefront sensor, which is why the measured beam is divergent again ($RoC > 0$).

In this curve we can also see an excellent agreement between the experimental results and the parametric fitting. The only data points that deviate from the parametric model are within the $[\Delta p_{inv}]$ interval, especially close to the pressure point $\Delta p = 1.198$ kPa.

Having said that, we should focus our analysis on the measurements obtained outside of the $[\Delta p_{inv}]$ interval. In fact, it can be seen from Fig. 6-10 that the obtained curve $\kappa(\Delta p)$ is monotonic for both the pressure intervals $\Delta p < [\Delta p_{inv}]$ and $\Delta p > [\Delta p_{inv}]$. Therefore, it is possible to invert these segments of the curve numerically to reconstruct part of the mirror deflection curve $P_M(\Delta p)$, as shown in Fig. 6-12. In this figure, the measurement model data points were obtained by plugging the

measurements κ into the numerical inversion of the segments of the measurement model given by 6.5. The fitted deflection curve was obtained using the 6.6 with the values for a, b and c indicated in Table 6.1.

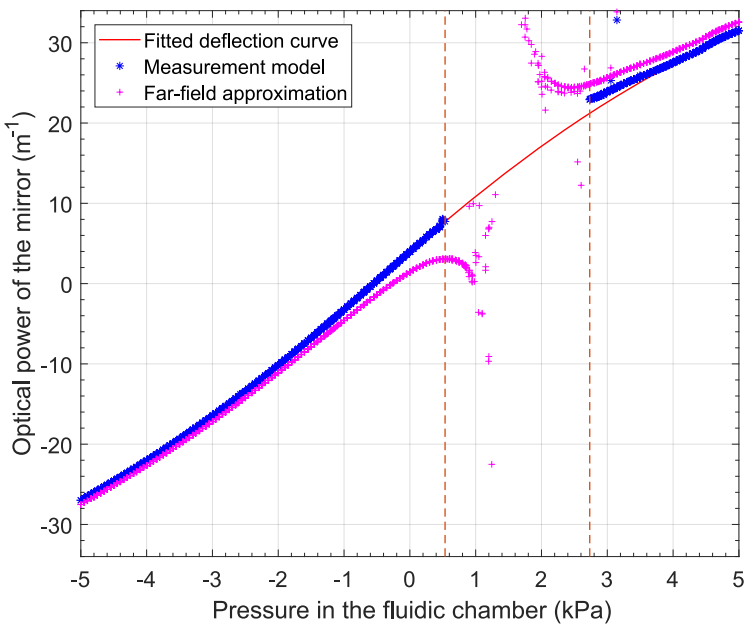

Figure 6-12: Deflection curve of the varifocal mirror calculated from the results of the static characterization.

As it can be seen, the optical power of the mirror can be well determined by the mirror deflection model, at least for pressure values outside of the $[\Delta p_{inv}]$ interval. The RMSE between these segments of the reconstructed $P_M(\Delta p)$ and the fitted deflection curve is 0.480 m^{-1}. This graph also shows the $\tilde{P_M}(\Delta p)$ obtained by the far-field approximation, given by 6.11. As expected, the results obtained with the far-field approximation are not valid when the focal spot is close to the measurement plane of the wavefront sensor. However, even outside the $[\Delta p_{inv}]$ interval, we can see that the results obtained with the far-field approximation still show significant deviation from the obtained parametric fitting. This can be explained due to the low quality of the collimated beam. As shown in Table 6.1, the obtained value for the parameter L was 20.7, which corresponds to $z_{R1} = 0.2198$ m. As shown in Fig. 6-7 this value of z_{R1} is relatively low, causing the far-field approximation to provide significant error over a wide range of pressure values. The main reason for that is the fact that the light source used in this experiment was a fiber-coupled LED, which is not a laser beam.

Experiment with Prefocusing Lens

In order to better understand the behavior of the mirror within the pressure interval $[\Delta p_{inv}]$, we repeated the static characterization experiment with the same procedure, but inserting a prefocusing lens (a plano-convex lens with focal length of 40 mm) between the mirror and the wavefront sensor. The distance between the mirror and the prefocusing lens was 20 mm. Because of that, the range of pressures that causes the focal point to be close to the wavefront sensor is shifted, allowing us to reconstruct another segment of the $P_M(\Delta p)$ curve. Fig. 6-13 shows the results obtained in this second experiment. Analogously to the Fig. 6-10, this graph shows the laser spot diameter measured by the wavefront sensor alongside the obtained wavefront curvature. In this case, the pressure range that results in a laser spot diameter lower than 1.2 mm is between -3.950 and -0.545 kPa, which we will denote as $[\Delta p_{inv2}]$.

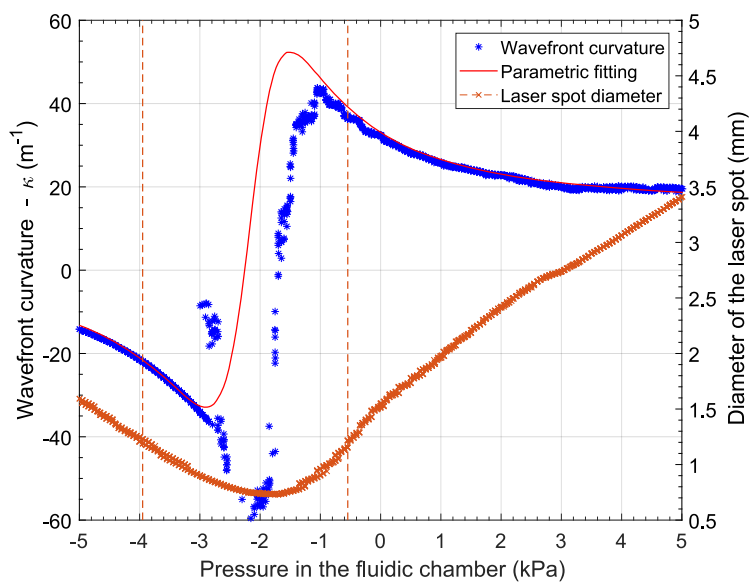

Figure 6-13: Static characterization of the elliptical mirror performed with a prefocusing lens between the mirror and the wavefront sensor.

The parametric fitting shown in Fig. 6-13 was obtained with the method described in Section 6.2.1, however with a different expression for $\kappa(P_M)$, since the inclusion of the prefocusing lens modifies the measurement model that represents the optical system. The complete ABCD matrix representing the mirror, the prefocusing lens and the beam propagation until the wavefront sensor is given by:

$$M_{system2} = \begin{pmatrix} A & B \\ C & D \end{pmatrix} = \begin{pmatrix} (1-d_W P_L)(1-d_L P_M) - d_W P_M & (1-d_W P_L)\, d_L + d_W \\ -P_M - P_L(1-d_L P_M) & 1-d_L P_L \end{pmatrix}, \tag{6.12}$$

where $P_L = 1/f_L$ is the optical power of the prefocusing lens, d_L is the distance

between the prefocusing lens and the mirror and d_W is the distance between the prefocusing lens and the measurement plane of the wavefront sensor. Therefore, the expression for $\kappa(P_M)$ used in the parametric fitting of Fig. 6-13 is obtained by replacing the A, B, C and D terms of the 6.12 into the 6.3. It is worth noting that if $f_L = d_L$, the 6.12 reduces to:

$$M_{system3} = \begin{pmatrix} A & B \\ C & D \end{pmatrix} = \begin{pmatrix} P_L - P_M - d_W P_L^2 & 1 \\ -P_L^2 & 0 \end{pmatrix} \tag{6.13}$$

However, since this condition was not satisfied in this experiment, we used the 6.12. The results shown in Fig. 6-13 are significantly more noisy than the ones obtained without the prefocusing lens, since the RMSE between the κ measurements and the parametric fitting is 21.50 m^{-1}. This is associated with two factors. The first one is the large deviation between the measurements and the parametric model within the $[\Delta p_{inv2}]$ interval. The second one is the larger variance of the data, especially for pressure values above 4 kPa. The later is most likely caused by misalignments between the mirror and the prefocusing lens. Even though the optical system was aligned before the experiment, we observed a small tilt of the varifocal mirror associated with the mirror deflection, which we better explain in Section 6.3.5. Because of this effect, the alignment can be lost as the mirror deflects, degrading the quality of the focused laser spot.

Excluding the pressure interval $[\Delta p_{inv2}]$ from the obtained results, we are able invert the two remaining segments of the $\kappa(\Delta p)$ in order to reconstruct another part of the deflection curve $P_M(\Delta p)$, as shown in Fig. 6-14. In this figure we show the results obtained in both experiments – with and without the prefocusing lens. As expected, the curve obtained with the prefocusing lens gets very noisy for high pressure values. The most important conclusion we can draw from this graph is that the qualitative behavior of the curve $P_M(\Delta p)$ does not change significantly within the $[\Delta p_{inv}]$ interval. Even though the results obtained with the prefocusing lens are noisy, it is clearly seen that the curve is smooth within the $[\Delta p_{inv}]$ interval, without any discontinuities or artifacts. This lets us conclude that the curve $P_M(\Delta p)$ obtained without the prefocusing lens is a good representation of the mirror behavior.

Coefficients of the Parametric Fitting

The values obtained for the coefficients of the parametric fitting shown in Table 6.1 can be analyzed to draw additional conclusions about the characterized varifocal mirror and the experimental setup.

The coefficient a represents the initial curvature of the mirror, caused by the thermal stress between the membrane and the reflective coating. The obtained value for a corresponds to an initial optical power of the mirror of 3.97 m^{-1}. This means that the focal length of the mirror without actuation is 251.89 mm.

From the linear coefficient b, we can determine the residual stress σ_0 of the mir-

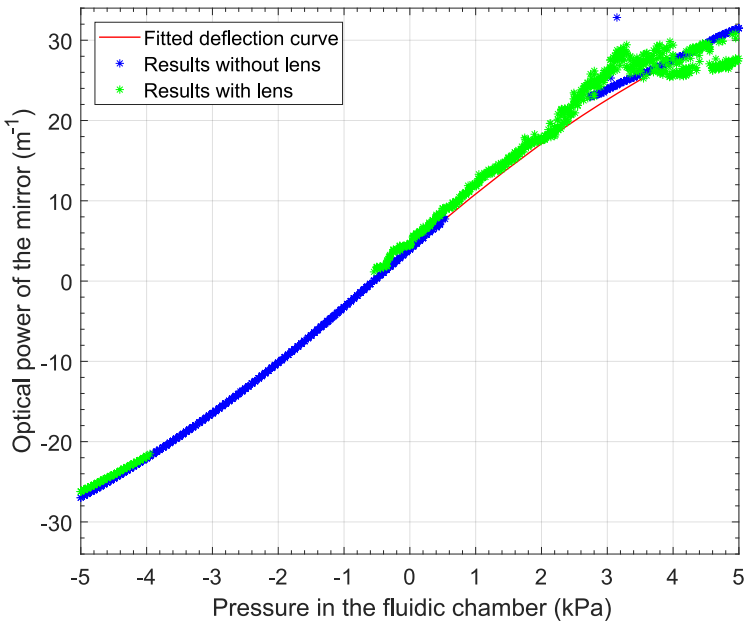

Figure 6-14: Deflection curve of the varifocal mirror obtained from 2 datasets: with and without the prefocusing lens.

ror, as given by 6.7. Assuming the thermal stress σ_T to be 0 (since this experiment is performed with the low-power laser), the residual stress can be calculated as:

$$\sigma_0 = \frac{2\alpha b}{h(1+\alpha^2)}. \tag{6.14}$$

Using the obtained value for b and the parameters of the mirror ($\alpha = \sqrt{2}$ and $h = 500\,\text{nm}$), we obtain $\sigma_0 = 261\,\text{MPa}$. This value is consistent with typical values of residual stress of silicon nitride membranes reported in the literature [74].

The coefficient c is completely defined by the properties of the mirror and does not contain any free parameter. This means we can compare the obtained value for c with the 6.8 in order to validate the obtained result. Using the parameters of the mirror, we can calculate the expected value of c as $c_{expected} = 0.03$, which is close to the obtained value for $c = 0.03694$. The $c_{expected}$ was calculated using typical values for Young's modulus and Poisson's ratio of silicon nitride, since these parameter were not identified for our specific membranes.

The obtained value for the parameter L corresponds to a Rayleigh range of the collimated beam of $z_{R1} = 0.2198$ m. If we compare this value with the expression 2.8 for z_{R1}, we are able estimate the beam quality factor of our light source. Using the obtained value for z_{R1} and the parameters of the collimated beam ($\lambda = 470\,\text{nm}$ and $w_1 = 1.5\,\text{mm}$), we obtain $M^2 = 68$. This corresponds to a very low optical quality, which means that the light beam used in the experiment is far from a Gaussian beam.

Finally, the parameter d_W corresponds to the distance between the measurement plane of the wavefront sensor and the center of the varifocal mirror. This parameter was measured before the experiment as $d_W = 83.66$ mm, however the value for d_W obtained with the parametric fitting was 82.22 mm. This difference is acceptable and can be considered within the error margin of the manual measurement of d_W.

6.3.4 Corresponding Focal Length Range

Analyzing the deflection curve $P_M(\Delta p)$ of Fig. 6-12, we can see that the optical power of the mirror changes from -26.73 to 31.50 m^{-1} for a pressure range from -5 to 5 kPa, resulting in an optical power range ΔP_M of almost 60 m^{-1}. This maximum optical power corresponds to a concave deflection with focal length of 31.75 mm, while the maximum convex deflection corresponds to a focal length of -37.41 mm. This means that the varifocal mirror alone can shift the focal point of the laser from ∞ to 31.75 mm and from $-\infty$ to -37.41 mm. However, when a prefocusing lens is used, the focal length range of the system depends also on the optical power of the prefocusing lens.

Assuming the distance between the mirror and the prefocusing lens d_L to be equal to the focal length of the prefocusing lens f_L, the combined length f_{sys} of the system composed by the mirror and the prefocusing lens is given by the 4.68. Considering the focal length range required by the clinical application to be $\{f_{min}, f_{max}\}$, our proposed focusing system must be able to achieve:

$$f_L - max\,(P_M)\,f_L^2 \leq f_{min} \tag{6.15a}$$

$$f_L - min\,(P_M)\,f_L^2 \geq f_{max} \tag{6.15b}$$

From this expression, we can see that if the maximum deflection of the mirror is symmetric, such that $max(P_M) = -min(P_M) = Q$, the required optical power of the mirror for satisfying the application requirements is given by:

$$Q \geq \frac{f_{max} - f_L}{f_L^2} \tag{6.16a}$$

$$Q \geq \frac{f_L - f_{min}}{f_L^2} \tag{6.16b}$$

This means that having a mirror with high optical power range allows us to use a prefocusing lens with shorter focal length, which helps reducing the overall size of the focusing system. For example, considering $f_L = d_L = 25$ mm, the corresponding optical length of the system f_{sys} becomes as illustrated in Fig. 6-15. The results showed here were calculated from the data of the Fig. 6-12, using the equation 4.68. As it can be seen, in this optical configuration, the optical power range provided by

the mirror is able to shift the focal point of the system from 5.32 to 41.88 mm. This focal length range can be considered good enough for a clinical application such as endoscopic phonomicrosurgery as it covers a significant part of the anatomical depth variation observed in the vocal cords.

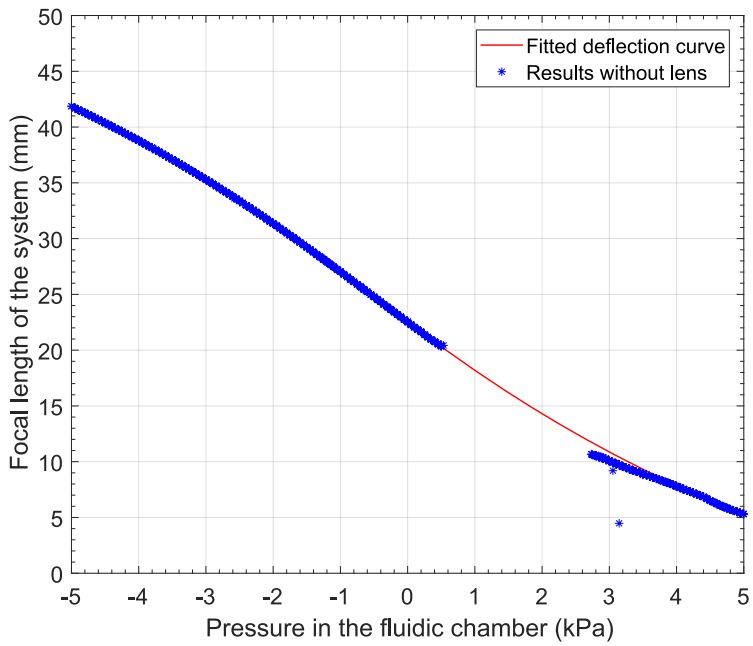

Figure 6-15: Corresponding focal length f_{sys} of an optical system composed by the varifocal mirror and a prefocusing lens with f_L = 25 mm. This result is calculated based on the reconstructed deflection curve $P_M(\Delta p)$ of Fig. 6-12.

The RMSE calculated between the two segments of the obtained $f_{sys}(\Delta p)$ curve and the deflection model of the mirror is 0.432 mm. Assuming the mirror to be controlled in open-loop based on the fitted deflection curve, the expected focusing error f_e obtained is shown in Fig. 6-16. As it can be seen, the error is negligible for the negative pressures, which means the mirror deflection in the convex direction can be controlled with high precision. In the concave direction, the mirror deflection deviates from the model, but ignoring the $[\Delta p_{inv}]$ interval the maximum obtained error is expected to be -1.10 mm.

To understand the impact of this focusing error on the precision of the laser focusing, we can calculate the corresponding error in the laser spot diameter. This can be obtained by the 4.65. If we define w_e as the ratio between the obtained laser spot diameter and the target spot diameter $2w_t$, we can see that:

$$w_e = \sqrt{1 + \left(\frac{f_e}{z_R}\right)^2}, \tag{6.17}$$

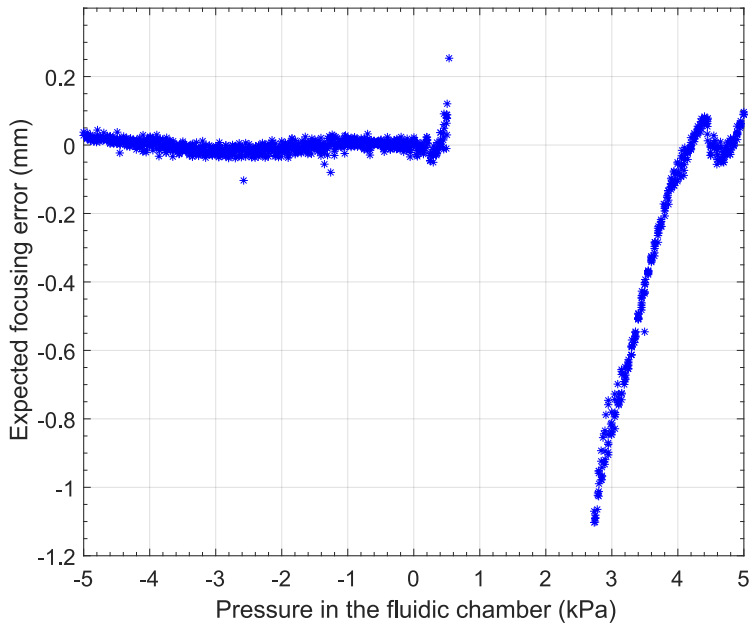

Figure 6-16: Expected focusing error in a system with a prefocusing lens with f_L = 25 mm, caused by the difference between the mirror deflection curve and the obtained experimental results.

where

$$z_R = \frac{\pi}{M^2\lambda} w_t^2. \tag{6.18}$$

Fig. 6-17 shows a simulation of w_e as a function of the focusing error, assuming the parameters of a TEM_{00} CO_2 laser beam ($M2 = 1$ and $\lambda = 10.6\,\mu m$). As we can see, the smaller is the target spot diameter, the greater is the impact of the focusing error. For a target spot of 200 µm, a focusing error of 1.1 mm produces a variation in the laser spot diameter of 6.67%. For a target spot of 300 µm, this corresponding variation is only 1.35%. This result can be considered good since current CO_2 fibers typically provide laser spots of diameter of 300 µm or higher.

6.3.5 Optical Quality

The optical quality of the deflected varifocal mirror was analyzed by the Zernike coefficients measured by the wavefront sensor. Figs. 6-18, 6-19 and 6-20 show the measured Zernike coefficients as a function of the pressure applied to the mirror. This data was acquired during the static characterization without the prefocusing lens.

The largest aberrations observed, where optical tip and tilt, represent by the Zernike coefficients Z2 and Z3 respectively. Fig. 6-18 shows the evolution of these

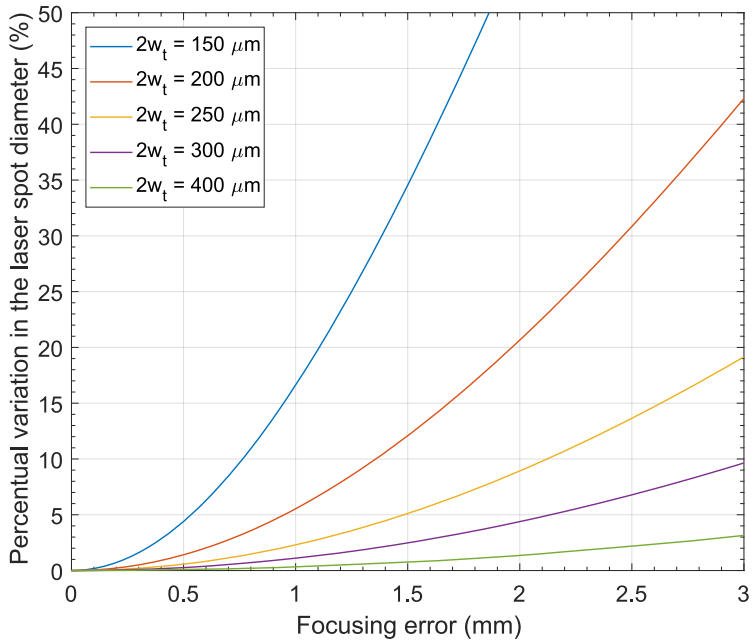

Figure 6-17: Relationship between the focusing error and the corresponding variation in the laser spot diameter, as a function of the target spot diameter $2w_t$.

aberrations with the applied pressure. As it can be seen, the coefficient for the tip in the vertical direction exhibits more than 56 µm of variation, ranging from 31 to −25 µm. This corresponds to an angular motion of the reflected beam of 0.72°. The coefficient for the tilt in the horizontal direction shows a lower variation of 10.6 µm, corresponding to an angular motion of 0.14°.

Even if the angular displacements associated with these aberrations are not very large, they have a negative impact in the focusing performance if the distance from the mirror to the target is large or if other optical elements are placed after the mirror. In the performed experiments, these aberrations were enough to hinder the static characterization of the mirror when the prefocusing lens was placed in front of it. We believe these aberrations to be caused by motion of the varifocal mirror inside the mirror holder. To eliminate this problem, we expect to improve the design of the mirror holder, adding O-rings between the mirror holder, the varifocal mirror and the cover part.

After the tip and tilt, the largest measured aberration was the vertical astigmatism, represented by the Zernike coefficient Z6, shown in Fig. 6-19. The induced vertical astigmatism makes the focal spot of the beam slightly elliptical, which degrades the efficiency of the laser focusing. The total variation of the coefficient Z6 was 1.1 µm. This value is considered significant when compared to other varifocal mirrors [53], which exhibit aberrations in the order of 200 nm.

Vertical astigmatism is typically induced when the laser beam is not aligned with the optical axis of the mirror being used [75]. In the case of an off-axis mirror,

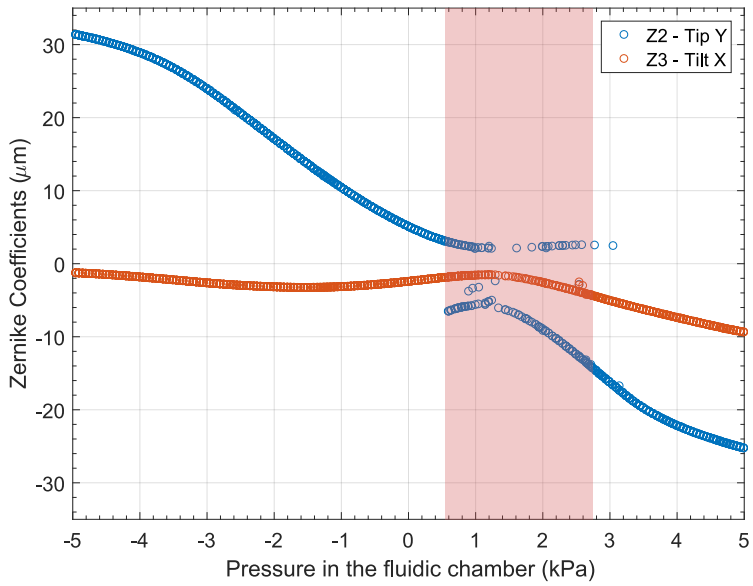

Figure 6-18: Aberrations Tip Y (Z2) and Tilt X (Z3) induced by the varifocal mirror. Area in red indicates the pressure interval $[\Delta p_{inv}]$ for which the focal point of the beam is close to the measurement plane of the wavefront sensor.

this happens if the angle of incidence of the collimated beam deviates from the intended angle of operation of the mirror, which is determined by the mirror's aspect ratio. Based on that, we believe two phenomena may be contributing to the obtained variation in Z6. The first one is a real misalignment of the collimated beam caused by the tilt of the mirror. The second one is a distortion of the mirror deflection from the elliptical paraboloid caused by errors in the shape of the mirror's boundary. In Section 5.4.1, we saw that the process of releasing the membrane with wet etching causes small distortions on the shape of the membrane boundary.

Finally, the other optical aberrations are shown in Fig. 6-20. As it can be seen, all other Zernike coefficients vary within -100 and 100 nm, including the spherical aberration (Z13). Overall, these aberrations can be considered negligible, however it is worth noting that the aberrations for the concave deflection are larger than the ones for convex deflections. This result was also observed in static characterization with the prefocusing lens (shown in Fig. 6-13), where the concave deflections exhibited larger variance than the convex deflections. Until now, we were not able to determine the reason for this asymmetric behavior.

6.4 Focusing Demo in Fluorescent Medium

In order to verify the results obtained in the static characterization, we performed a focusing demo by passing the focused laser beam through a fluorescent medium. In

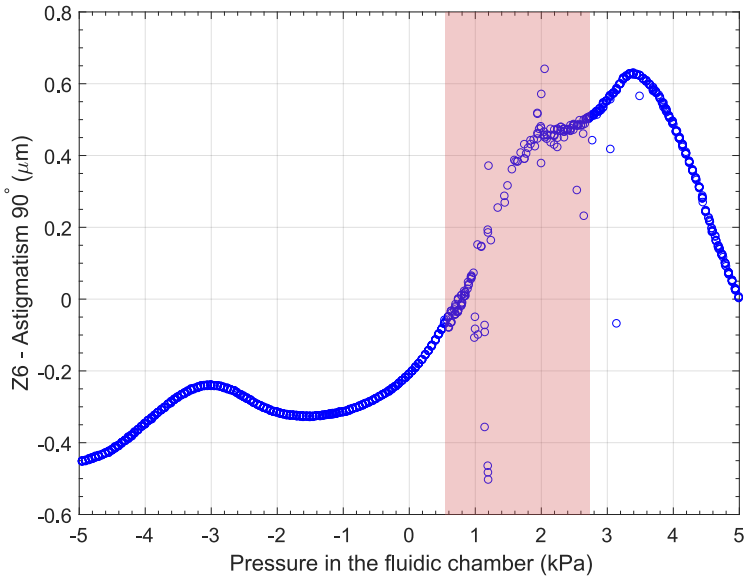

Figure 6-19: Vertical astigmatism (Z6) induced by the varifocal mirror. Area in red indicates the pressure interval $[\Delta p_{inv}]$ for which the focal point of the beam is close to the measurement plane of the wavefront sensor.

this experiment, we placed a long cuvette in front of the varifocal mirror containing a solution of fluorescein in water. We irradiated the mirror with the same fiber-

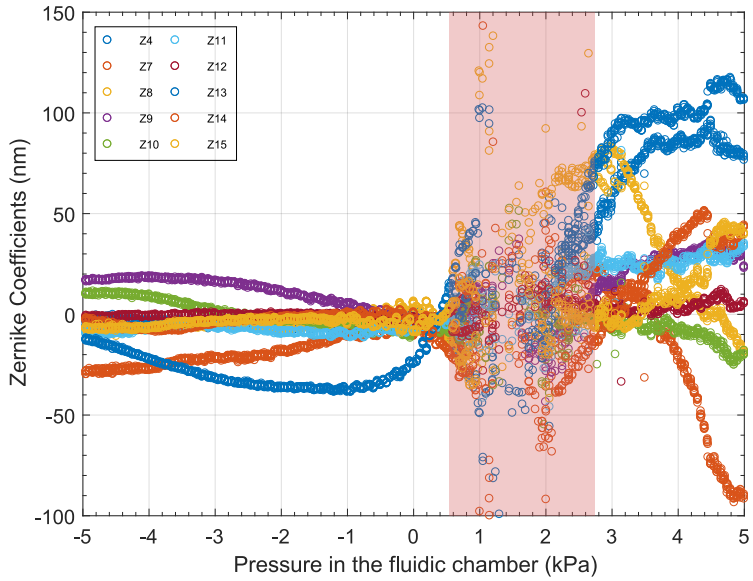

Figure 6-20: Other optical aberrations induced by the varifocal mirror. Area in red indicates the pressure interval $[\Delta p_{inv}]$ for which the focal point of the beam is close to the measurement plane of the wavefront sensor.

coupled LED as before, such that the reflected beam passed through the cuvette, allowing us to visualize the propagation of the beam inside the fluorescent medium. We took pictures of the beam for pressure levels from 0.8 to 5.3 kPa.

Fig. 6-21 shows three of those pictures. As it can be seen, the focal length of the beam decreases with the pressure applied to the mirror. For example, in the case of p = 4.8 kPa – which is close to the maximum concave deflection of the mirror – the focal point of the beam is close to the wall of the cuvette, causing the beam to strongly diverge at the end of the cuvette. The focal point of the beam in each image (indicated by a vertical red line) was obtained using image processing in order to identify the position where the diameter of the beam was minimal.

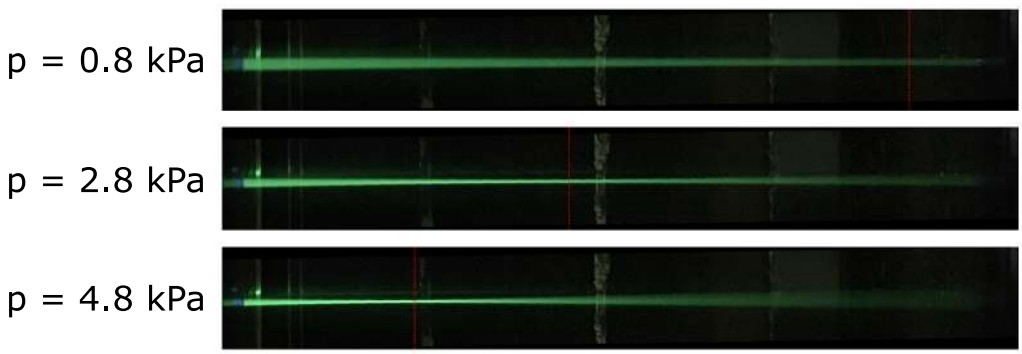

Figure 6-21: Pictures of the focused beam propagating through a fluorescent medium for different values of mirror deflection. The focal spot of the beam in each image, obtained using image processing, is indicated by a vertical red line.

In order to validate the results of the static characterization, we compared the measurements performed in the fluorescent images to the characterized mirror deflection model. However, the measured focal length of the beam in the fluorescent medium is not equal to the focal length of the mirror, since the refractive indexes of the fluorescent medium and the air are different. The conversion between the measured focal length f_w and the focal length of the mirror f_M is given by:

$$f_M = d_c + f_w \frac{n_a}{n_w} + h \frac{n_a}{n_g}, \tag{6.19}$$

where d_c is the distance between the center of the varifocal mirror and the cuvette, h is the thickness of the wall of the cuvette and n_a, n_w and n_g are the refractive indexes of air, the fluorescent medium and the cuvette material respectively. The derivation of this formula is given in the Appendix A.

The comparison between the measurements of the fluorescent images and the varifocal mirror's deflection model is shown if Fig. 6-22. As it can be seen, there is a good match between the curves for pressures over 2 kPa. For lower pressures instead, the focal length measured in the fluorescent images is shorter than the one

predicted by the deflection model. We believe this to be a measurement error associated with the fluorescent images, since for low pressure levels the numerical aperture of the focused beam becomes very small, which makes difficult to identify the focal spot of the beam with precision. This can be observed in the picture for p = 0.8 kPa, as the variation of the beam diameter around the measured focal spot is in the order of the pixel resolution of the picture.

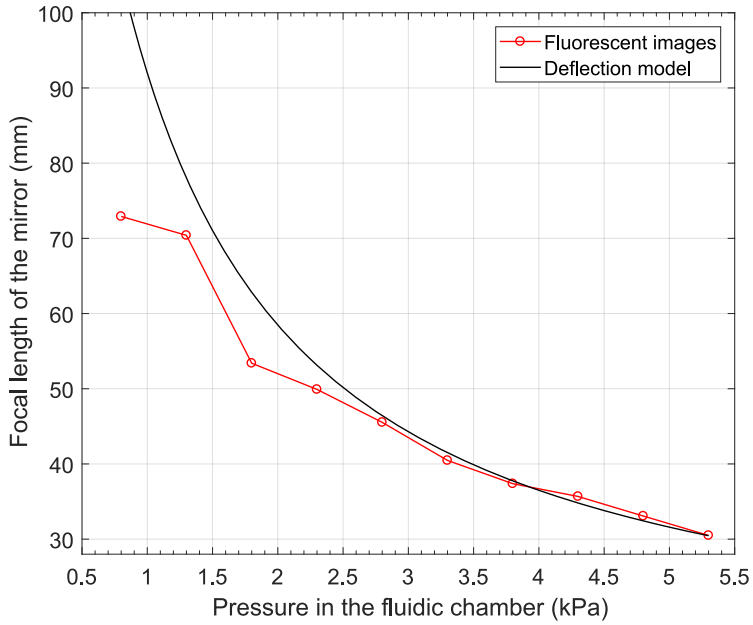

Figure 6-22: Comparison between the focal length of the mirror calculated from the fluorescent images and the mirror deflection model obtained from the static characterization.

6.5 Thermal Characterization

The goal of the thermal characterization is to analyze how the mirror behaves when irradiated by a high-power laser beam. According to the thermal deflection model (presented in Section 4.1.3), the high-power laser must induce a temperature increase in the mirror membrane, causing thermal expansion of the mirror and increasing its central deflection. Our main goal with this set of experiments is to quantify this thermal effect by comparing the mirror deflection curve with and without high-power laser irradiation.

6.5.1 Experimental Setup

To perform the thermal characterization, the mirror deflection was measured using the wavefront sensor, while the mirror was irradiated by the CO_2 laser. This means the mirror was irradiated with the CO_2 laser and the fiber-coupled LED simultaneously. However in order to prevent the CO_2 laser from damaging the wavefront sensor, the optical path of the CO_2 laser was orthogonal to the one of the fiber-coupled LED. The experimental setup used to achieve that is shown in Fig. 6-23. As it can be seen, the position of the fiber-coupled LED and the wavefront sensor were the same as in the static characterization, but a new 3D-printed system support was used. This new system support contains a connector for the CO_2 waveguide, allowing us to align it with the mirror at an angle of 45°. To prevent the reflected CO_2 beam from damaging the base of the system support, a small plaster block was placed in front of the mirror holder.

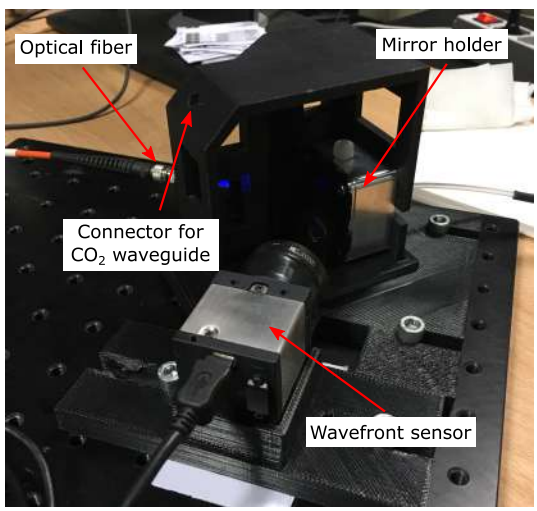

Figure 6-23: Experimental setup used in the thermal characterization of the varifocal mirror.

The laser system used in these experiments was a SmartXide2 ENT (Deka, Italy). The fiber used to deliver the CO_2 laser was a hollow waveguide (Molex, USA) with an internal diameter of 750 µm. However, since the SmartXide2 laser system does not provide a fiber-coupled output, a fiber-coupler device was used to focus the CO_2 laser into the waveguide. Initially, we used a refractive fiber-coupler from Laser Components, however it was not optimized for our CO_2 laser resource, resulting in coupling efficiency of less than 10%. This made difficult to obtain a high-power laser beam on the output of the waveguide. To solve this problem, we designed a custom reflective fiber-coupler based on an off-axis parabolic mirror.

Reflective Fiber-Coupler

Fig. 6-24 shows the design of the custom reflective fiber coupler. It is composed of an off-axis mirror – to allow focusing the CO_2 laser beam into the center of the SMA connector for the hollow waveguide – and two motion stages, providing five degrees of freedom to the system. The mirror used here had 25.4 mm of diameter, since the diameter of the collimated CO_2 beam was around 10 mm. In fact, one of the main issues of the refractive fiber-coupler from Laser Components was that the diameter of the lens was only 5 mm.

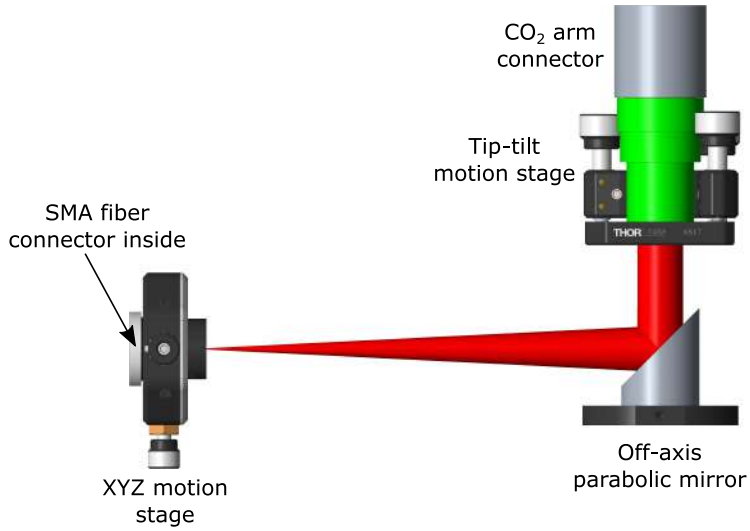

Figure 6-24: Schematic diagram of the designed reflective fiber-coupler to focus the collimated CO_2 laser beam inside the hollow-core waveguide.

The first two degrees of freedom of the fiber-coupler correspond to the tip-tilt motion stage attached to the CO_2 arm connector. These allow aligning the optical axis of the CO_2 beam to the off-axis mirror. Since the collimated CO_2 beam is reflected by many mirrors inside its articulated delivery arm, the optical axis of the beam is usually slightly misaligned with the arm connector. This misalignment, if not corrected, causes aberrations in the focused CO_2 beam, decreasing the coupling efficiency.

The remaining three degrees of freedom correspond to the XYZ motion stage, which allows us to displace the SMA fiber connector in the X, Y and Z directions. Even though the position of the SMA connector was designed to be exactly at the focal point of the off-axis mirror, assembly or fabrication errors can lead to misalignment of the connector, also decreasing the amount of energy that gets coupled into the fiber. Together these two motion stages allow calibrating the fiber-coupler on-site to maximize the coupling efficiency.

Fig. 6-25 shows a picture of the fabricated reflective fiber-coupler. We calibrated this fiber-coupler to our CO_2 laser by adjusting the two motion stages while

measuring the output power of the hollow waveguide with a power sensor. At the optimal position, we were able to achieve a coupling efficiency over 50%. Given, the fact that the attenuation at the waveguide is 1 dB. the estimated energy loss in our custom fiber-coupler was around 44%.

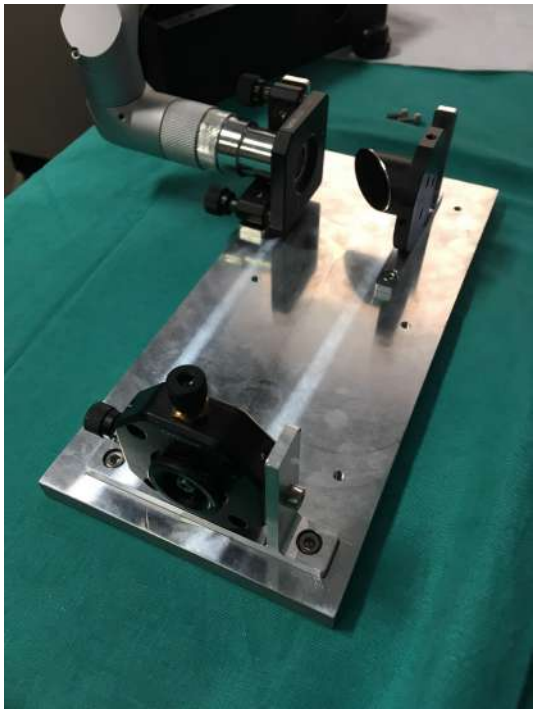

Figure 6-25: Fabricated fiber-coupler attached to the delivery arm of the Deka laser system.

6.5.2 Experimental Procedure

The experimental procedure used here was similar to the one of the static characterization – i.e. the deflection of the mirror was measured with the wavefront sensor for pressure levels in the range -5 to 5 kPa. The difference here was that the CO_2 laser was used to heat the mirror, changing the obtained deflection. Since the CO_2 cannot be kept on for the entire duration of the experiment (several minutes), the CO_2 was turned on and off for each target pressure. In fact, this allowed us to measure the static deflection of the mirror with and without the CO_2 irradiation in a single experiment.

The exact procedure to achieve that was the following. The implemented Matlab routine set the target pressure of the hydraulic actuation system. After 1s of settling delay, the system acquired ten measurements using the wavefront sensor without CO_2 irradiation. Then the CO_2 laser was turned on for approximately 3s,

allowing us to acquire ten deflection measurements with the mirror heated. After that, the CO_2 was turned off and the value of target pressure was changed. Since the activation of the CO_2 laser is made with an activation pedal (for safety reasons), this routine could not be performed entirely autonomously. Instead, command messages were added to the user interface telling the user when to turn the CO_2 on and off.

The profile of the target pressures used here was the same of the one used for the static characterization ($0 \rightarrow -5 \rightarrow 5 \rightarrow 0$). This was done to test for hysteresis, but also to verify if the CO_2 irradiation changes the properties of the mirror. Since each target pressure is used twice during the experiment (except for the limits p = -5 kPa and p = 5 kPa), a permanent change to the mirror properties can be identified by a discrepancy in both measurements for the same target pressure. Since this experiment is slower than the static characterization (as it requires intervention of the user), the pressure was changed at steps of 250 Pa (instead of 50 Pa, as done before).

6.5.3 Obtained Results

Fig. 6-26 shows the obtained results of the thermal characterization. This figure shows both the κ measurements with the CO_2 laser on and off. The power of the CO_2 laser was set to 7.5W and the coupling efficiency obtained was 40%, resulting in an output power at the hollow waveguide of 3W.

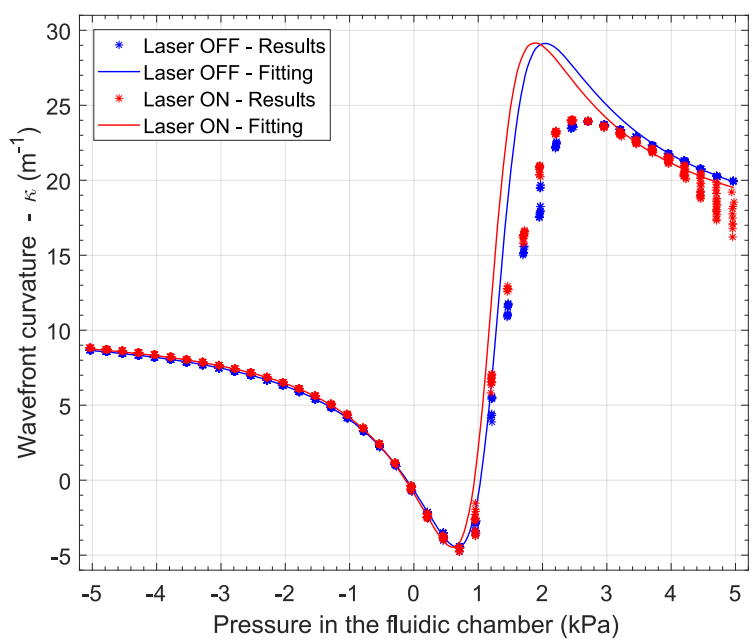

Figure 6-26: Characterization of the mirror deflection with and without CO_2 laser irradiation.

The results obtained with the laser off are similar to the results of the static characterization. As before, the measurements deviate from the parametric model for the pressure range which results in a laser spot diameter is lower than 1.2 mm. In this case, this pressure range corresponds to the interval from 0.951 to 2.718 kPa. The results do not show any hysteresis, which means that the behavior of the mirror was consistent during the entire experiment. This indicates that the high-power laser irradiation did not cause any permanent damage to the mirror properties.

The obtained coefficients for the parametric fitting of the measurements with the laser off are shown in Table 6.2. As it can be seen, the coefficients a, b and c of the mirror deflection curve are slightly different from the ones obtained for the static characterization, however it is worth noting that the precision of this fitting is lower due to the lower amount of data points. The RMSE obtained between the experimental results with the laser off and the corresponding parametric fitting is 2.737 m^{-1}.

Table 6.2: Parametric fitting of the experimental results of the thermal characterization with the laser off.

Parameter	Fitted value
a	-370.4
b	131.5
c	0.03949
L	20.45
d_W	0.08109

The measurements obtained with the laser on exhibit the same pattern as the ones with the laser off. With exception of the pressure range above 4 kPa, it is possible to see that the CO_2 laser irradiation did not increase the variance of the measurements per target pressure. This low variance of the measurements with the laser on suggests that the temperature of the mirror is constant during the acquisition. This means that the CO_2 laser increases the temperature of the mirror, but the temperature stabilizes quickly. For pressures over 4 kPa, the measurements presented large variance, indicating abnormal behavior of the mirror. One possible explanation to this behavior could be the presence of small defects on the coating of the mirror leading to increased absorption of the CO_2 laser for this specific shape of the deflected mirror. If this problem cannot be solved, the operating pressures of the mirror can be limited to the range from -5 to 4 kPa.

The parametric fitting of the measurements with the laser on was obtained by determining the value of the coefficient b that minimizes the RMSE of the fitting, while keeping the values of the other coefficients equal to the ones shown in Table 6.2. The obtained result for b was $b_{hot} = 122.5$. From this coefficient, the thermal

stress of the mirror induced by the laser irradiation can be obtained as:

$$\sigma_T = \sigma_0 - \frac{2\alpha b_{hot}}{h(1+\alpha^2)}. \tag{6.20}$$

Using the parameters of the mirror and the residual stress obtained in the static characterization, we obtain $\sigma_T = 30.01$ MPa. Using the 4.26, we can calculate the corresponding temperature variation of the mirror as $\Delta T = 22.57\,^{\circ}$C. This result is lower than the temperature increase obtained from the FEM thermal simulation of the mirror, presented in Section 4.1.4. This suggests that the hydraulic actuation system helps cooling the mirror.

Finally, the mirror deflection curves with and without laser irradiation can be partially reconstructed from the κ measurements as performed for the results of the static characterization. Fig. 6-27 shows both these curves. As it can be seen, the laser irradiation increases the magnitude of the mirror deflection, however the behavior of the mirror remains the same. The only exception for that are the pressure values above 4 kPa for which the mirror deflection becomes unstable.

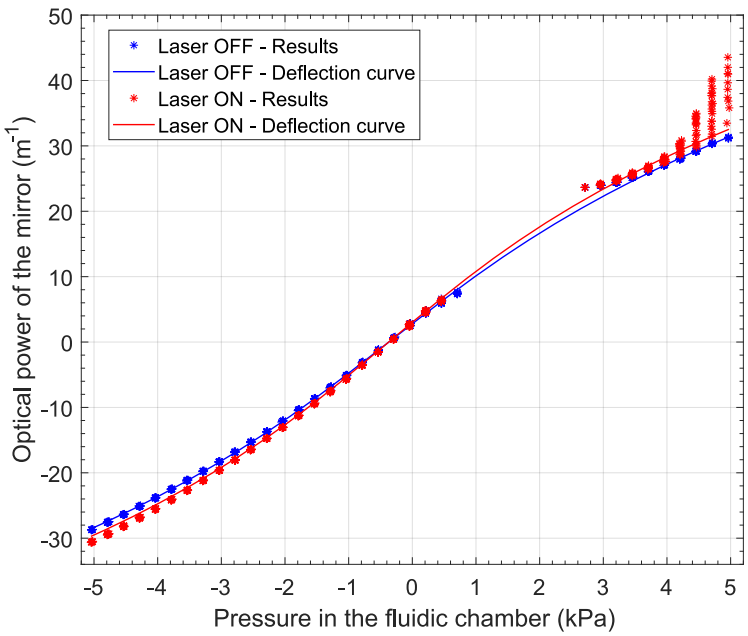

Figure 6-27: Deflection curve of the varifocal mirror with and without CO_2 laser irradiation, obtained from the results of the thermal characterization.

6.6 Step Response

To analyze the dynamic behavior of the fabricated varifocal mirror, we measured its step response.

6.6.1 Experimental Procedure

To measure the step response of the varifocal mirror with the hydraulic actuation system, we performed two sets of experiments. In the first experiment, the pressure of the fluidic chamber started at 0, which means the mirror was at its initial curvature. Then, the motor of the microinjection system was set to full speed for 50 ms, causing the mirror to bend in the convex direction. During this process, the optical power of the mirror was measured over time using the wavefront sensor.

In the second experiment, we made two modifications. The first one was the insertion of a microvalve between the microinjection system and the varifocal mirror. This allowed applying a larger pressure variation over a shorter time than in the previous experiment. The achieve that, the mirror started at its initial curvature as before. Then, the microvalve was closed and the microinjection system was actuated for 2s, increasing the pressure in the microfluidic channel before the microvalve. After that, the microvalve was opened changing the pressure of the fluidic chamber abruptly. The second modification was the replacement of the wavefront sensor by a high-speed camera. In this case, instead of measuring the optical power of the mirror, we measured only the diameter of the reflected beam at a fixed distance from the mirror.

6.6.2 Obtained Results

Fig. 6-28 shows the results obtained in both experiments. These experiments were performed with a circular mirror of 4 mm of diameter. In the first experiment (shown in Fig. 6-28a), the obtained settling time was 390 ms. The temporal resolution of this measurement was low, because the wavefront sensor takes 130 ms to reconstruct the wavefront of the beam. In the second experiment (shown in Fig. 6-28b), using the microvalve and the high-speed camera, the temporal resolution was higher and the obtained settling time was 180 ms. The response observed here was overdamped, which means this system could be modeled as a first-order system. This is probably a better representation of the dynamic behavior of the system, since the pressure variation was a better approximation of a step input.

It is also worth noting that the volume of oil in the hydraulic actuation circuit in the second experiment was lower than in the first one, since when we inserted the microvalve, we had to replace some of the tubes and ended up using shorter ones. This suggests that the settling time of the systems depends more on the hydraulic circuit than on the dynamics of the membrane. In fact, the volume of the hydraulic circuit in both experiments was in the order of 1 mL, while the volume of the fluidic chamber was only 6.6 µL. Based on that, we believe the settling time of the system can be greatly reduced by miniaturizing the hydraulic actuation system.

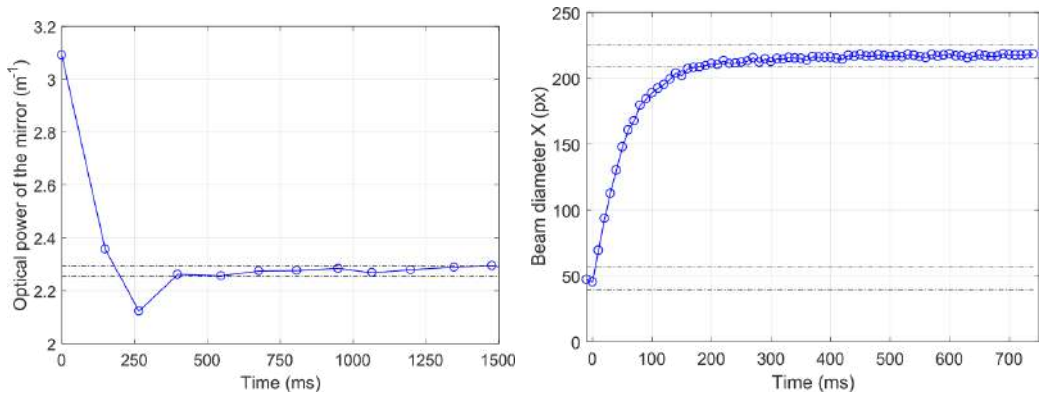

(a) (b)

Figure 6-28: Step response of the system obtained using (a) the microinjection system and (b) the microvalve.

6.7 Integration with Fiber Laser Tools

The results of the thermal characterization confirmed that the mirror deflection under CO_2 laser irradiation can be described by the thermal deflection model presented in Section 4.1.3. It also showed that the temperature variation induced by the CO_2 laser is constant for a constant laser power. Based on that, it is possible to control the focal length of the laser beam only based on the actuation pressure and the characterized thermal model. This allows us to control the focusing of the beam in open-loop by implementing the feed-forward controller presented in Section 4.4.1. Based on that, we could propose a fiber laser tool with a varifocal mirror-based focusing system, as illustrated in Fig. 6-29.

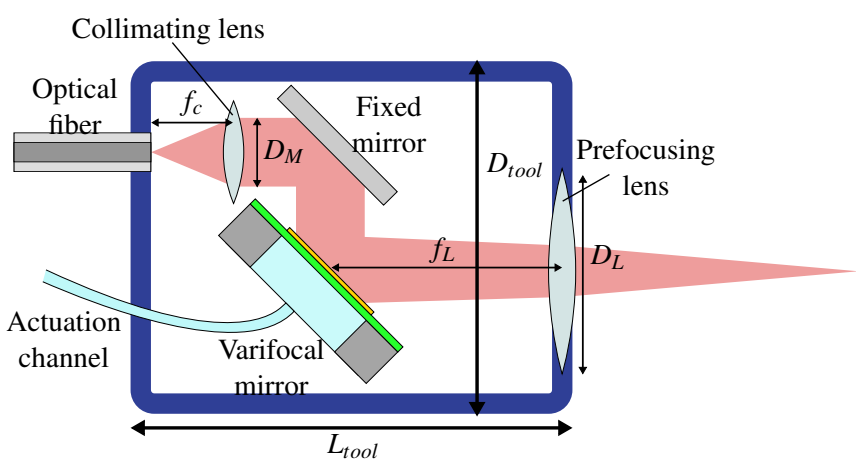

Figure 6-29: Schematic diagram of the proposed fiber laser tool with varifocal mirror-based focusing system.

The focusing system of such tool can be designed based on the application requirements and on the considerations made so far. The focal length of the collimating lens f_c must be selected to provide a collimated beam large enough to avoid thermal damage on the mirror. This depends on the power of the laser beam. For a laser of 3W, which is enough to ablate soft tissue in continuous-wave mode, we have seen that a collimated beam with diameter D_M of 3 mm is sufficient. To keep the direction of the output beam parallel to the optical fiber, the varifocal mirror can be used in combination with a fixed flat mirror, using an angle of incidence of 45°. The hydraulic actuator could be placed outside of the fiber tool and connected to the varifocal mirror using a microfluidic actuation channel, which can be placed next to the optical fiber. To simplify the focus controller, the distance between the mirror and the prefocusing lens should be equal to the focal length of the lens f_L, which must be selected based on the focal length range required by the clinical application. With this optical setup, the diameter of the tool D_{tool} would be approximately $3D_M$. For a collimated beam of 3 mm, this corresponds to 9 mm. The length of the tool depends mainly on the focal length of the prefocusing lens and could be approximately $L_{tool} = f_L + f_c + D_M$.

This focusing system could be integrated in the tip of a flexible endoscope, as long as the tip is rigid and is long enough to fit the entire optical system. This could be an issue if the focal length of the prefocusing lens f_L is large, which is why it is desirable to maximize the optical power range of the mirror. Another limitation of the proposed system is that its overall diameter D_{tool} is relatively large. Commercial flexible endoscopes can have an outer diameter of up to 14 mm, however their internal space may also contain optical fibers for illumination and for the cameras, cables for actuating the endoscope tip and an instrument channel. This means that the integration of the proposed focusing system in a flexible endoscope would be challenging, but we believe it could be possible depending on the endoscope design. Alternatively, this system could be integrated in a standalone fiber laser tool to be used in transoral procedures. In this case, the spatial limitation is less strict since the tool can be inserted through a laryngoscope, whose inner diameter can reach up to 19 mm.

One issue that has not been addressed yet is the measurement of the distance between the target and the tool. Since this information is needed to control the mirror deflection, the proposed fiber laser tool would need to have an integrated distance sensor. One possible solution would be to use a confocal distance sensor, such as proposed in [76], [77] or [78]. Another solution would be to estimate the distance to the target based on 3D reconstruction of the target tissue, as proposed in [79, 80]. In [79], the surface of the vocal cords are reconstructed in real-time and the reported precision of the distance estimation was 94 µm.

6.8 Conclusion

The experiments presented in this chapter allowed us to understand the thermal, static and dynamic behaviors of the fabricated varifocal mirrors and to evaluate their performance for focusing a laser beam. The main findings obtained were:

- The mirrors can achieve an optical power range of almost 60 m^{-1} for an actuation pressure of ± 5 kPa, being able to deflect both in concave and convex directions. When used with a prefocusing lens with focal length of 25 mm, this optical power range is able to shift the focal length of the laser beam from 5.32 to 41.88 mm, which is sufficient for many endoscopic surgical procedures.

- The optical aberrations observed were small, due to the parabolic deflection of the mirror, with exception of tip, tilt and vertical astigmatism. Tip and tilt are probably related to the connection between the varifocal mirror and the hydraulic actuation system and should be eliminated with a more stable design. Vertical astigmatism remains a problem but the overall optical quality of the mirror should be good enough to focus the laser beam without much distortion.

- The mirror is able to withstand a CO_2 laser beam of 3 W without suffering thermal damage. The temperature variation induced by the CO_2 irradiation was 22.57 °C. Since the temperature variation was constant, the mirror can still be controlled in open loop, which is important for miniaturizing the focusing system.

- The settling time of the mirror with the hydraulic actuation is 180 ms, which means the maximum operating frequency for the mirror is 5.56 Hz. However the settling time seems to depend on the volume of the actuation channel, which can be significantly miniaturized.

These results confirm the hypothesized advantages of hydraulic actuation over other actuation mechanisms. The obtained optical power range was higher than other varifocal mirrors, because the pressure we were able to apply was higher than the maximum pressure obtained with electrostatic or piezoelectric actuation. The mirror deflection presented negligible spherical aberration and overall good optical quality, since the hydraulic actuation generates uniform pressure over the membrane. And finally, the thermal effects of the CO_2 laser over the mirror were small since the hydraulic actuation increases the heat dissipation on the mirror.

The main drawback of the hydraulic actuation is the settling time of the system, which is much larger than the one obtained with other actuation mechanisms. However, we expect to be able to significantly reduce it by reducing the volume of the hydraulic circuit in at least one order of magnitude. In fact, the miniaturization of

the hydraulic actuation system is a critical step to allow integrating the developed varifocal mirror in an endoscopic tool, since the experimental setup used here was significantly large.

7
Conclusions and Future Works

This chapter presents the concluding remarks of this work, based on the obtained experimental results and the main scientific findings. It also presents some directions for future work, in order to integrate the proposed varifocal mirrors in endoscopic laser tools.

7.1 Concluding Remarks

Lasers were one of the greatest inventions of the 20th century. They have paved the way for breakthrough technology in fields such as microfabrication, imaging systems, sensors and medicine. In surgery, they have been used widely improving the performance of several surgical procedures and allowing new types of interventions such as retinal surgery.

With the development of minimally invasive and robot-assisted surgery, traditional surgical procedures are being redesigned to treat the patient with minimal trauma. This pushes the need for compact and smart surgical tools that are able to be operated inside the patient's body. In some cases, the development of these tools consists in miniaturizing traditional tools such as blades, scissors or grippers. In other cases, however, different approaches must be used. For these cases, recent technologies involving micro and nanosystems can have great impact.

This is the case of endoscopic laser surgery, which relies on flexible optical fibers to deliver the laser beam to the surgical site. Due to the lack of a compact optical system for precise focusing of the laser beam, fiber laser tools still perform significantly worse than traditional (free-beam) laser systems, often resulting in more tissue carbonization. In this thesis, we investigated how micro optical devices

such as MEMS varifocal mirrors can be used to improve the performance of fiber laser tools, by providing dynamic focusing of the surgical laser in a small form factor. We have addressed this problem by analyzing the requirements of the laser focusing task and by designing a new MEMS varifocal mirror based on hydraulic actuation.

The obtained results have demonstrated the feasibility of a MEMS varifocal mirror with hydraulic actuation for focusing high-power lasers. Using a microinjection system with $\pm$ 5 kPa of actuation, the mirror was able to provide an optical power range of 60 m^{-1}, which is three times higher than the optical power obtained by electrostatic mirrors of the same diameter. When used in combination with a prefocusing lens with focal length of 25 mm, this mirror allows controlling the focal length of the laser beam in the range from 5.32 to 41.88 mm. The mirror has showed low optical aberrations, except for some residual vertical astigmatism, and low thermal sensitivity. Under irradiation of a 3W CO_2 laser beam, the temperature variation of the mirror was 22.57 °C and the corresponding change in the mirror deflection due to the induced thermal stress has been well described by the proposed deflection model. This means the mirror can be controlled in open-loop, which allows designing a compact focusing system.

7.2 Future Work

The results obtained in this thesis have demonstrated the feasibility of focusing high-power lasers using a hydraulic MEMS varifocal mirror. However, extensive development is still required before the proposed varifocal mirrors are integrated in existing endoscopic laser systems. Some of the immediate improvements that could be made based on the developed prototypes are listed bellow.

7.2.1 Improvements to the MEMS Varifocal Mirror

Modeling of the Optical Quality

The proposed mirror deflection model allows determining the optical power of the mirror as a function of the applied pressure. However the focusing capability also depends on the optical quality of the mirror. In this work, we only evaluated the pressure range for which the aberrations are small, assuming them to be negligible within this interval. However a model of how the quality factor M^2 of the mirror changes with the applied pressure could improve the precision of the proposed focusing controller. This could be done using a beam profiler for actually measuring M^2 as a function of the applied pressure or by finding a method to accurately calculate M^2 from the measured zernike coefficients.

Mirror Fabrication and Assembly

The proposed mirror fabrication method contains some limitations that prevent us from fabricating an entire wafer of varifocal mirrors at once. These limitations are associated with the difficulty to release the membrane using wet etching. The process would be simplified and its consistency would probably increase if the wet etching step was eliminated. To achieve that, different fabrication processes can be used, allowing us to release the membrane with dry etching only or even using wafer bonding methods.

Experimental Characterization

The performed experiments allowed us to characterize the static, dynamic and thermal behavior of the fabricated mirrors. However other experiments would also be important to fully determine the performance and consistency of the proposed approach. Some relevant experiments include:

- Determine the Laser Induced Damage Threshold (LIDT) of the mirrors by measuring the maximum laser power that can be used with the mirror without resulting in thermal damage. This information is necessary to determine the clinical applications for which the mirror can be used.
- Determine the consistency of the microfabrication process by measuring the parameters and performance of different mirrors fabricated from the same wafer. This is important since the mirrors are controlled in open-loop, which requires accurate determination of its deflection parameters.
- Determine the lifetime of the mirror by performing fatigue tests, analyzing how many deflections the mirror can perform before it fails or its parameters deviate from the original values. This is important to determine how long the mirror can be operated before it needs to be replaced.

7.2.2 Design of a Compact Focusing System

Miniaturization of the Hydraulic Circuit

In order to integrate the proposed MEMS varifocal mirror in an endoscopic tool, the setup used to actuate the mirror must be miniaturized. This requires changing the mirror holder and the microfluidic tubes used in the hydraulic circuit. The design of the new mirror holder should include O-rings for improved sealing and stabilization of the mirror. This should eliminate the observed tip and tilt of the mirror under hydraulic actuation. The design of the new hydraulic circuit should reduce the volume of oil used in at least one order of magnitude in order to decrease the setting time of the system. One way to achieve this is by using an in-line pressure sensor, which allows eliminating the T-connection.

Integration with Distance Sensor

In order to develop a complete focusing system, the proposed varifocal mirror must be integrated with a sensor to measure the distance between the mirror and the tissue. This can be achieved using confocal sensors [76, 77, 78] or using distance measurement methods based on computer vision [79, 80].

A

Mathematical Derivations

This appendix contains mathematical derivations of some of the formulas presented in Chapters 4 and 6 of this thesis.

A.1 Solution to the Equation 4.36

The equation 4.36 relates the angle of the reflected beam 2θ by and off-axis parabolic mirror to the distance x_0 between the incident beam and the axis of the parabola. These values are indicated in Fig. A-1.

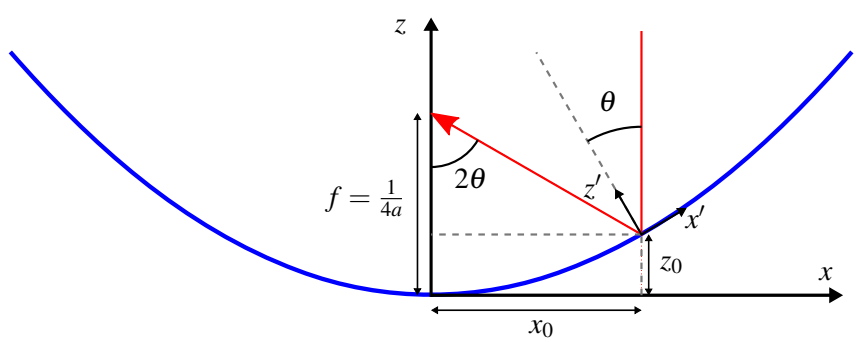

Figure A-1: Schematic diagram of a laser beam reflected by an off-axis parabolic mirror.

The equation we are interested in solving is:

$$tan(2\theta) = \frac{x_0}{\frac{1}{4a} - z_0}. \tag{A.1}$$

Replacing the term $z_0 = ax_0^2$ gives us:

$$tan(2\theta) = \frac{x_0}{\frac{1}{4a} - ax_0^2}, \tag{A.2}$$

which results in a second order equation on x_0:

$$4atan(2\theta)x_0^2 + 4ax_0 - tan(2\theta) = 0. \tag{A.3}$$

Solving this equation for x_0 gives us:

$$x_0 = \frac{-1 \pm \sqrt{tan(2\theta)^2 + 1}}{2atan(2\theta)}. \tag{A.4}$$

To simplify this expression, first we need to prove two trigonometric identities.

Proof 1: $1 + tan(\theta)tan(2\theta) = sec(2\theta)$

$$\begin{aligned}
1 + tan(\theta)tan(2\theta) &= 1 + \frac{sin(\theta)}{cos(\theta)}\frac{sin(2\theta)}{cos(2\theta)} \\
&= 1 + \frac{sin(\theta)2sin(\theta)cos(\theta)}{cos(\theta)cos(2\theta)} \\
&= 1 + \frac{2sin^2(\theta)}{cos(2\theta)} \\
&= \frac{cos(2\theta) + 2sin^2(\theta)}{cos(2\theta)} \\
&= \frac{cos^2(\theta) - sin^2(\theta) + 2sin^2(\theta)}{cos(2\theta)} \\
&= \frac{cos^2(\theta) + sin^2(\theta)}{cos(2\theta)} \\
&= \frac{1}{cos(2\theta)} \\
&= sec(2\theta)
\end{aligned} \tag{A.5}$$

Proof 2: $\frac{-1\pm\sqrt{tan^2(2\theta)+1}}{tan(2\theta)} = tan(\theta)$

$$\begin{aligned}
\frac{-1\pm\sqrt{tan^2(2\theta)+1}}{tan(2\theta)} &= tan(\theta) \\
-1\pm\sqrt{tan^2(2\theta)+1} &= tan(\theta)tan(2\theta) \\
\pm\sqrt{tan^2(2\theta)+1} &= 1+tan(\theta)tan(2\theta) \\
\pm\sqrt{tan^2(2\theta)+1} &= sec(2\theta) \\
tan^2(2\theta)+1 &= sec^2(2\theta) \\
\frac{sin^2(2\theta)}{cos^2(2\theta)}+1 &= \frac{1}{cos^2(2\theta)} \\
sin^2(2\theta)+cos^2(2\theta) &= 1
\end{aligned} \tag{A.6}$$

Replacing A.6 into A.4 gives us the solution to 4.36 as:

$$x_0 = \frac{tan(\theta)}{2a} \tag{A.7}$$

A.2 Taylor Series Expansion of the Function 4.43a

By isolating z' in the original expression 4.43a, we are able to write it as a function of x':

$$z' = g(x') = \frac{ac_\theta^3 x'^2}{2ac_\theta^2 s_\theta x' + 1}. \tag{A.8}$$

To simplify the next calculations, let us re-write A.8 as

$$g(x') = \frac{Ax'^2}{Bx'+1}, \tag{A.9}$$

with

$$A = ac_\theta^3 \tag{A.10}$$

and

$$B = 2ac_\theta^2 s_\theta. \tag{A.11}$$

Then the Taylor series expansion of 4.43a up to the fourth order is given by:

$$z' \cong g(0) + \frac{g'(0)}{1!}x' + \frac{g''(0)}{2!}x'^2 + \frac{g'''(0)}{3!}x'^3 + \frac{g''''(0)}{4!}x'^4 \tag{A.12}$$

The first four derivatives of the function $g(x')$ are given by:

$$\begin{aligned} g'(x') &= \frac{Ax'(Bx'+2)}{(Bx'+1)^2} \\ g''(x') &= \frac{2A}{(Bx'+1)^3} \\ g'''(x') &= \frac{-6AB}{(Bx'+1)^4} \\ g''''(x') &= \frac{24AB^2}{(Bx'+1)^5} \end{aligned} \tag{A.13}$$

Therefore the coefficients of the Taylor series expansion are given by:

$$\begin{aligned} g(0) &= 0 \\ g'(0) &= 0 \\ g''(0) &= 2A \\ g'''(0) &= -6AB \\ g''''(0) &= 24AB^2 \end{aligned} \tag{A.14}$$

Replacing A.10 and A.11 into A.14 gives us:

$$\begin{aligned} g(0) &= 0 \\ g'(0) &= 0 \\ g''(0) &= 2ac_\theta^3 \\ g'''(0) &= -12a^2c_\theta^5 s_\theta \\ g''''(0) &= 96a^3c_\theta^7 s_\theta^2 \end{aligned} \tag{A.15}$$

Finally, replacing A.15 into A.12 gives us:

$$z' \cong ac_\theta^3 x'^2 - 2a^2c_\theta^5 s_\theta x'^3 + 4a^3c_\theta^7 s_\theta^2 x'^4 \tag{A.16}$$

A.3 Conversion of the Measured Focal Length in the Fluorescent Medium

Fig. A-2 shows a schematic diagram of a laser beam being focused inside a fluorescent medium, such as a solution of fluorescein in water. As it can be seen, the light beam propagating in air enters the wall of the cuvette at an angle θ_a and is refracted at an angle θ_g. When exiting the cuvette, the beam is refracted again at an angle θ_w and starts propagating in water, until reaching its focal point. Due to these two refractions, the beam is focused in the water at a farther distance than it would, if it kept propagating only in air. Our goal here, is to calculate the relationship between

the obtained focal length in the water f_w and the corresponding focal length of the original beam f_a.

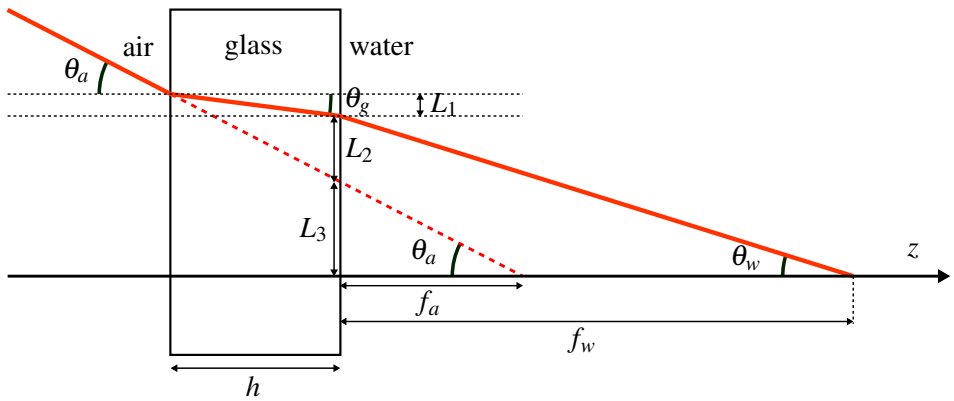

Figure A-2: Schematic diagram of a laser beam entering a glass cuvette and being focused inside water.

We begin by calculating the tangent of θ_w as:

$$tan\left(\theta_w\right) = \frac{L_2 + L_3}{f_w}. \tag{A.17}$$

Then, the lengths L_3 and L_2 can be obtained as

$$L_3 = f_a tan\left(\theta_a\right) \tag{A.18}$$

and

$$L_2 = htan\left(\theta_a\right) - L_1, \tag{A.19}$$

with L_1 being

$$L_1 = htan\left(\theta_g\right). \tag{A.20}$$

Replacing A.18, A.19 and A.20 in A.17, we obtain:

$$tan\left(\theta_w\right) = \frac{f_a tan\left(\theta_a\right) + h\left[tan\left(\theta_a\right) - tan\left(\theta_g\right)\right]}{f_w}, \tag{A.21}$$

which allows us to calculate f_a as:

$$f_a = \frac{f_w tan\left(\theta_w\right) - h\left[tan\left(\theta_a\right) - tan\left(\theta_g\right)\right]}{tan\left(\theta_a\right)}. \tag{A.22}$$

The angles θ_a, θ_g and θ_w are related by the Snell's law:

$$sin\left(\theta_a\right) n_a = sin\left(\theta_g\right) n_g = sin\left(\theta_w\right) n_w, \tag{A.23}$$

where n_a, n_g and n_w are the refractive indexes of air, the cuvette material and water respectively. If we consider all angles to be small ($\theta_g < \theta_w < \theta_a < 5°$), the paraxial approximation can be used, which yields $sin(\theta) \approx tan(\theta) \approx \theta$. With the paraxial approximation, A.22 becomes:

$$f_a = \frac{f_w \theta_w - h\left[\theta_a - \theta_g\right]}{\theta_a}. \tag{A.24}$$

and the Snell's law gives us:

$$\theta_g = \frac{\theta_a n_a}{n_g} \tag{A.25}$$

and

$$\theta_w = \frac{\theta_a n_a}{n_w}. \tag{A.26}$$

Replacing A.25 and A.26 in A.24 gives us:

$$f_a = f_w \frac{n_a}{n_w} - h\left(1 - \frac{n_a}{n_g}\right). \tag{A.27}$$

Knowing the distance d_c between the center of the varifocal mirror and the wall of the cuvette, the focal length of the mirror f_M can be calculated as a function of the measured focal length f_w by:

$$f_M = d_c + h + f_a, \tag{A.28}$$

which gives us

$$f_M = d_c + f_w \frac{n_a}{n_w} + h\frac{n_a}{n_g}. \tag{A.29}$$

Assuming the diameter of the collimated laser beam reflected by the mirror to be 2 mm, the condition used for the paraxial approximation ($\theta_a < 5°$) corresponds to $f_M > 11.43$ mm, which gives us $P_M < 87.5$ m^{-1}.

Bibliography

[1] Marc Rubinstein and William B Armstrong. Transoral laser microsurgery for laryngeal cancer: a primer and review of laser dosimetry. *Lasers in medical science*, 26(1):113–124, 2011.

[2] Michael L Hinni, Alfio Ferlito, Margaret S Brandwein-Gensler, Robert P Takes, Carl E Silver, William H Westra, Raja R Seethala, Juan P Rodrigo, June Corry, Carol R Bradford, et al. Surgical margins in head and neck cancer: a contemporary review. *Head & neck*, 35(9):1362–1370, 2013.

[3] Vasant Oswal, Marc Remacle, S Jovanvic, SM Zeitels, JP Krespi, and C Hopper. *Principles and practice of lasers in otorhinolaryngology and head and neck surgery*. Kugler Publications, 2014.

[4] Adam S Jacobson, Peak Woo, and Stanley M Shapshay. Emerging technology: flexible co2 laser waveguide. *Otolaryngology—Head and Neck Surgery*, 135(3):469–470, 2006.

[5] Z Wang and N Chocat. Fiber-optic technologies in laser-based therapeutics: threads for a cure. *Current pharmaceutical biotechnology*, 11(4):384–397, 2010.

[6] David L Dickensheets, Phillip A Himmer, Robert A Friholm, and B Jeffrey Lutzenberger. Miniature high-resolution imaging system with 3d moems beam scanning for mars exploration. In *MOEMS and Miniaturized Systems*, volume 4178, pages 90–98. International Society for Optics and Photonics, 2000.

[7] David L Dickensheets. Requirements of mems membrane mirrors for focus adjustment and aberration correction in endoscopic confocal and optical coherence tomography imaging instruments. *Journal of Micro/Nanolithography, MEMS, and MOEMS*, 7(2):021008, 2008.

[8] Alperen Acemoglu and S Leonardo Mattos. Non-contact tissue ablations with high-speed laser scanning in endoscopic laser microsurgery. In *2018 40th Annual International Conference of the IEEE Engineering in Medicine and Biology Society (EMBC)*, pages 3660–3663. IEEE, 2018.

[9] Philip Janda, Ronald Sroka, Boris Mundweil, Christian S Betz, Reinhold Baumgartner, and Andreas Leunig. Comparison of thermal tissue effects induced by contact application of fiber guided laser systems. *Lasers in Surgery and Medicine: The Official Journal of the American Society for Laser Medicine and Surgery*, 33(2):93–101, 2003.

[10] Grazyna T Rabczuk and M Sawczak. High-power cw co 2 laser beam properties in a system with a variable focal length mirror. In *Laser Optics 2003: Wavefront Transformation and Laser Beam Control*, volume 5481, pages 37–43. International Society for Optics and Photonics, 2004.

[11] Sarah J Lukes and David L Dickensheets. Agile scanning using a mems focus control mirror in a commercial confocal microscope. In *Three-Dimensional and Multidimensional Microscopy: Image Acquisition and Processing XXI*, volume 8949, page 89490W. International Society for Optics and Photonics, 2014.

[12] J Brunne, R Grunwald, and U Wallrabe. Adaptive piezoelectric axicon mirrors for high power femtosecond laser applications. In *Solid-State Sensors, Actuators and Microsystems Conference (TRANSDUCERS), 2011 16th International*, pages 1558–1561. IEEE, 2011.

[13] Vladimír Panc. *Theories of elastic plates*, volume 2. Springer Science & Business Media, 1975.

[14] Werner Karl Schomburg. Membranes. In *Introduction to Microsystem Design*, pages 29–52. Springer, 2011.

[15] Jeffrey Y Pan, Pinyen Lin, Fariborz Maseeh, and Stephen D Senturia. Verification of fem analysis of load-deflection methods for measuring mechanical properties of thin films. In *Solid-State Sensor and Actuator Workshop, 1990. 4th Technical Digest., IEEE*, pages 70–73. IEEE, 1990.

[16] Orazio Svelto, Stefano Longhi, Giuseppe Della Valle, Günter Huber, Stefan Kück, Markus Pollnau, Hartmut Hillmer, Thomas Kusserow, Rainer Engelbrecht, Frank Rohlfing (deceased), Jeffrey Kaiser, Ralf Malz, Gerd Marowsky, Klaus Mann, Peter Simon, Charles K. Rhodes, Frank J. Duarte, Annette Borsutzky, Johannes A. L'huillier, Markus W. Sigrist, Helen Wächter, Evgeny Saldin, Evgeny Schneidmiller, Mikhail Yurkov, Roland Sauerbrey, Joachim Hein, Michele Gianella, Jürgen Helmcke, Katsumi Midorikawa, Fritz Riehle, Steffen Steinberg, and Hans Brand. *Lasers and Coherent Light Sources*, pages 641–1046. Springer Berlin Heidelberg, Berlin, Heidelberg, 2012.

[17] Martí Duocastella. Lecture notes in laser-matter interactions, July 2017.

[18] Loris Fichera. *Cognitive Supervision for Robot-Assisted Minimally Invasive Laser Surgery*. Springer, 2016.

[19] Anthony E Siegman. Defining, measuring, and optimizing laser beam quality. In *Laser Resonators and Coherent Optics: Modeling, Technology, and Applications*, volume 1868, pages 2–13. International Society for Optics and Photonics, 1993.

[20] PA Bélanger. Beam propagation and the abcd ray matrices. *Optics letters*, 16(4):196–198, 1991.

[21] Herwig Kogelnik and Tingye Li. Laser beams and resonators. *Applied optics*, 5(10):1550–1567, 1966.

[22] James C Wyant and Katherine Creath. Basic wavefront aberration theory for optical metrology. *Applied optics and optical engineering*, 11(s 29):2, 1992.

[23] Lingqiang Meng, Zheqiang Huang, Zhigang Han, Hua Shen, and Rihong Zhu. Simulation and experiment studies of aberration effects on the measurement of laser beam quality factor (m 2). *Optics and Lasers in Engineering*, 100:226–233, 2018.

[24] Matthias Brinkmann, Joseph Hayden, Martin Letz, Steffen Reichel, Carol Click, Wolfgang Mannstadt, Bianca Schreder, Silke Wolff, Simone Ritter, Mark J. Davis, Thomas E. Bauer, Hongwen Ren, Yun-Hsing Fan, Yvonne Menke, Shin-Tson Wu, Klaus Bonrad, Eckhard Krätzig, Karsten Buse, and Roger A. Paquin. *Optical Materials and Their Properties*, pages 253–399. Springer Berlin Heidelberg, Berlin, Heidelberg, 2012.

[25] Markolf H Niemz. *Laser-tissue interactions: fundamentals and applications*. Springer Science & Business Media, 2013.

[26] Beina Azadgoli and Regina Y Baker. Laser applications in surgery. *Annals of translational medicine*, 4(23), 2016.

[27] Christopher L Hoy, Onur Ferhanoglu, Murat Yildirim, Ki Hyun Kim, Sandeep S Karajanagi, Ka Man Carmen Chan, James B Kobler, Steven M Zeitels, and Adela Ben-Yakar. Clinical ultrafast laser surgery: recent advances and future directions. *IEEE Journal of Selected Topics in Quantum Electronics*, 20(2):242–255, 2014.

[28] Jessica Burgner. *Robot assisted laser osteotomy*. KIT Scientific Publishing, 2010.

[29] Leon Goldman, Donald J Blaney, DJ Kindel, and Ernst K Franke. Effect of the laser beam on the skin. *J Invest Dermatol*, 40(121):2, 1963.

[30] Robert W Ryan, Tamir Wolf, Robert F Spetzler, Stephen W Coons, Yoel Fink, and Mark C Preul. Application of a flexible co2 laser fiber for neurosurgery: laser-tissue interactions. *Journal of neurosurgery*, 112(2):434–443, 2010.

[31] Nathaniel M Fried and Keith E Murray. High-power thulium fiber laser ablation of urinary tissues at 1.94 μm. *Journal of endourology*, 19(1):25–31, 2005.

[32] Ichiro Tateya, Akihiro Shiotani, Yasuo Satou, Masayuki Tomifuji, Shuko Morita, Manabu Muto, and Juichi Ito. Transoral surgery for laryngopharyngeal cancer–the paradigm shift of the head and cancer treatment. *Auris Nasus Larynx*, 43(1):21–32, 2016.

[33] Leonardo S Mattos, Giulio Dagnino, Gabriele Becattini, Massimo Dellepiane, and Darwin G Caldwell. A virtual scalpel system for computer-assisted laser microsurgery. In *Intelligent Robots and Systems (IROS), 2011 IEEE/RSJ International Conference on*, pages 1359–1365. IEEE, 2011.

[34] Uttam K Sinha and Laura A Gallagher. Effects of steel scalpel, ultrasonic scalpel, co2 laser, and monopolar and bipolar electrosurgery on wound healing in guinea pig oral mucosa. *The Laryngoscope*, 113(2):228–236, 2003.

[35] Nicolas Andreff and Brahim Tamadazte. Laser steering using virtual trifocal visual servoing. *The International Journal of Robotics Research*, 35(6):672–694, 2016.

[36] Gregory S Weinstein, Bert W O'Malley Jr, Shaun C Desai, and Harry Quon. Transoral robotic surgery: does the ends justify the means? *Current opinion in otolaryngology & head and neck surgery*, 17(2):126–131, 2009.

[37] Kanty Rabenorosoa, Bastien Tasca, Antonin Zerbib, Patrick Rougeot, Nicolas Andreff, and Ton Eakkachai Pengwang. Squipabot: A mesoscale parallel robot for a laser phonosurgery. *International Journal of Optomechatronics*, 9(4):310–324, 2015.

[38] Seyyed Mohammad Javad Moghimi. *Large-stroke deformable MEMS mirror for focus control*. Montana State University, 2013.

[39] Ryohei Hokari and Kazuhiro Hane. A varifocal convex micromirror driven by a bending moment. *IEEE Journal of Selected Topics in Quantum Electronics*, 15(5):1310–1316, 2009.

[40] Yuhe Shao, David L Dickensheets, and Phillip Himmer. 3-d moems mirror for laser beam pointing and focus control. *IEEE Journal of Selected Topics in Quantum Electronics*, 10(3):528–535, 2004.

[41] David L Dickensheets, Marshall Overcast, Phillip Himmer, Victor XD Yang, and I Alex Vitkin. Focus tracking in time domain optical coherence tomography using membrane mirrors operated near snap-down. In *Optical MEMS and Their Applications Conference, 2006. IEEE/LEOS International Conference on*, pages 170–171. IEEE, 2006.

[42] Phillip A Himmer, David L Dickensheets, and Robert A Friholm. Micromachined silicon nitride deformable mirrors for focus control. *Optics Letters*, 26(16):1280–1282, 2001.

[43] Phillip A Himmer and David L Dickensheets. Off-axis variable focus and aberration control mirrors. In *MOEMS Display and Imaging Systems*, volume 4985, pages 296–304. International Society for Optics and Photonics, 2003.

[44] Sarah Lukes, B Jeffrey Lutzenberger, Erwin Dunbar, Steven R Shaw, and David L Dickensheets. Variable-focus su-8 membrane mirror with enhanced stroke using feedback control. In *Optical MEMS and Nanophotonics, 2009 IEEE/LEOS International Conference on*, pages 141–142. IEEE, 2009.

[45] B Jeffrey Lutzenburger, Mohammad J Moghimi, Sarah J Lukes, Brant Kaylor, and David L Dickensheets. Mems deformable mirrors for focus control in vital microscopy. In *MOEMS and Miniaturized Systems IX*, volume 7594, page 759406. International Society for Optics and Photonics, 2010.

[46] Sarah J Lukes and David L Dickensheets. Su-8 focus control mirrors released by xef 2 dry etch. In *MOEMS and Miniaturized Systems X*, volume 7930, page 793006. International Society for Optics and Photonics, 2011.

[47] Sarah J Lukes and David L Dickensheets. Su-8 2002 surface micromachined deformable membrane mirrors. *Journal of Microelectromechanical Systems*, 22(1):94–106, 2013.

[48] David L Dickensheets, Paul V Ashcraft, and Phillip A Himmer. Pixel-by-pixel aberration correction for scanned-beam micro-optical instruments. In *Miniaturized Systems with Micro-Optics and MEMS*, volume 3878, pages 48–58. International Society for Optics and Photonics, 1999.

[49] Mohammad J Moghimi, Krishna Chattergoon, Chris Wilson, and David L Dickensheets. Deformable mirror with controlled air damping for fast focus tracking and scanning. In *MOEMS and Miniaturized Systems XI*, volume 8252, page 82520M. International Society for Optics and Photonics, 2012.

[50] Mohammad J Moghimi, Krishna N Chattergoon, Chris R Wilson, and David L Dickensheets. High speed focus control mems mirror with controlled air damping for vital microscopy. *Journal of Microelectromechanical Systems*, 22(4):938–948, 2013.

[51] Jen-Liang Wang, Tyng-Yow Chen, ChingWei Liu, Chen-Wei Edward Chiu, and Guo-Dung John Su. Polymer deformable mirror for optical auto focusing. *ETRI journal*, 29(6):817–819, 2007.

[52] Md Mahabub Hossain, Wu Bin, and Seong Ho Kong. Large-stroke convex micromirror actuated by electromagnetic force for optical power control. *Optics express*, 23(22):28358–28368, 2015.

[53] Mohammad J Moghimi and David L Dickensheets. Electrostatic-pneumatic membrane mirror with positive or negative variable optical power. *Journal of Microelectromechanical Systems*, 24(3):716–729, 2015.

[54] Ammar A Alzaydi, John TW Yeow, and Sangjune L Lee. Hydraulic controlled polyester-based micro adaptive mirror with adjustable focal length. *Mechatronics*, 18(2):61–70, 2008.

[55] Jessica Morrison, Matthias Imboden, Thomas DC Little, and DJ Bishop. Electrothermally actuated tip-tilt-piston micromirror with integrated varifocal capability. *Optics express*, 23(7):9555–9566, 2015.

[56] DM Burns and VM Bright. Micro-electro-mechanical focusing mirrors. In *Micro Electro Mechanical Systems, 1998. MEMS 98. Proceedings., The Eleventh Annual International Workshop on*, pages 460–465. IEEE, 1998.

[57] Wei Liu and Joseph J Talghader. Current-controlled curvature of coated micromirrors. *Optics letters*, 28(11):932–934, 2003.

[58] Max Ti-Kuang Hou, Ke-Min Liao, Hong-Zhen Yeh, Bo-Wen Cheng, Pei-Yuan Hong, and Rongshun Chen. Fabrication of micromachined focusing mirrors with seamless reflective surface. In *MOEMS and Miniaturized Systems III*, volume 4983, pages 359–367. International Society for Optics and Photonics, 2003.

[59] Li Li, Ran Li, Walter Lubeigt, and Deepak Uttamchandani. Design, simulation, and characterization of a bimorph varifocal micromirror and its application in an optical imaging system. *Journal of Microelectromechanical Systems*, 22(2):285–294, 2013.

[60] Alan Paterson, Ralf Bauer, Li Li, Walter Lubeigt, and Deepak Uttamchandani. Range extension of a bimorph varifocal micromirror through actuation by a peltier element. *IEEE Journal of Selected Topics in Quantum Electronics*, 21(4):72–78, 2015.

[61] Moritz Sturmer, Matthias C Wapler, Jens Brunne, and Ulrike Wallrabe. Focusing mirror with tunable eccentricity. In *Optical MEMS and Nanophotonics (OMN), 2013 International Conference on*, pages 159–160. IEEE, 2013.

[62] Mark J Mescher, Michael L Vladimer, and Jonathan J Bernstein. A novel high-speed piezoelectric deformable varifocal mirror for optical applications. In *Micro Electro Mechanical Systems, 2002. The Fifteenth IEEE International Conference on*, pages 511–515. IEEE, 2002.

[63] Paul Janin, Ralf Bauer, Paul Griffin, Erling Riis, and Deepak Uttamchandani. Characterization of a fast piezoelectric varifocal mems mirror. In *2018 International Conference on Optical MEMS and Nanophotonics (OMN)*, pages 1–5. IEEE, 2018.

[64] Augustus Edward Hough Love. Xvi. the small free vibrations and deformation of a thin elastic shell. *Philosophical Transactions of the Royal Society of London.(A.)*, (179):491–546, 1888.

[65] Stephen P Timoshenko and Sergius Woinowsky-Krieger. *Theory of plates and shells*. McGraw-hill, 1959.

[66] Fuzhang Zhao. Nonlinear solutions for circular membranes and thin plates. In *Modeling, Signal Processing, and Control for Smart Structures 2008*, volume 6926, page 69260W. International Society for Optics and Photonics, 2008.

[67] JW Beams. Mechanical properties of thin films of gold and silver. structure and properties of thin film, ca neugebauer, jd newkirk, and da vermilyea, eds, 1959.

[68] Sarah J Lukes, David Lämmle, and David L Dickensheets. Surface micromachined su-8 2002 membrane mirrors for focus control. In *MOEMS and Miniaturized Systems IX*, volume 7594, page 75940E. International Society for Optics and Photonics, 2010.

[69] B Schwartz and H Robbins. Chemical etching of silicon iv. etching technology. *Journal of the electrochemical society*, 123(12):1903–1909, 1976.

[70] Kalpathy B. Sundaram, Arun Vijayakumar, and Ganesh Subramanian. Smooth etching of silicon using tmah and isopropyl alcohol for mems applications. *Microelectronic Engineering*, 77(3):230 – 241, 2005.

[71] Thilo Sandner, Simon Kimme, Thomas Grasshoff, Ulrich Todt, Alexander Graf, Christian Tulea, Achim Lenenbach, and Harald Schenk. Micro-scanning mirrors for high-power laser applications in laser surgery. In *Optical MEMS and Nanophotonics (OMN), 2013 International Conference on*, pages 83–84. IEEE, 2013.

[72] Daniel R Neal, William J Alford, James K Gruetzner, and Mial E Warren. Amplitude and phase beam characterization using a two-dimensional wavefront

sensor. In *Third International Workshop on Laser Beam and Optics Characterization*, volume 2870, pages 72–83. International Society for Optics and Photonics, 1996.

[73] Jianghua Xu and Songlin Zhuang. Measurement of lens focal length with hartmann–shack wavefront sensor based on 4f system. *Optik-International Journal for Light and Electron Optics*, 126(13):1303–1306, 2015.

[74] P Temple-Boyer, C Rossi, E Saint-Etienne, and E Scheid. Residual stress in low pressure chemical vapor deposition sin x films deposited from silane and ammonia. *Journal of Vacuum Science & Technology A: Vacuum, Surfaces, and Films*, 16(4):2003–2007, 1998.

[75] Armando Gomez-Vieyra and Daniel Malacara-Hernández. Geometric theory of wavefront aberrations in an off-axis spherical mirror. *Applied optics*, 50(1):66–73, 2011.

[76] Pete Rizun and Garnette Sutherland. Tactile feedback laser system with applications to robotic surgery. In *Eurohaptics Conference, 2005 and Symposium on Haptic Interfaces for Virtual Environment and Teleoperator Systems, 2005. World Haptics 2005. First Joint*, pages 426–431. IEEE, 2005.

[77] Takeshi Seki, Kiyoshi Oka, Akihiro Naganawa, Hiromasa Yamashita, Keri Kim, and Toshio Chiba. Laser distance measurement using a newly developed composite-type optical fiberscope for fetoscopic laser surgery. *Optics and Lasers in Engineering*, 48(10):974–977, 2010.

[78] Hongen Liao, Masafumi Noguchi, Takashi Maruyama, Yoshihiro Muragaki, Etsuko Kobayashi, Hiroshi Iseki, and Ichiro Sakuma. An integrated diagnosis and therapeutic system using intra-operative 5-aminolevulinic-acid-induced fluorescence guided robotic laser ablation for precision neurosurgery. *Medical image analysis*, 16(3):754–766, 2012.

[79] Andreas Schoob, Dennis Kundrat, Lukas Kleingrothe, Lüder A Kahrs, Nicolas Andreff, and Tobias Ortmaier. Tissue surface information for intraoperative incision planning and focus adjustment in laser surgery. *International journal of computer assisted radiology and surgery*, 10(2):171–181, 2015.

[80] Brahim Tamadazte and Nicolas Andreff. Weakly calibrated stereoscopic visual servoing for laser steering: Application to phonomicrosurgery. In *Intelligent Robots and Systems (IROS 2014), 2014 IEEE/RSJ International Conference on*, pages 743–748. IEEE, 2014.